A study of the physicochemical pathways in an atmospheric surface barrier discharge for microbial inactivation

Thesis submitted in accordance with the requirements of the University of Liverpool for the degree of Doctoral in Philosophy by

Aaron P. Dickenson, M.Eng

Centre for Plasma Microbiology

University of Liverpool

July 2019

Contents

Abstract

A major cause for concern in the healthcare sector is the treatment of chronic infections caused by pathogenic microorganisms, particularly those in the form of a biofilm. Conventional biofilm decontamination techniques such as antibiotic treatment rapidly become ineffective due to the emergence of resistant organisms. It is estimated that up to 80% of human bacterial infections are caused by biofilms, therefore there is an urgent global need to develop an effective method for biofilm decontamination. [1]

Atmospheric pressure non-thermal plasma generated in ambient air have proven to be a highly effective biocide, their low temperature nature presents a number of opportunities for the healthcare sector. Within such plasmas a plethora of charged and neutral reactive nitrogen and oxygen species (RONS) are created, such as O, OH, O_3, H_2O_2, NO etc… It is the nature of these RONS that drive applications within the healthcare sector, as the presence of certain species can cause microbial death. Given that these types of plasmas are generated at near room temperature they provide a means to treat materials that are thermosensitive, which is particularly important when it comes to the decontamination of invasive medical equipment that can be damaged through current sterilisation techniques that employ high temperatures (i.e. autoclaving).

This thesis focuses on the surface barrier discharge (SBD), a class of device based on the widely used dielectric barrier discharge configuration. SBD's are known to be extremely stable whilst operating in ambient air and can be generated over large areas. A key disadvantage of the SBD system is the spatial separation between the plasma generation region and the target sample, which limits the transport of highly reactive and highly antimicrobial RONS such as O, N and OH to the target. In this work the underpinning discharge mechanisms involved in the generation and transportation of reactive chemistries from a surface barrier discharge are explored.

Efforts focus on the interplay between electrode geometry and the breakdown characteristics of the discharge, as decreasing the area of a circular discharge gap below a certain threshold is shown to cause an exponential increase to the breakdown voltage, while also impacting several other discharge characteristics including deposited power and the EHD induced flow. The dielectric temperature effects on species generation is shown, as the rate at which the transition into ozone poisoning mode occurs can be altered and essentially negated entirely through dielectric temperature manipulation, while the influence of air feed rate into the discharge chamber is also presented alongside as a viable means of transition control. Thus, enabling the density of specific RONS to be tailored for the needs of an application.

Through both experimental investigations and simulations, the transport dynamics of key reactive nitrogen species (RNS) that are relevant in biofilm decontamination are found to be carried several cm from the active discharge domain, closely following the plasma induced flow. While a method to exert a degree of control over the induced flow is also established, through the introduction of a phase shift between the high voltage signals applied to a linear electrode configuration, without compromising the chemistry of the downstream reactive species.

Finally, the impact of plasma-liquid interactions on biofilm decontamination efficacy is assessed, as the composition of the liquid phase species is demonstrated to have significant influence over the bactericidal efficacy of plasma activated water (PAW). Several possible underpinning mechanisms responsible for microbial inactivation are identified, that include the production of reactive nitrogen species under acidic conditions. The work presented in this thesis adds to the field by giving an insight into the reactive chemistries and dynamics of species generated by non-thermal discharges. Several techniques are demonstrated to essentially tailor the physical and chemical nature of SBDs to the needs of future applications.

Acknowledgements

First and foremost, I would like to express my gratitude to my supervisor Dr James Walsh who not only provided me with the opportunity to carry out this PhD but also presented me with a number of opportunities along the way to broaden my knowledge and experiences in the academic world. I also appreciate his continuous guidance and support received throughout the duration of my study at the University of Liverpool.

Thank you to the funding body EPSRC for enabling this PhD to take place. A Special thanks goes to my collaborators Mohammad Hasan, Youssef Morabit, Martina Modic Nikolay Britun, Anton Nikiforov, Neil McCloude and Mark Sutton, with whom I had the pleasure of meeting and enjoyed working with on a number of different projects. My thanks go to my academic advisors Prof James Bradley and Dr Kirsty McKay for their guidance and feedback from annual reviews. I would also like to express my appreciation for all the valuable help I received from Gareth Blacoe, Jill Anson and Phil Hilton along the way. Many thanks to my fellow researchers Mike Barnes, Paddy McCarthy, Stephane Florent Joel, Andreas Katsigiannis, Stefania Fabbri, Peter Ryan, Matt Smith, Felix Walk, Brandon Harris, who have all made my experience over the course of my studies an enjoyable one.

To my friends Peter Edmondson, Elly Stevens, Sebastian Karam, Nuzli Karam, Chinmay Mishra and Gary Stanton I would like to express my sincere appreciation for all their kindness, the good times shared and for being supportive whenever things got tough. I would like to end with a huge thank you to my parents, my sister and to the rest of my family for their constant encouragement throughout my studies and for the love and support they provide me with throughout life.

Sources

Laser induced fluorescence experimentation was conducted at the Chimie des Interactions Plasma-Surface, University of Mons under the supervision of Nikolay Britun, and with Anton Nikiforov from the Department of Applied Physics, Ghent University. While data gathered through Fourier transform infra-red spectroscopy seen in chapter 5, was collated with past data collected by Dr Y Ni, University of Liverpool PhD graduate. All other experimental data was collected through investigations independently carried out in the center of plasma microbiology, at the University of Liverpool. All computational modeling seen within investigations throughout this contribution, were conducted by Dr Mohammad Hasan at the Department of Electrical Engineering & Electronics, University of Liverpool.

List of figures

List of abbreviations

DC – Direct current

AC – Alternating current

HV – High voltage

DBD – Dielectric barrier discharge

SBD – Surface barrier discharge

EHD - Electrohydrodynamic

PIV – Particle imaging velocimetry

LIF – Laser induced fluorescence

SHG – Second harmonic generator

FTIR – Fourier transform infrared

OES – Optical emission spectroscopy

RONS – Reactive oxygen and nitrogen species

ROS – Reactive oxygen species

RNS – Reactive nitrogen species

PAW – Plasma activated water

PAL/PAF – Plasma activated liquid/fluid

CFU – Colony forming units

TSA/TSB – Tryptic soy agar/broth

HPLC – High performance liquid chromatography

Publications

The generation and transport of reactive nitrogen species from a low temperature atmospheric pressure air plasma source

2018, Physical Chemistry Chemical Physics, 20(45)

A. Dickenson, N. Britun, A. Nikiforov, C. Leys, M. I. Hasan & J. L. Walsh

Directional mass transport in an atmospheric pressure surface barrier discharge

2017, Scientific Reports, 7, Article number: 14003

A. Dickenson, Y. Morabit, M. I. Hasan & J. L. Walsh

Impact of electrode geometry on an atmospheric pressure surface barrier discharge

2017, Applied Physics Letters, 110, 264101

M. I. Hasan, Y. Morabit, **A. Dickenson** & J. L. Walsh

Antimicrobial efficacy of cold atmospheric plasma for different intrinsic and extrinsic parameters

2017, Plasma Processes and Polymers, 15(2)

C. Smet, M. Baka, **A. Dickenson**, J. L. Walsh, V. P. Valdramidis & J. F. Van Impe

Chapter 1: Introduction

1.1 Challenge

Over the past decade, plasmas generated at atmospheric pressure with highly non-equilibrium thermal properties have been the subject of intense research due to their unique ability to create a plethora of charged and neutral reactive oxygen and nitrogen species (RONS) under ambient conditions. Of all the promising areas of application for such plasmas, which range from environmental remediation to nanomaterials synthesis, it is the hope that they offer within the healthcare sector for the decontamination of pathogenic microorganisms in particular, that has spurred a global research effort.

Despite the enormous potential societal and economic benefits of plasma technology within the healthcare sector, many plasma-based technologies remain at the proof of concept stage due to the difficulties in understanding and controlling the physicochemical properties of the discharge. Under the highly collisional conditions experienced at atmospheric pressure and the complex chemical environment arising as a consequence of operating beyond the controlled environment of a vacuum chamber, the challenge of generating controlled doses of specific RONS to elicit a specific biological response remains unaddressed.

This work aims to contribute towards addressing this challenge by exploring the link between the plasma power source, species generation, species transport and ultimately the impact they have upon biological substrates.

1.2 Objectives

The aim of this work was to take a holistic view of a promising plasma-medicine related application, that of microbial decontamination, and apply advanced experimental techniques in order to understand the mechanisms governing the generation of RONS and identify opportunities where the composition and density of RONS arriving at a downstream sample surface could be manipulated. Throughout the work an SBD operating in ambient air was the focus of the research, such efforts were motivated by the widespread use of the SBD, a consequence of their ease of use, simple construction and scalability.

To addresses this aim three interlinked objectives were identified:

(1) Identify the link between the electrical excitation and electrode geometry on the processes governing the generation of RONS within the plasma.
(2) Examine the mass-transport of reactive species from the plasma region to a downstream sample and identify opportunities to manipulate transport processes.
(3) Explore the impact of plasma generated RONS on biological samples, including those within a liquid volume which is often unavoidable in a healthcare scenario.

1.3 Novelty

The simple surface barrier discharge (SBD) is a subset of the Dielectric Barrier Discharge (DBD) family; as such, it has been under active investigation for well over 100 years [2], [3]. While much of this effort has focused on the use of DBD’s, including SBD’s, for the purpose of Ozone generation, there remains a comprehensive body of literature focused on the physics and chemistry of the SBD. Critically, much of this previous work has focused on maximising ozone generation efficiency, with little attention being paid to the other RONS created within the discharge or how RONS are transported from the plasma region to a sample placed downstream. As a result, the SBD offers considerable scope for novel research and this thesis has made several notable contributions to the area, including:

(1) Demonstration of a link between electrode geometry and breakdown voltage – Despite the complexities associated with gas breakdown, it is a well understood process in the field of plasma science. In this work, a deviation from the conventional Paschen Law was characterised in a SBD for the first time, reported in *Applied Physics Letters*.

(2) Identification of a technique to manipulate the transport of reactive neutral species from the plasma region – it is often assumed that diffusion is the primary mode of mass transport from a SBD. In this work, it was demonstrated that Electrohydrodynamic (EHD) forces give rise to convection which dominates the process. Using a novel plasma power source developed specifically for the purpose, a technique to electrically control the direction of mass transport was established; reported in *Nature Scientific Reports*. Using Planar Laser Induced Fluorescence the transport of RNS, specifically Nitric Oxide, from an SBD was examined for the first time and shown to closely follow the EHD driven flow; reported in *Physical Chemistry Chemical Physics*.

(3) Identification of a technique to manipulate the composition of RONS generated within the discharge – a link between discharge power and RONS generation in an SBD has been widely reported. Using a novel plasma power source, a means to manipulate the generation of RONS was established, giving the ability to electrically switch between ROS and RNS generation regime without having to vary the dissipated power within the discharge.

1.4 Thesis outline

This thesis contains 8 chapters, chapter two contains a brief overview of atmospheric pressure plasma science followed by a concise review of the recent literature on SBD’s, their applications and a summary of the use of plasma within the healthcare sector. Chapter three details the advanced measurement techniques adopted throughout this work. Chapter four explores the impact of electrode geometry on breakdown voltage and species transport. Chapter five explores a technique to electronically vary the composition of RONS generated within the plasma region. Chapter six focuses on the use of PLIF to quantify Nitric Oxide transport from the discharge region. Chapter seven highlights a methodology in which the EHD forces generated by the discharge can be manipulated electronically, facilitating the directional control of species transport. Chapter eight highlights the microbial decontamination impact of plasma RONS exposure on liquid samples. Finally, Chapter nine presents the major conclusions from the study and suggests avenues for future investigation.

Chapter 2: Literature review

2.1 Basic principles

Plasma, known as the fourth state of matter, occurs when a gas becomes “ionised” *i.e.* atoms or molecules become positively (or negatively) charged due to electron(s) loss (or gain), this state of matter is termed a Plasma.

This ionisation can occur through application of a sufficiently high electric field to cause free electrons to accelerate and collide with heavier molecules/atoms, resulting in the liberation of bound electrons from their orbitals; or through substantial heating providing atoms/molecules with enough energy for ion creation. Given this it is considered the fourth state of matter as it is transformed by breaking bonds, from solid, to liquid, to gas and then finally to plasma.

2.2 Plasma classification

A term often used in plasma physics is the “ionisation degree” this refers to the proportion of ions present in the plasma. Weakly ionised plasmas are defined by having a low ionization degree (e.g. 10^{-6}) whereas with a completely ionised gas, the ionization degree is close to unity. [4]

Plasma can also be classified as thermal & non-thermal. Thermal plasmas are characterised by the temperature of electrons and the temperature of the heavy neutral particles being close to thermal equilibrium. Whereas electron temperature, which is usually ~1eV in many non-thermal plasmas, substantially exceed that of the heavier particles which can be close to room temperature (e.g. 0.025 eV). [4] For this reason and the fact that highly reactive species can be readily generated from the chemical pathways initiated by creation of radicals, a plethora of applications utilising non-thermal plasmas have emerged over the past decades.

In a plasma the concentration of positive and negative charges are approximately equal and are therefore considered quasi-neutral. [5] The electron temperature T_e and electron number density, n_e, in plasmas are usually used in their classification, as seen in figure 1.

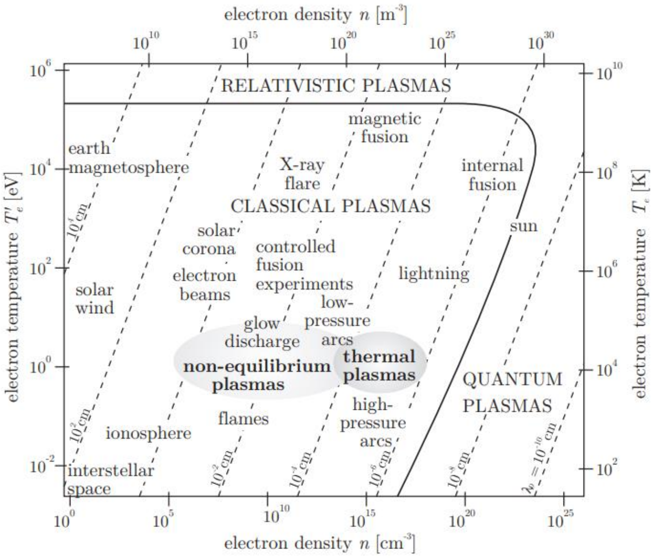

Figure 1: Classification of plasmas with respect to electron density & temperature. [6]

2.3 Discharge regimes

Plasma discharges can be divided into different regimes depending on their non-linear voltage and current characteristics, as seen in figure 2. This relationship was demonstrated by Roth [7] for DC low pressure electrical discharge tubes but is equally applicable in the analysis of IV characteristics of a DBD driven by AC at atmospheric pressure.

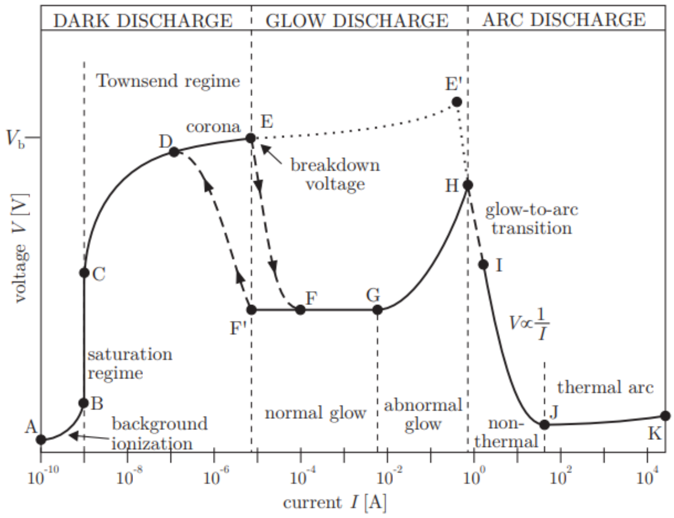

Figure 2: Discharge classification based on V-I characteristics of a low pressure DC discharge tube. [7]

2.3.1 Dark discharge:

In this regime, only ionised gas atoms/molecules from background radiation contributes charges to the current flow when the applied voltage is low (A-B). As the voltage is increased in this background ionization regime the charges available are accelerated towards the electrode until all charges produced by background ionization reach the electrodes (B). At this point a saturation regime is reached due to the lack of ionised gas, this is characterised by current stagnation with increasing voltage (B-C). Further increase in the applied voltage past this regime generates a sufficiently strong electric field to partially ionise the background gas, leading to discharge avalanches and an exponential increase in the current occurs (C-E), known as the Townsend regime. If the electrodes contain sharp tips/edges then visible corona discharges may occur in the later part of the Townsend regime (D-E).

2.3.2 Glow discharge:

At the end of the Townsend regime, a point known as the breakdown voltage (E) is reached where electrical breakdown occurs followed by transition to a visible glow discharge (E-F). The characteristic voltage drop of this transition takes place due to the significantly increased current flow. An increase in current is seen after this transition which is relatively independent of the applied voltage as the plasma begins to cover the whole cathode (F-G). Once the entire cathode is covered with plasma (G), the discharge enters an abnormal glow regime that requires a considerable increase in voltage to increase current (G-H). The electrodes start to heat in the abnormal glow regime.

2.3.3 Arc discharge:

Past the abnormal glow regime, a glow to arc transition occurs (H-I) that leads into a non-thermal arc (I-J) as thermionic emission of electrons from the cathode takes place. The voltage in this transition decreases rapidly due to the additional charges from this emission. Beyond the minimum voltage of the arc discharge regime (J), thermal arcs occur characterised by rapid increase of current with a slight increase in voltage.

2.4 Paschen’s law & curve

Plasma discharges can be generated across an electrode gap on application of a sufficiently large enough potential difference (i.e strong electric field). This is usually referred to as the breakdown voltage, V_B. An investigation by Paschen in 1889 [8] revealed that the breakdown voltage between two planar electrodes in air is dependent on pressure and gap distance between electrodes. This is usually represented as an equation known as Paschen’s law.

$$V = f(pd) \tag{2.3}$$

The relationship between V and pd is not linear, and in fact has a minimum value. This is displayed as Paschen's curve, seen in figure 3. Additional investigations found that different gas molecules have their own curve. From Paschens curve, it can be easily seen that breakdown voltage V_B varies proportionally with pd at atmospheric pressure conditions and above, for discharge gap distances on a mm scale. However, for low pressure conditions the relationship reverses as there are less molecules to for the ionisation mechanisms to take place.

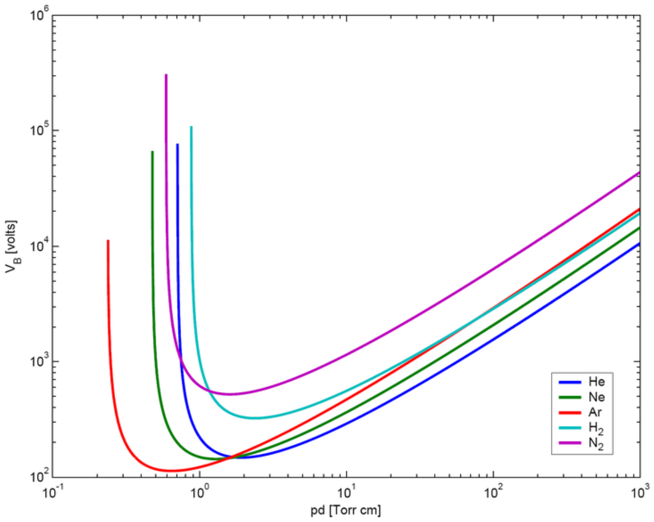

Figure 3: Paschen curves for a parallel plate discharge in different gases. [9]

Even though this is representative of discharges between parallel plates in open space, it also widely used to explain the breakdown characteristics of other discharge configurations, in different environmental conditions.

2.5 Dielectric barrier discharges

2.5.1 Historical summary

Experimental investigations using barrier discharges were first introduced by Siemens in 1857 for ozone generation. [2] Siemens used the dielectric barrier discharge (DBD) configuration seen in figure 4 to form a plasma discharge in a narrow annular gap between two coaxial glass tubes, cylindrical electrodes inside the inner tube and wrapped around the outer tube were powered with an alternating voltage high enough to achieve breakdown. Ozone was generated at the exit of the tube by feeding oxygen/air through the annular discharge gap from the opposing end.

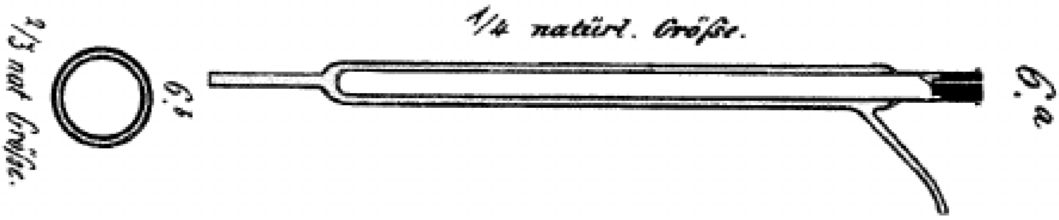

Figure 4: Illustration from the original 1857 patent application from Siemans, showing the DBD discharge tube used for ozone generation. [2]

The discharge observed by Siemens is often referred to as a “silent discharge”, a term that was first proposed by Andrews and Tait in 1860. [10] Many important investigations were carried out on silent discharges at the beginning of the 20th century. The design of industrial ozone generators using DBD configurations was the focus of Becker and Otto In the 1920’s [11], [12] while investigations into the nature of such discharges were carried out by Warburg. [13], [14] Langmuir first introduced the term “plasma” in 1928, as a means of describing region of electrically neutral discharge. [15]

An important characteristic of barrier discharges was uncovered by Buss In 1932. [16] He showed that breakdown in an atmospheric pressure air dielectric barrier discharges occurs as many short-lived current filaments, the formation of which is discussed in section 2.5.5. Buss obtained the first 'Lichtenberg figures' showing the footprints of the individual filaments along with oscilloscope recordings of current and voltage. From these measurements Buss was able to deduce information about the number of filaments per unit area, the typical duration of a filaments which were found to last few nanoseconds (e.g. 1-20 ns) and transport charge in a filament to a fairly high degree. Throughout the 20th and 21st century our understanding of the nature of these filaments became the focus of a number of investigations. [17]–[19] A method for determining the dissipated power in DBD's was proposed by Manley who derived the power formula which relates the dissipated power to the operating frequency, the applied peak voltage and some discharge properties. [20]

Throughout the century the applications of DBDs grew, they went on to being used excimer lamps, CO_2 lasers and one of their most well-known applications to date, plasma TV's. This is only brief insight into the history of DBDs, more comprehensive histories have been provided by Kogelschatz & Fridman. [21], [22]

2.5.2 Basic configurations of DBDs

Dielectric barrier discharges (DBD's) generate plasma between adjacent electrodes.

A characteristic of such devices is that they have one or more dielectric insulator layers to separate the electrodes, this layer impedes the transition from glow-arc discharge and the formation of thermal arcs (Discussed in section 2.3). This dielectric layer also prevents plasma formation under DC excitation, as DC current is effectively blocked by the insulating material which forms a capacitor. Thus plasmas generated in a DBD configuration rely on pulsed or alternating high voltage excitation, which results in a displacement current in the dielectric

[23]. DBD's and SBD's at atmospheric pressure are usually operated with applied voltages reaching magnitudes of several kV and frequencies ranging from mains frequency to ~10 MHz. [3], [23] Operating frequencies in the 10-50 kHz range were used in this study, thus there is little impact of frequency over this range.

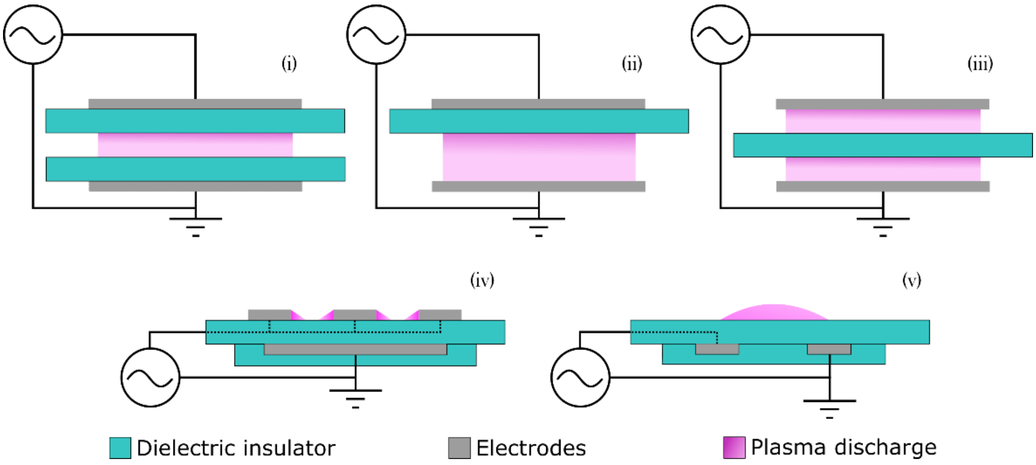

Figure 5: Different configurations of dielectric barrier discharges.

Different configurations of dielectric barrier discharges based on the classic parallel plate discharge arrangement are presented in figure 5 (i-iii), these are considered volume discharge devices as breakdown occurs across a gas gap. [3] Over time developments in dielectric barrier discharge (DBD) design led to the surface barrier discharge (SBD) configurations for generating non-thermal plasmas along the dielectric surface, as seen in figure 5 (iv, v). A typical SBD employs two metallic electrodes adhered to either side of a dielectric surface, on application of a sufficiently high voltage, plasma forms in the region where the electric field is the highest which is typically at the electrode edges. [6], [24]

2.5.3 Dielectrics

Dielectric materials are essentially insulators, but they have a unique reaction to externally applied electric fields, which causes these materials to become polarised. On application of a potential difference across the material, on an atomic scale, the positive charges in the material are slightly shifted in the direction of the electric field while the opposite occurs with the negatively charged electrons. This property of induced polarisation allows such materials to support electrostatic fields compensating for the externally applied electric field.

Each dielectric material has a dielectric constant, this refers to the amount of polarization that occurs and thus the ability of the material to concentrate electrostatic field lines. Materials with a large dielectric constant are able to induce a greater amount of polarisation. If the externally applied electric field is too great, then dielectric breakdown can occur in which the material begins to conduct current. A parameter known as the dielectric strength defines this limitation and should be considered when choosing the dielectric in SBD construction. Table 1 shows some insulator materials with their corresponding dielectric properties.

Table 1: Examples of dielectric insulators with their corresponding constants & strength

Dielectric material	**Dielectric constant**	**Dielectric strength** $\mathbf{10^6 V/m}$
Air	1.0006	3
Paper	3.7	16
Nylon	3.4	14
Porcelain	6	12
Quartz	3.78	8

One thing to note is that most of the surface barrier discharge devices seen throughout the following chapters, use quartz as the dielectric barrier in their construction. Quartz was chosen not only for its dielectric properties, but also for its low loss tangent and due to it being chemically inert thus preventing etching that would take place quickly with materials such as paper.

2.5.4 Discharge modes

DBD's can operate in different discharge modes depending on the composition of the gas in the discharge gap, ambient pressure and/or the characteristics of the drive signal. Diffuse mode discharges, as shown in figure 6(a), have been achieved under helium rich environments while filamentary mode discharges, as shown in figure 6(b), are usually achieved in the presence of oxygen or in air as is the focus of this contribution.

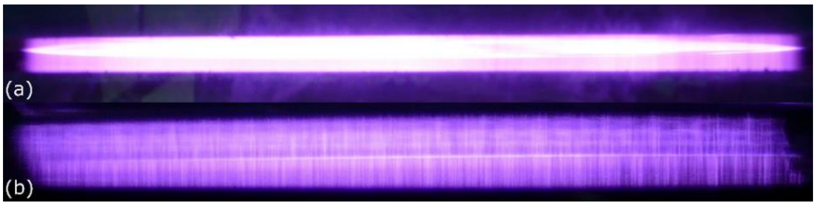

Figure 6: (a) Diffuse discharge mode & (b) Filamentary discharge mode in a volumetric discharge configuration [25]

2.5.5 Streamer/microdischarge formation

Operation of a DBD at atmospheric pressure in air typically results in breakdown in the form of many transient microdischarges, observed as bright filaments travelling across the gas gap in a volume discharge configuration or across the dielectric surface near the electrode edges in a surface barrier discharge. These filaments occur due to an avalanche-to-streamer transition summarised in figure 7.

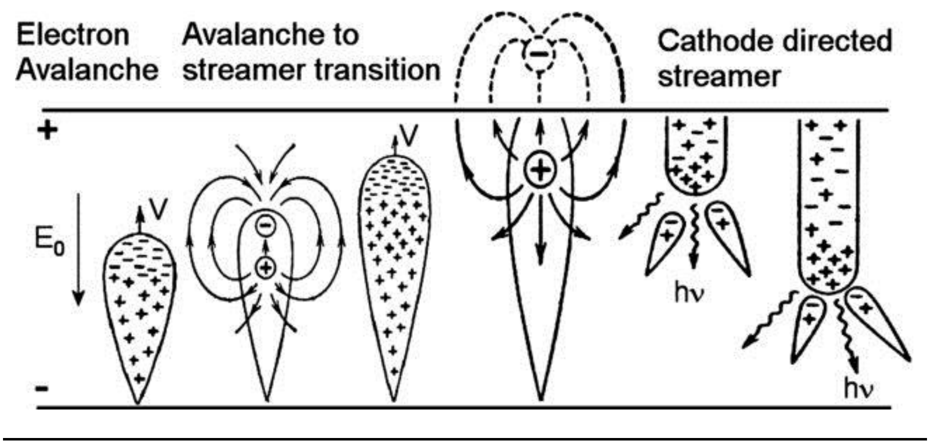

Figure 7: Evolution of the electron avalanche to streamer formation. [26]

On application of a potential difference across the electrodes at/above the breakdown voltage (≥V_B), the local electric field caused by the charge accumulation from electron avalanches is in the order of the external electric field. This results in the formation of thin weakly ionised plasma channels/streamers that propagate, in the case of DBD's, across the discharge gap over a few nanoseconds. Streamers can be classified as cathode directed/positive streamers where the streamer forms at the anode and propagates towards the cathode as seen in figure 7 or Anode-directed/negative streamers in which the contrary occurs. Secondary avalanches that are initiated from the additional electric fields from space charges created by the primary avalanches account for the growth of these streamers. Charge accumulation on the surface of the dielectric takes place, as electron current flows through the ionised channels bridging the dielectric-dielectric surfaces in DBDs or electrode-dielectric surfaces in SBDs. This causes the localised electric field to collapse, preventing the formation of new avalanches and streamers in the vicinity until the polarity of the external electric field is reversed. Charge deposition on the surface of the dielectric material and from residual charges left by the discharge channels, leads to future avalanches and streamers at the same position once the polarity of the applied voltage reverses, through a process known as the memory effect. Observation by the naked eye of individual localisd filaments is possible in DBD’s due to this memory effect, observed as groups of microdischarges at the same position as a single filament. [22], [26], [27]

The microdischarges can be observed as current spikes when measuring the displacement current waveform of the drive signal, which is very useful when trying to accurately determine the breakdown voltage.

2.6 Cold plasma devices

The design and development of cold plasma devices for intended biomedical applications has been the focus of many studies in recent years. [28]–[34] Most research into biomedical applications of cold plasma devices focus on either jets or barrier discharges. Atmospheric pressure plasma jets (APPJ) are used in numerous investigations in plasma medicine, for applications such as wound healing or microbial decontamination. [35]–[37] These devices generate plasma in open space rather than being confined to a discharge gap, thus allowing for direct treatment of an object and at the same time removing any limitations on the size of the object to be treated. But they come with several drawbacks, APPJ’s require a gas input and are limited in the surface area that they are able to treat, as the plume cross sectional area is often <cm^2. Different methods have been implemented to try and extend the cross-sectional area, such as arraying multiple devices, but gas flow constraints and the ability to to uniformly treat large areas is still a limited.

Barrier discharges, such as the SBD pose a viable means of combating issues presented by APPJ’s, SBD’s can be designed to be scalable as demonstrated by Morfill et al [38] allowing for large area treatments to be achieved. Despite their promise, inherent limitations of the SBD configuration exist, as many of the highly reactive species are confined to the active discharge region, *i.e.* visible plasma domain, near the surface of the dielectric as discussed in section 2.7. SBD's are sometimes referred to as surface micro discharge (SMD) devices and have been developed using different electrode geometries and materials. These devices are usually all based around the basic SBD configuration seen in figure 5. There are numerous examples of such devices developed for decontamination purposes in recent studies, these are usually designed with either the intention of generating large area uniform plasma discharges, such as mesh devices, [39]–[42] or with electrical safety in mind as seen by devices that utilise an embedded electrode configuration as to prevent any thermal arc discharges. [43]

The design of SBD's for biomedical applications such as decontamination or wound therapy must have safety in mind, especially when the plasma discharge is intended to come into close contact with living subjects. [30], [44] In the following chapters, this issue is addressed by covering the high voltage electrodes with an insulator and by forming the plasma discharge solely on the grounded electrode, thus making contact with the plasma possible without the risk of electrical shock. Obviously when it comes to the design and development of an SBD, its intended application must be in mind, if the device is to be used directly onto a target/specimen in open space then portability of the device is required. Ni *et al* [45] recently presented such a device that is handheld for the treatment of water, seen in figure 8(a). For closed systems, seen in figure 8(b), where the discharge is confined in an enclosure in which the target/specimen is also placed portability is often not a necessity but factors such as enclosure/chamber volume require consideration. Also if the intended application is to treat a specimen such as a biofilm or a liquid media, then the efficiency can be affected by the distance of the gas gap between the discharge and the surface of the target.

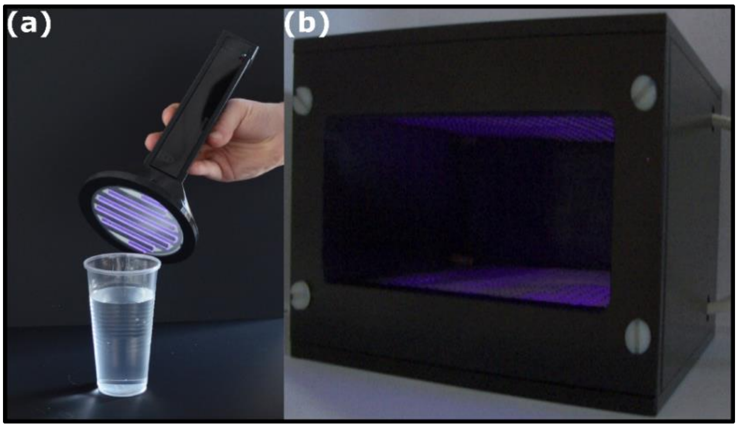

Figure 8: Examples of a (a) handheld portable plasma device & (b) an enclosed plasma “dispenser” based on SBD configurations for applications in microbial decontamination. [38], [45]

2.7 Reactive oxygen & nitrogen species generation

Plasmas generated far from thermodynamic equilibrium in humid air at atmospheric pressure produce large densities of Reactive Oxygen and Nitrogen Species (RONS). [46]–[48] Ionization of the ambient gas generates a variety of positively/negatively charged particles that lead to the generation of these reactive species. Table 2 presents some of the species likely to be generated and considered in a numerical model of an atmospheric SBD discharge in humid air, presented by Sakiyama *et al.*

In surface barrier discharges and other DBD’s there exists domains/boundaries by which certain charged particles & species are confined. Charged particles along with the highly reactive neutral species shown in group (a) of table 2 are confined to the visible plasma domain, due to their short lifespans (<10 μs). Reactive species shown in group (b) are longer-lived, they are therefore able to diffuse into the afterglow region.

Table 2: Charged particles and species generated by a surface barrier discharge in air. [46]

Positively charged particles	**$N^+, N_2^+, N_3^+, N_4^+, O^+, O_2^+, O_4^+,$ $NO^+, N_2O^+, NO_2^+,$ $H^+, H_2^+, H_3^+, OH^+, H_2O^+, H_3O^+$**
Negatively charged particles	$e, O^-. O_2^-, O_3^-, O_4^-,$ $NO^-, N_2O^-, NO_2^-,$ NO_3^-, H^-, OH^-
Neutral species	
Group (a)	$N(^2D), N_2(A^3\Sigma),$ $N_2(B^3\Pi), O(^1D), H, N, O$
Group (b)	$O_2(a^1\Delta), O_3, NO,$ $N_2O, NO_2, NO_3, N_2O_3,$ $N_2O_4, N_2O_5, H_2, OH, HO_2,$ $H_2O_2, HNO, HNO_2, HNO_3, N_2, O_2, H_2O$

With the exception of aerodynamics and the cooling of electronics, most applications of the SBD rely upon the fluxes of reactive species generated from the plasma discharge. These reactions can be highly beneficial in accelerating reactions in plasma catalysis applications or the oxidation of bacteria for decontamination purposes in plasma medicine applications.

Taking into account species generated from an SBD for applications in decontamination or surface treatment etc. We only consider medium-long lived species as these applications rely on the diffusion/convection of species from the visible plasma to a downstream location (target) which will be discussed in the upcoming section on plasma induced flow.

2.7.1 Ozone poisoning

A phenomenon known as ozone poisoning can occur when barrier discharges are confined in a sealed volume. With increasing power supplied to a confined discharge, ozone generation increases up to a certain point, followed by a rapid reduction in ozone density. This phenomenon is accompanied by a drastic increase in RNS generation.

Despite over 100 years of active research into ozone generation, the exact origins of this transition remain unexplained. The phenomenon was investigated by Shimizu et al who presented a study on the dynamic behaviour of ozone production for an SMD air plasma. Ozone concentration was shown to increase over time with input power densities up to ~0.1W/cm2 but with greater input powers ozone density was seen to decrease ~10s after initiation, as seen in figure 9. It was hypothesised that the transition may occur due to reactions between vibrationally excited nitrogen molecules $\left(N_2(\nu)\right)$ and O atoms leading to the accelerated production of nitric oxide NO, which is a major quencher of ozone reacting to produce NO_2 which further reacts with ozone to produce NO_3. [49]

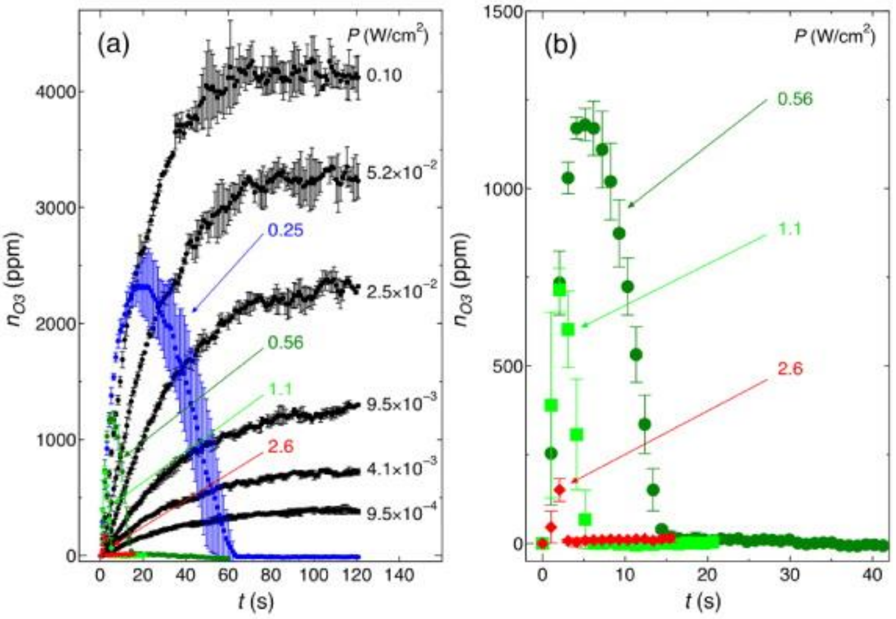

Figure 9: Time evolution of ozone density for different input powers (a) <0.56 W/cm^2 & (b) >0.56W/cm^2. [49]

Another factor that can effect ozone generation and poising is temperature, this has been shown in previous studies with air fed DBDs, in which ozone poisoning is shown to occur by drastically increasing feed gas temperature. [50], [51] in chapter 4, this phenomenon will be further investigated using a more efficient method of controlling the transition that does not require extreme temperatures in an attempt to explain some of the underpinning mechanisms that are involved. Understanding this phenomenon is vital when it comes to the design and development of barrier discharges for decontamination purposes, as the optimum composition of RONS necessary to achieve high antimicrobial efficacy remains unknown.

2.8 Gas phase species analysis

An important aspect when developing any type of cold plasma device for a given application is understanding the plasma nature. It is well known that species generation in cold plasma are directly affected by the gas composition of the environment in which the discharge is formed. As this contribution is focused on surface discharges in ambient air, only literature based on air-fed discharge chemistries or studies that use applicable diagnostic techniques are discussed.

The main species that are found in the discharge region and post discharge 'after-glow' of SBDs operating in air include O_3, NO, NO_2, N_2O, N_2O_5, HNO_2, HNO_3, OH & H_2O_2. Along with experimental measurements using advanced gas analysis techniques, these species have been identified through numerical simulations. [52] Gas phase species measurements have been extensively carried out in an attempt accurately determine the composition of RONS in the plasma effluent and better understand the chemical pathways that lead to reactive species generation. The computational model of Sakiyama *et al* is a prime example that considers 624 reactions resulting from the interactions between 53 species including electrons, ions and neutral species. [52] To gain an insight into the densities of reactive species generated from air fed discharges, advanced diagnostic techniques have also been used in numerous investigations. [53], [54] Spatiotemporal inhomogeneity due to the discharges being confined to small areas on the dielectric pose a challenge when using these techniques.

2.8.1 Fourier transform infra-red spectroscopy

Fourier transform infra-red (FTIR) spectroscopy is one of the most widely used analytical techniques used in characterising and determining concentrations of various gas phase species generated from air fed plasma discharges. [39], [47], [55] Through the transmission of a known range of the infra-red spectra across a gaseous sample FTIR spectroscopy is able to detect the absorbed wavelengths, which are specific to the vibrational bonds of a molecule , thus enabling the composition of the sample to be determined. Al-Abduly *et al* presented a study of the plasma glow and downstream chemistry of an air fed DBD in which FTIR spectroscopic measurement were made. [53] An example FTIR spectra collected from this investigation is presented in figure 10 along with a table of assignments of various features observed in the spectra collated from multiple sources, in table 3.

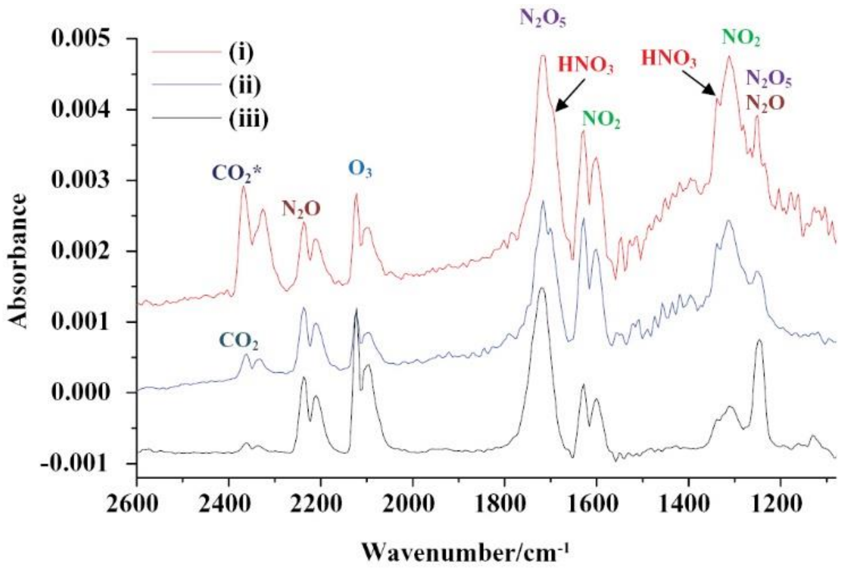

Figure 10: FTIR spectra of an air fed DBD with (i) ambient air, (ii) humid artificial air & (iii) dry artificial air. [53]

Table 3: Assignments of reactive species to their corresponding spectral bands. [53]

Wavenumber/cm^{-1}	Associated species	Reference
2326,2366	$CO_2^*(v)$	[53]
1300, 2211, 2237	N_2O	[56]
1055, 1030, 2098, 2121	O_3	[57]
1247, 1720	N_2O_5	[56]
1313, 1341, 1700	HNO_3	[56]
1600, 1627	NO_2	[56], [58]
2360, 2340	CO_2	[59]
2176, 2121	CO	[59]

Although such studies have demonstrated that the FTIR analysis technique can effectively be used to measure gas phase species, they are usually performed on plasma discharges that are confined in a closed space. Consequently, the ability to obtain spatially resolved measurements of downstream species and the characterisation of barrier discharges operated in free space in limited. The FTIR method is usually used to provide an insight into the concentration of long lived species, such as O_3, NO_2 & N_2O. As the majority of reactors rely on convection of species from the discharge to a gas cell placed within the FTIR system, little insight is gained into the nature of species with a shorter lifespan, such as NO. [45]

2.8.2 Laser Induced fluorescence spectroscopy

Laser induced fluorescence (LIF) is a more species-specific approach of gas phase analysis. This technique allows for spatially resolved density measurements of individual reactive oxygen and nitrogen species (RONS), present in the gas phase of cold plasma discharge, in free space or in a confined environment. It is a combination of absorption and emission spectroscopy, in which a laser is finely tuned to a certain wavelength usually to excite a chemical species from a ground state energy level to a higher electronic energy state. On transition back to a lower energy state, photons of light at a different wavelength specific to the rovibrational transition of a molecule are emitted, that can then be detected with sensitive imaging devices such as an ICCD camera.

Measurements in the plume of an air fed plasma jet of the absolute densities of OH and NO, which are of significant biological importance, have been demonstrated by Yonemori & Van Gessel et al [54], [60] using such a technique. Part of the investigation conducted by Gessel et al [61] into the generation of NO from a plasma jet looked at fluorescence spectra obtained via a scan of the laser wavelength at around 226 nm, the fluorescence obtained is shown in figure 11. It can be seen from the figure that there are a number of wavelengths at which a higher intensity signal is achieved which is indicative of LIF being a resonant process of matching laser wavelength to molecular energy transition as described above.

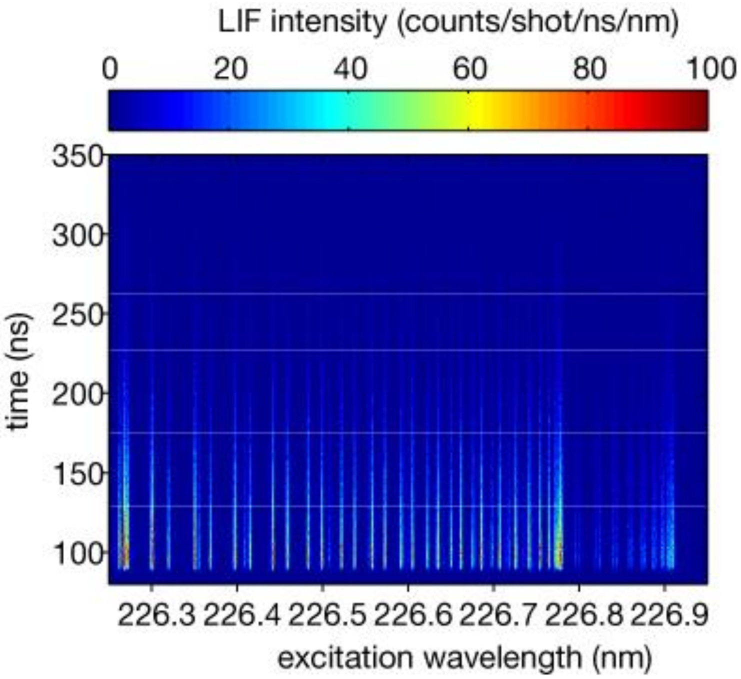

Figure 11: Time and wavelength resolved LIF signal of a helium/air jet. [61]

2.9 EHD induced flow

The electrohydrodynamic (EHD) flow generated from a barrier discharge has been studied for almost a century. The phenomenon has been exploited for numerous applications including the cooling of microscale electronic circuits and industrial processing of chemical materials. [62], [63] This induced flow originates from momentum transfer to heavier neutral particles from ions drifting in the electric field. Flows generated from a surface barrier discharge configuration have proven to be very useful as flow control devices for applications such as aerodynamics in particular. [64], [65]

Taking a simple linear plasma actuator as seen in figure 12, as an example, consisting of two planar electrodes mounted to either side of a dielectric and driven by an sufficiently high enough time varying source to achieve breakdown. Plasma forms along the electrode edge and extends a few mm across the dielectric surface.

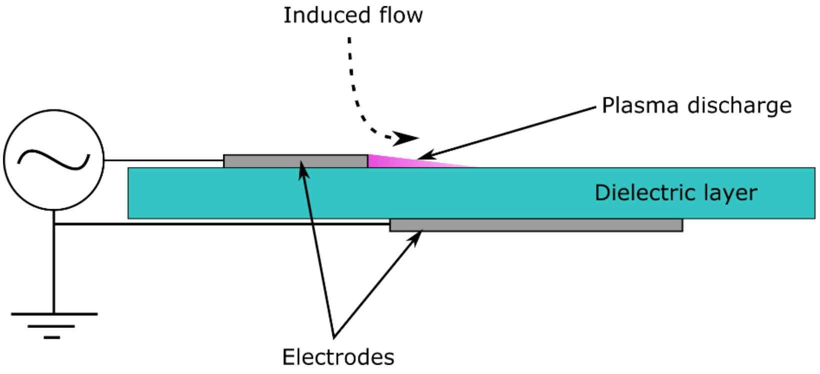

Figure 12: Simple planar SBD design, commonly used for plasma actuators.

An EHD force is established from the formation of a plasma discharge, as charged particles drifting in the electric fields setup by the applied HV signal and streamer discharges, a transfer of momentum occurs through collisions with heavier neutral particles. This leads to an induced flow which is often referred to as an electrical/ionic wind [65], [66] which can reach velocities of a few ms^{-1}, depending on the magnitude of the applied voltage, dielectric material/thickness & electrode geometry [67]. In the example seen in figure 12, the flow travels in the horizontal direction (to the right) across the surface of the dielectric away from the electrode edge, while air above the electrode-plasma interface is entrained into the discharge region.

Many applications require reactive chemical species generated in/near the plasma domain of an SBD to reach a remote location (a few cm from the discharge domain) such as those for the processing of substrates/materials or for the decontamination of pathogenic microorganisms in plasma medicine, which was the focus of this study. These applications rely on the plasma induced flow as a means of transport for reactive oxygen and nitrogen species to a downstream location. [48]

2.9.1 Flow analysis techniques

A number of techniques have been identified to visualise/measure the flow induced by the electrohydrodynamic forces generated from barrier discharge devices. [68] Examples of techniques that have been used in the analysis of flows generated from non-thermal plasmas include: Schlieren imaging seen in figure 13, smoke visualisation and Particle imaging velocimetry seen in figure 14 (a) and (b), respectively. [45], [65], [68], [69]

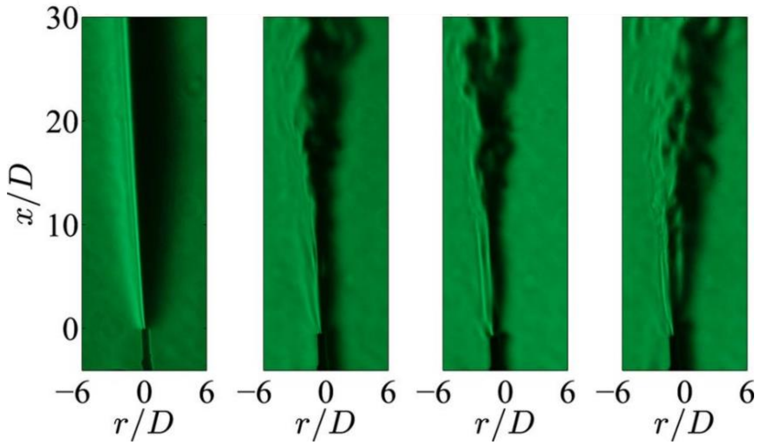

Figure 13: Example of Schlieren imaging used on a non-thermal plasma jet operating under different discharge conditions [69]

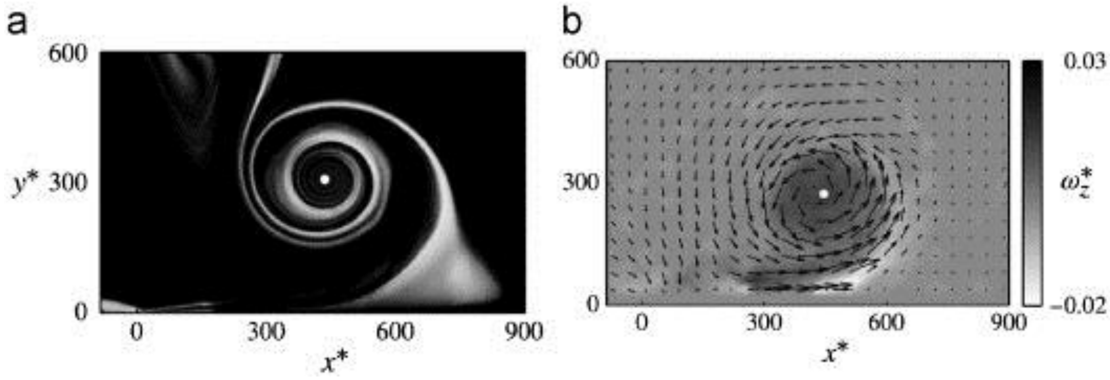

Figure 14: Vortex generated by the plasma induced flow of an SBD device, (a) Smoke-flow visualisation and (b) Particle imaging velocimetry. [68]

Although Schlieren imaging and smoke-flow analysis are useful tools in atmospheric pressure plasma diagnostics, [70] they only provide a qualitative indication of the induced flow , thus cannot be used to accurately gauge the induced velocity. [71] Quantitative measurements can be made using particle imaging velocimetry (PIV) to approximate the flow velocity generated from a discharge to a high degree of accuracy, as demonstrated by R. Whalley et al [65], [67], [69].

2.9.2 Flow manipulation

The mass transportation of plasma activated species from the plasma domain is known to heavily rely on the EHD induced flow. [45], [48], [72], [73] When it comes to the application of an SBD for microbial decontamination the treatment efficiency can be greatly impeded compared to a 'direct' plasma exposure as many of the reactive species generated in the active plasma region are short-lived and do not reach the target. Manipulation of the EHD forces, to increase the convective gas flow through the active plasma region as well as steering of the convective flow, is a viable means to overcome these issues. [45], [74]

Different dielectric thickness, electrode pattern and/or configurations strongly affect the EHD flow, allowing a degree of control. [75]–[79] This is demonstrated in an investigation presented by Moreau et al [67], where a comparison was made of the velocity profiles of the EHD flow between a smooth and serrated linear SBD electrode design. It was found that the serrated electrode edge induced a larger flow velocity than that of the smooth edge as seen in figure 15.

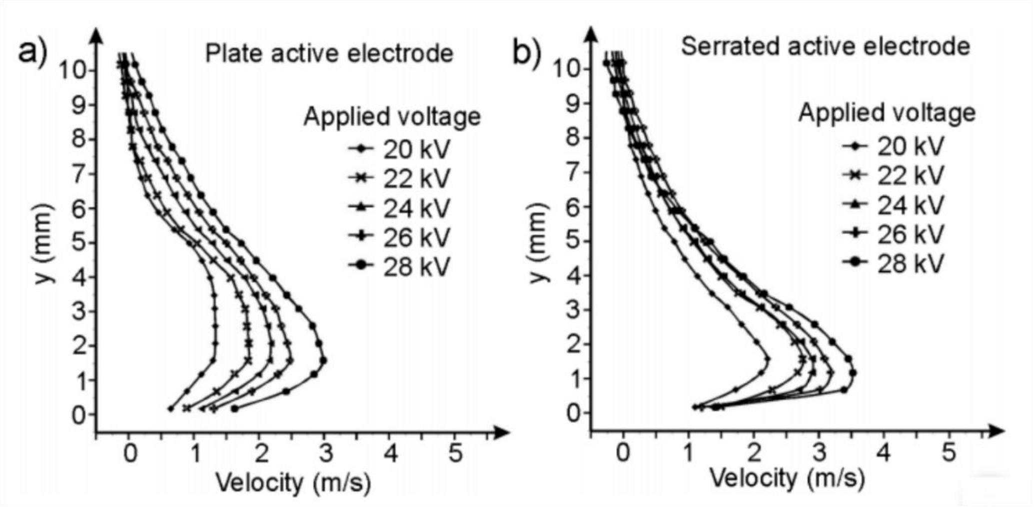

Figure 15: Velocity profiles for a linear SBD design (as seen in chapter 1) at different applied voltages, (a) with a smooth edge and (b) with a serrated edge. [67]

Previous studies have also shown that steering of the convective gas flow can be achieved by altering electrical properties such as changing the amplitude or pulse modulation of the voltage signal applied to one or more adjacent electrodes. [80]–[82] These methods can effectively steer the induced flow but require impeding plasma formation from the electrode(s), thus effecting the density of species. The main driving point behind EHD flow manipulation is for control over the mass transport of species downstream of the plasma domain. As most SBD devices used in decontamination applications only produce a flow in a set direction, being able to effectively steer the flow, allows for a larger and more uniform surface treatment to be achieved.

2.10 Plasma activated fluids

Due to the chemical enrichment that takes place from reactive species diffusing into certain liquid media after plasma treatment, plasma activated fluids (PTF's) have been the focus of many recent investigations. Plasma treatment of a variety of liquid media have been investigated, but water in particular has gained a vast amount of interest due to its readily available nature and the antimicrobial properties it displays once treated. Given this interesting phenomena, numerous healthcare related applications have been reported in recent times. [83]–[88]

2.10.1 Plasma –liquid interaction

In recent years much effort has been made in the field of plasma science and technology to understand the complex underpinning chemical nature of plasma-liquid interactions. [88]–[91] The reactive chemical species and processes found across the gas-liquid boundaries of a relatively simple air plasma was summarised by Kong et al [92] as seen in figure 16. Between the gas phase of the plasma discharge and the bulk of the liquid there lies an interface where a number of chemical reactions/processes occur with the “shorter” lived species. The size of this interface layer can vary from species to species, as different reactive species penetrate different depths depending on their lifetimes.

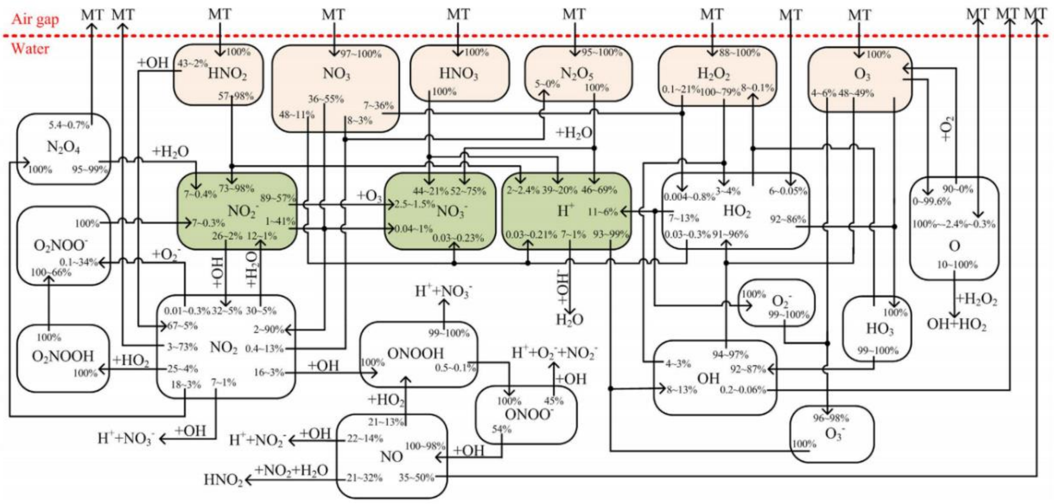

Figure 16: Schematic of reactive species and mechanisms found across the gas-liquid boundaries from non-thermal air plasma treatment of water. [92]

A variety of diagnostics techniques have been carried out on water/liquids before and after plasma treatment to discover what reactive species are present and to try and to ascertain the chemical reactions that take place at the gas-liquid boundary. A review conducted by Bruggeman al [88] identified the key species involved in these plasma –liquid interactions along with a comprehensive insight into the challenges faced when looking into this area of research.

2.10.2 Liquid phase analysis

To detect and quantify the concentrations of the various chemical species found in fluids such as water after plasma treatment, a number of chemical analysis techniques have been investigated. Some of the species found to be present in PTFs through experimental measurements include $O_3, NO_2^-, NO_3^-, HNO_2, HNO_3, H_2O_2$ & OH. [93] A number of these species can be measured through colourimetric tests, as they react with certain reagents, some common examples are given in table 4.

Table 4: Common reagents for colourimetric test in PAW species diagnostics.

Reagent	**Reactive species**	**Reference**
Griess reagent	Nitrites	[93]–[95]
Titanium oxysulfate	Hydrogen peroxide	[93], [95]
Indigo trisulfonate	Ozone	[96], [97]

Acidification is a common characteristic of plasma treated fluids. With time the pH of water has been shown to decrease, reaching relatively low values. [93] The source of this acidification is considered to be as a result of both nitrite and nitrate formation, as seen in figure 17. [98]

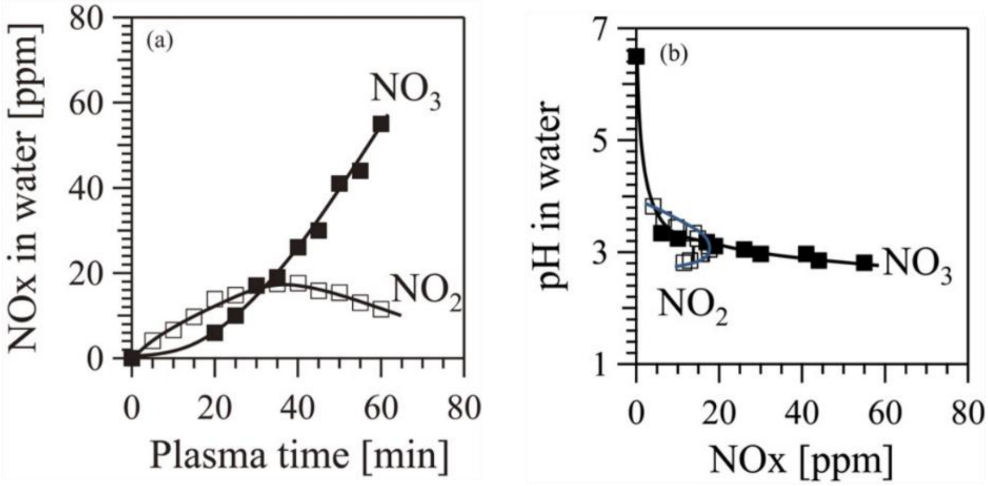

Figure 17: Nitrate & nitrite concentrations in PAW (a) NOx vs time, (b) pH vs NOx. [98]

2.10.3 Bactericidal species

Determining the chemical species that are the cause of the antimicrobial activity displayed by certain plasma activated media, poses many challenges due to its complex chemical makeup. This has been a topic of interest in a number of investigations. [93], [99] In recent literature on this topic acidified peroxynitrite has been identified as a crucial bioactive species that can be found in water samples after plasma treatment. But this area is still up for debate. Much of the research indicates a synergistic effect between certain plasma generated species previously mentioned in the liquid media. [85], [93], [100]

2.11 Decontamination via non-thermal plasma treatment

Over the past decade research into applications of non-thermal plasmas for microbial decontamination applications within both industrial and healthcare sector has been vast. [45], [93], [101]–[108] The bactericidal properties of certain active species generated by cold plasmas has made microbial decontamination one of the most widely investigated application in the field. [104], [108]–[111] As was discussed in previous sections, efforts have been made to tailor cold plasma devices to generate specific reactive species under different operating conditions. This is directly relevant in decontamination of microorganisms as different strains can be more susceptible to certain plasma species than others. [112]–[114] Table 5 lists some of the most common bacterial strains investigated in cold plasma decontamination applications.

Table 5: Common strains used to investigate the efficiency of DBD discharge plasmas for decontamination.

Microorganism	Reference
Salmonella	[115]
Escherichia coli	[115]–[117]
Pseudomonas aeruginosa	[105], [118]
Staphylococcus epidermidis	[118]
Staphylococcus aureus	[107]

Another factor that can influence the efficacy of non-thermal discharges in microbial decontamination is the characteristic formation of the microorganism, i.e. whether it exists in a planktonic state or in a biofilm. Microorganisms in a biofilm display more tolerance to external influences, as they live in a complex microbial community which is enclosed in a matrix of extracellular polymeric substrate (EPS), seen in figure 18. [119] As biofilms account for ~ 80% of all chronic infections worldwide and the number of drug resistances in these communities are growing, non-thermal plasma technology as a means of biofilm control has been the focus of many recent studies. [120]–[124]

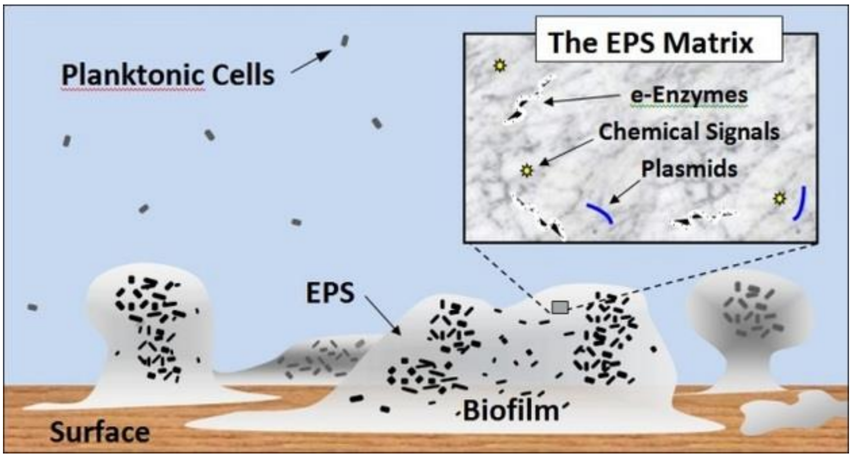

Figure 18: Illustration of the characteristics planktonic sate microorganisms and biofilms. [125]

2.11.1 Direct & indirect plasma treatment

Within the recent literature, bacterial treatment with non-thermal plasma is usually categorised as either direct or indirect. In the case of direct treatments, the decontamination target is usually placed within the visible plasma domain, thus is exposed to large fluxes of shorter-lived species. Direct treatments are most common in volumetric DBD configurations where the target specimen is easily placed between the adjacent electrodes. Conversely, treatments with a SBD configuration are considered indirect as they involve the decontamination target being exposed to the discharge effluent carried by the EHD induced flow as mention previously, thus receiving fewer doses of short-lived species. Fridman and colleagues presented a comparative study of these two treatment modes. [100]

2.11.2 Hazards

Understanding the ways in which plasma and its effluent react with a biotic or abiotic target is of vital importance when it comes to the field of plasma healthcare, especially in the field of plasma assisted wound healing. As discussed, safety is of high priority, any potential hazardous effects that a plasma treatment may induce is of great concern. This has led to a number of different studies being performed that focus on plasma treatment effects and related topics. [126], [127]

2.12 Summary

This brief review has provided an account of recent research into the RONS generation and transportation mechanisms in a surface barrier discharge and highlighted key applications of such non-thermal devices in microbial decontamination. Analysis of the reactive chemistries in the gas phase of such discharges has been well established for longer living RONS, and efforts have been made in determining the underpinning mechanisms involved in their creation. Several key RONS have been quantified using different techniques, such as FTIR spectroscopy and laser induced fluorescence. It was observed that the operating conditions of the plasma can affect the densities of different species downstream of the discharge. Methods of manipulation over the EHD forces that induce flow within the discharges were discussed as a means of control over the mass transport of species. A number of studies have been highlighted that look at the antimicrobial efficacy of non-thermal plasma devices on different microorganisms. The majority of these are based on planktonic state bacterium but there has been a recent emergence in studies focusing on biofilms.

Chapter 3: Methodology

3.1 PIV measurement technique

In order to quantify the flow field created by the plasma, particle imaging velocimetry (PIV) was used in a number of the investigations discussed throughout this contribution. The PIV technique employs a pulsed laser formed into a sheet to illuminate fine oil droplets within the measurement domain. A high-speed camera is used to capture one laser pulse per frame and a cross correlation technique is used to track the displacement of particles between consecutive frames. The precise timing between laser pulses and the measured displacement of particles enables velocity vectors in 2D space to be calculated. PIV measurements were undertaken using the experimental setup shown in figure 19. The SBD was inserted into a large chamber (volume > 2 m^3), which was seeded using oil droplets with a nominal size of 1 µm. To prevent any influence on the plasma generated flow from external draughts the chamber was sealed for all measurements. The Stokes number of the seeding particles used throughout the study was < 0.1, thus ensuring that the particles followed the fluid flow closely with tracing errors being < 1%. [69] A double pulsed Nd:YLF laser operating at 400 Hz with a pulse duration of 100 ns and wavelength of 527 nm was used to generate a light sheet that was projected into the seeding chamber and across the SBD electrode. A high-speed camera (Phantom Miro Lab 340) was positioned outside the seeding chamber perpendicularly to the laser sheet and synchronised with the laser such that each frame captured a single laser pulse. A spatial calibration was performed and the time delay between consecutive laser pulses (Δt) was set to 20 µs, a value chosen to capture the movement of oil droplets over a square grid with spatial resolution of 56 µm, enabling the velocity vectors to be computed using a recursive cross-correlation technique. For each dataset, 800 frames were recorded and used to make 400 individual vector maps; in the case of time averaged measurements all 400 vector maps were averaged and presented as a single figure.

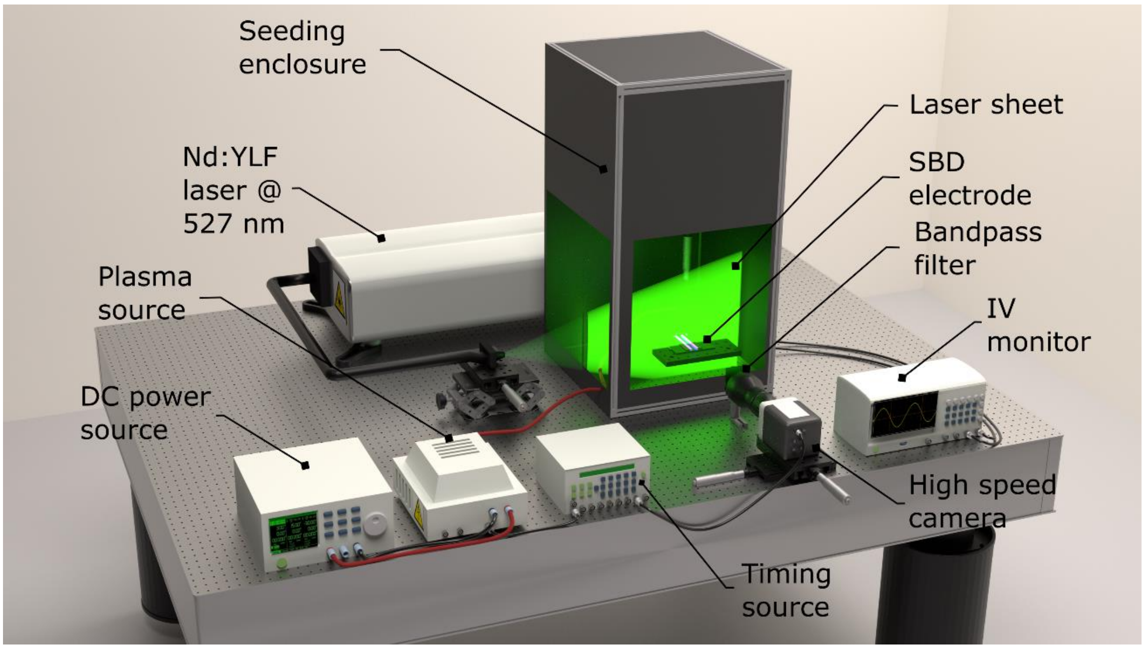

Figure 19: Schematic showing arrangement of the Particle imaging velocimetry system for measurement of velocity flow fields.

3.2 Gas phase species measurements

Analysis and quantification of the gas phase species was conducted in a number of investigations discussed throughout this contribution using two different approaches identified in the literature review. FTIR was used for determination of the long-lived reactive chemistry, while LIF was used in the analysis and quantification of NO in the gas phase of a SBD.

3.2.1 FTIR measurement technique

An FTIR spectrometer (Jasco FT/IT-4000) with a mid-IR optical bench from 7800cm-1 to 500cm^{-1}, was used to measure the IR absorption spectra of the gas-phase species in the plasma effluent. The resolution of the data acquisition was set to 8 cm^{-1} and each spectra was comprised of 15 individual scans averaged, for each measurement.

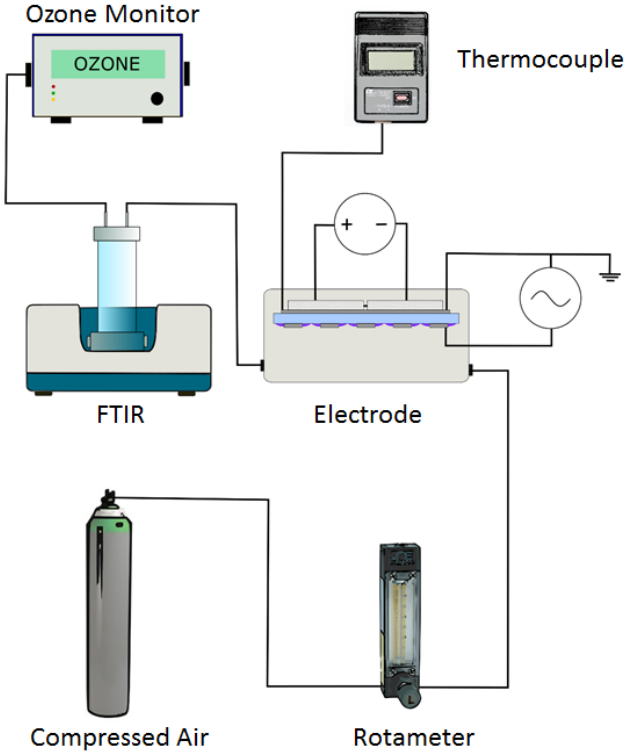

Figure 20: Illustration of Fourier transform infrared spectroscopy setup used for gas-phase analysis of surface barrier discharge.

The longer living plasma species produced by the plasma were driven by compressed air into the FTIR gas cell (16 m path length) with the aid of the input air feed into the enclosure in which the discharge formed, shown in figure 20. Absorption spectrum measurements of the long-lived species were performed for each of the powers and corresponding temperatures under investigation. After each spectral acquisition the whole system was flushed for 5 minutes with the compressed air in order to purge any remnant effluent that may be present. Real time spectral analysis was performed alongside each purge to confirm the absence of any plasma generated species.

Standard reference profiles obtained from the Pacific Northwest National Laboratory (PNNL), [128] were used to fit the absorption peaks for each of the molecules seen in the FTIR spectrum measurements. This enabled the concentrations of individual gas phase species to be estimated using equation (3.1), derived from Beer lamberts law. [129]

$$C = A/(B \times l) \tag{3.1}$$

Where C is the concentration of a specific gas molecule (PPM), A is the area of the corresponding absorption peak for the gas molecule, B is the peak area from the corresponding reference data and l is the difference between the experimental gas cell path length and that used in the standard reference (1 m).

A ozone monitor (2B technologies model 106M) was connected to the exit of the FTIR gas cell to obtain time resolved concentration measurements of ozone in the exhaust gases. The recorded ozone data was compared against the FTIR analysis as a means of validation.

3.2.2 LIF measurement technique

The LIF measurement system is shown in figure 21. A dye laser (Sirah Cobra Stretch with second harmonic generation (SHG) unit) was pumped by a 5 ns pulsed Nd:YAG laser with a wavelength of 355 nm at a repetition rate of 10 Hz. The dye laser with a line bandwidth of 0.04 cm^{-1} was tuned to generate an output at a wavelength around 226.263 nm to excite the P1(4) and R2(11) rotational states of ground state NO molecules, the transition NO X(v''=0) → A(v'=0). The laser wavelength was scanned across the transition to achieve the highest intensity LIF signal thus determining the wavelength at which the maximum ground state NO excitation occurs. Parasitic effects that can affect the LIF signal and therefore require consideration have been identified in recent work. [130] No fluorescence signal was detected from the dielectric surface or in the discharge gap when the plasma was off, indicating that any parasitic effects from spurious laser scattering can be neglected in our analysis. The photoemission of charged species such as NO(A) produced in the discharge was also considered to be unimportant due to the low energy of the laser used in the experiments and the fact that NO excitation is a resonant process. Other possible parasitic effects were tested by shifting the laser wavelength by more than 5 pm away from the centre of the transition at 226.263 nm. Detuning the laser wavelength from the centre of the transition resulted in no fluorescence signal detection, thus other parasitic effects that can disturb the LIF measurements can also be neglected.

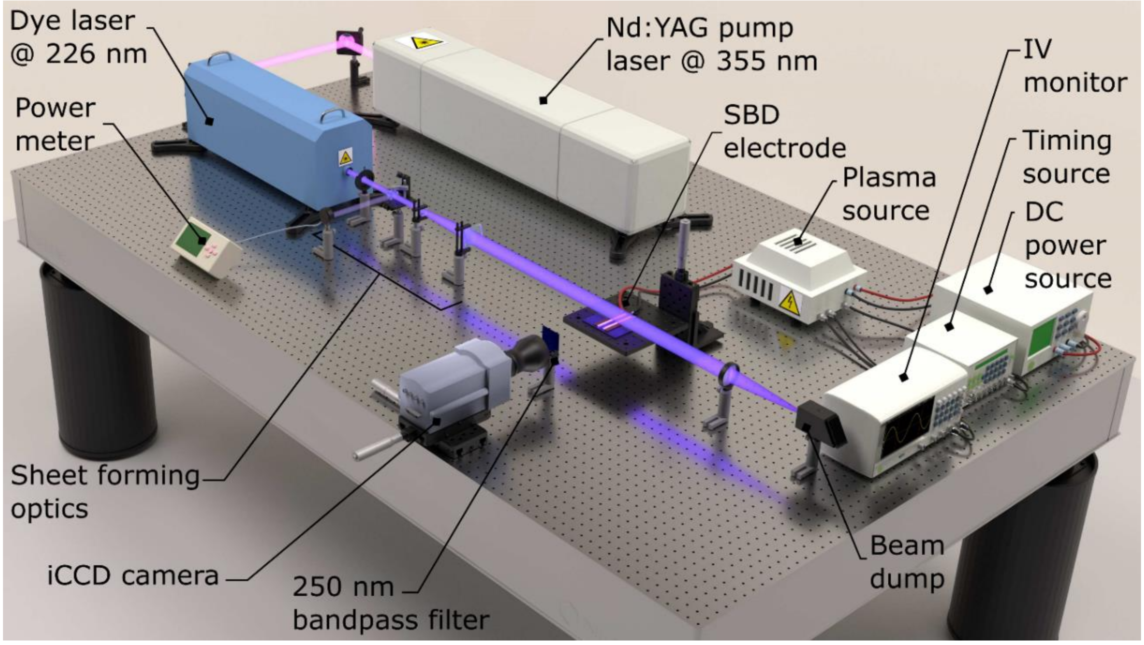

Figure 21: Schematic showing arrangement of laser induced fluorescence system for measurement of ground state NO.

The laser pulse energy was monitored in real-time using an Ophir PE-9 laser energy meter and was kept within the range of 0.07 - 0.1 mJ. Using a cylindrical lens (with 100 mm focal length), the dye laser output was converted into a 13 mm sheet propagating perpendicularly above the discharge. The slight divergence of the laser beam after the cylindrical lens was neglected. To capture the fluorescence of excited NO molecules, an Andor iStar740 iCCD camera was fitted with a UV Nikkor 50 mm imaging lens via an optical bandpass filter. The filter had a full width half maximum bandwidth of 10 nm and was used to capture the fluorescence signal at ~248 nm corresponding to the NO transition of A(v''=0) → X(v'=2). The camera arrangement was positioned to face the centre of the discharge gap between the two driven electrodes. For each image recorded the iCCD camera was configured to accumulatively capture 40 laser pulses, using an optical gate width equal to 30 ns for each exposure. All images of the LIF signal were corrected for background noise and plasma emission prior to analysis of the results. The divergence of the laser sheet was determined to be 15.7 mrad due to the presence of the sheet forming optics; over the camera field of view, this level of divergence was found to be negligible hence no correction of the data was applied.

A calibration procedure described in detail by Van Gessel *et al*. [60], [61] was used to convert the fluorescent signal in to the NO number density within the region of interest. To obtain calibration data, an experimental setup with the same optical elements and the same detector position was used with the exception of the SBD being replaced with a sealed chamber filled with ultra-pure helium at pressures of 300, 500, 700, and 900 mbar plus an admixture of 100 ppm of NO. Multiple He/NO pressures were used to account for possible reflections from inside the chamber. The LIF signal accumulated by the ICCD camera was corrected for the laser energy, according to equation (3.2)[61]:

$$\boldsymbol{I_{LIF}^{cal} = \frac{I_{LIF}^{0}}{E_L \eta_{226} \eta_{248}}} \qquad (3.2)$$

Where $\boldsymbol{I_{LIF}^{0}}$ is the LIF signal intensity per pixel measured as an average value over a region of interest, $\boldsymbol{E_L}$ is the laser energy while $\boldsymbol{\eta_{226}}$ and $\boldsymbol{\eta_{248}}$ are the transparency of the windows of the vacuum chamber used for the laser beam pass and fluorescence signal detection, respectively. Using this parameter, the NO concentration, $\boldsymbol{n_{NO}}$, in the discharge was calculated using equation (3.3)[60], [61]:

$$\boldsymbol{n_{NO} = \frac{I_{LIF}^{SBD}}{I_{LIF}^{cal}} \frac{\tau_{cal}}{\tau_{SBD}} n_{NO}^{cal}} \tag{3.3}$$

Where $\boldsymbol{I_{LIF}^{SBD}}$, is the LIF signal measured from the SBD discharge normalised to the laser energy and corrected for O_3 absorption, $\boldsymbol{n_{NO}^{cal}}$ is the known density of NO in the calibration mixture, $\boldsymbol{\tau_{SBD}}$ (s) and $\boldsymbol{\tau_{cal}}$ (s) are the LIF signal (*i.e.* fluorescence) decay time in the discharge and in the calibration chamber respectively. [61], [131]–[135] The required decay times $\boldsymbol{\tau_{SBD}}$ (s) and $\boldsymbol{\tau_{cal}}$ (s) were estimated based on known densities of the quenchers (He, N_2, O_2, H_2O, NO, O_3) in the discharge and the calibration cell and known rate coefficients given elsewhere. [61]

3.3 liquid-phase species measurements

The investigation discussed in chapter 8 required liquid phase diagnostics to be performed in order to quantify the concentrations of certain species in plasma activated water samples. Dissolved ozone in these samples was measured using the indigo technique which relies on the rapid discoloration of indigo trisulphide reagent by ozone, such that UV absorption measurements at 600 nm has a linear trend with ozone concentration *i.e. a* higher concentration of ozone gives a decrease in the measured absorption. Two methods were used to calculate the concentration of ozone using the indigo technique: [136]–[139]

Volumetric: $$mg\ O_3/L = \frac{100 \times \Delta A}{f \times b \times V} \tag{3.4}$$

Gravimetric: $$mg\ O_3/L = \frac{(A_B \times 100) - (A_S \times V_T)}{f \times V_S \times b} \tag{3.5}$$

Where ΔA is the difference in absorbance between the plasma treated sample and the untreated control, b is the path of the cell (cm), V is the PAW sample volume (mL), f is the absorption coefficient (0.42), A_B is the absorbance of the untreated control, A_S is the absorbance of the plasma treated sample, V_S is the volume of the plasma treated sample, V_T is the total volume of the treated sample and the indigo reagent. The quantitative measurements of the generated nitrites (NO_2^-) and nitrates (NO_3^-) species in the PAW were performed via high-performance liquid chromatography (HPLC). Any changes in pH & conductivity that occurred due to the generation of chemical species in the water were recorded using a Five Easy pH meter from Mettler Toledo & a H98311 Conductivity and Temperature Meter (0-3999S, 0-60C) from Hanna Instruments.

3.4 Numerical model

A numerical axisymmetric plasma model was developed and implemented using COMSOL, version 5.2a, by Dr Hasan [140]–[142], to uncover the underpinning mechanisms behind the results observed from the experimental measurements shown in the following chapters.

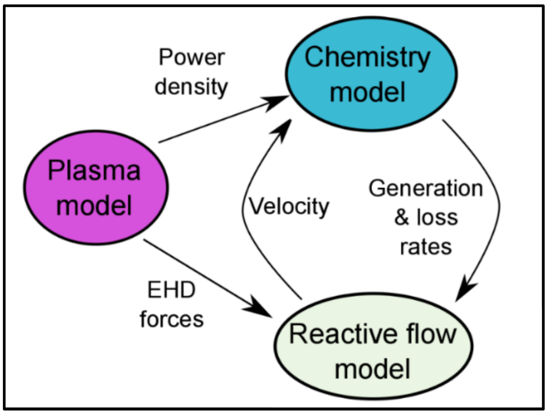

Figure 22: Diagram showing the coupling between different modules within the computational model.

The main computational model used in throughout this contribution was a 2D time-dependent model, comprising of a number interconnecting sub-models that each computed the variables necessary for the main model. While the investigation detailed in chapter 4 only required the plasma sub-model solving. Figure 22 indicates how the plasma module and the chemistry module were coupled with the reactive flow model. The plasma model linked experimental parameters, such as the electrode geometry, applied voltage waveform, and dielectric thickness to variables needed by the reactive flow model, these variables were the EHD force field and the plasma power density. The plasma model was a fluid model that solves a system of conservation equations for the densities of electrons, electrons energy, $N_2^+,\ O_2^+, O_2^-, O, and\ O_3$ in addition to the background $O_2\ and\ N_2$. The model solves the Poisson equation for the electric potential and the surface charge continuity equation on the dielectric surface, shown as the interface between the air domain and the dielectric domain of each SBD setup. All of the simulation parameters were chosen to exactly match those in the corresponding experiments. The reasoning behind this adopted approach was to use the plasma sub-model to accurately capture the physics of the discharge while the chemistry of the discharge was accurately modelled using the chemistry sub-model. Further details of the model can be found in appendix A.

Chapter 4: Impact of electrode geometry on atmospheric pressure SBD's

Edited edition of: M. I. Hasan, Y. Morabit, A. Dickenson & J. L. Walsh. 'Impact of electrode geometry on an atmospheric pressure surface barrier discharge', Applied Physics Letters, 110, 264101 (2017).

The geometrical configuration of electrodes in an atmospheric pressure SBD configuration has an impact on several key physicochemical characteristics of the plasma. In this chapter it is shown that changes in the diameter of circular discharge gaps can heavily affected the discharge properties. Experimental findings show that a critical limit exists beyond which reducing the diameter of a circular electrode gap below 5 mm, results in the required breakdown voltage to increase exponentially and the power deposited in the discharge to be impeded. To understand the underpinning physical mechanisms behind the experimental observations a numerical model was employed. The model showed that a reduction in the electrode gap diameter yielded a decrease in the voltage difference between the electrode and dielectric surface in the plasma domain, thus lowering the maximum electric field. Particle imaging velocimetry was also used to assess the impact on the EHD induced flow for gap diameters >5mm. The flow velocity was found to increase with diameter, which was deemed to be as a result of an increase in streamer density thus resulting in greater charge deposition in the discharge. These observations indicate a link between the geometry of the electrodes in an SBD and the nature of the reactive chemistry in the plasma, thus for applications where multiple closely packed SBD's are employed to achieve uniform and large area plasmas, some previously unforeseen implications have been demonstrated.

4.1 Introduction

Considering that many applications of the SBD, such as ozone generation, flow actuation, microbial decontamination and high-value materials processing, often require a large area discharge with good uniformity, many researchers have considered placing multiple SBD’s in close proximity to form an array. Many reports in the literature have focused on arrays of SBD’s and many researchers have demonstrated the ability to generate large area and uniform discharge using linear, circular or hexagonal electrode geometries [45], [68], [92]. These SBD arrays are usually composed of many small discharges packed closely together, as a means of generating larger plasma volumes over the surface of the discharge domain with a high degree of uniformity. Such configurations are ideal when the uniform processing of a downstream surface is essential. While increasing the number of SBD’s on a surface has proven to be effective, changing the electrode geometry can greatly influence the underpinning physical processes which remains a relatively unexplored area.

One of the key physical processes that can be influenced by electrode configuration is the breakdown voltage, this is defined as the amplitude at which the energising waveform applied to the driven electrode is sufficiently high enough to cause a discharge to occur, in the case of an SBD this in the form of stochastic filamentary discharges [52], [143]. Changes in breakdown voltage would inherently affect the power input to achieve specific densities of species and in applications where RNS chemistries are necessary the ability to access these regimes can be impacted.

Breakdown in SBDs can be observed experimentally as intense current spikes visible on the displacement current of the energising waveform where each spike represents one or more individual discharge events. Determining the exact point at which breakdown occurs experimentally is not as straightforward as one would expect; however, a procedure was established for determining the point of breakdown by examining the current spikes in this contribution.

This chapter explores the impact of reducing the diameter of the electrode discharge gap on the underpinning physical processes in a circular SBD configuration. Measurements of the breakdown voltage and power densities were experimentally performed. A numerical model was implemented as a means to capture the underpinning physical mechanisms involved. Through the use of particle imaging velocimetry, the electrohydrodynamic EHD induced flow was analysed, thus giving an insight into the impact of electrode geometry on the mass transport of reactive oxygen and nitrogen species downstream of the discharge, which can be crucial in an application context.

4.2 Experimental Methodology

4.2.1 Setup of surface barrier discharge

A schematic of the surface barrier discharge used in this investigation is presented in figure 23. Ten individual double-sided 1.6 mm thick copper clad FR4 boards were used, each measuring 50 x 50 mm square. Circular discharge gaps ranging in diameter from 1 to 10 mm were machined out of centre of one of the sides of each board which acted as the driven electrode while the other side was left untouched and set as the ground.

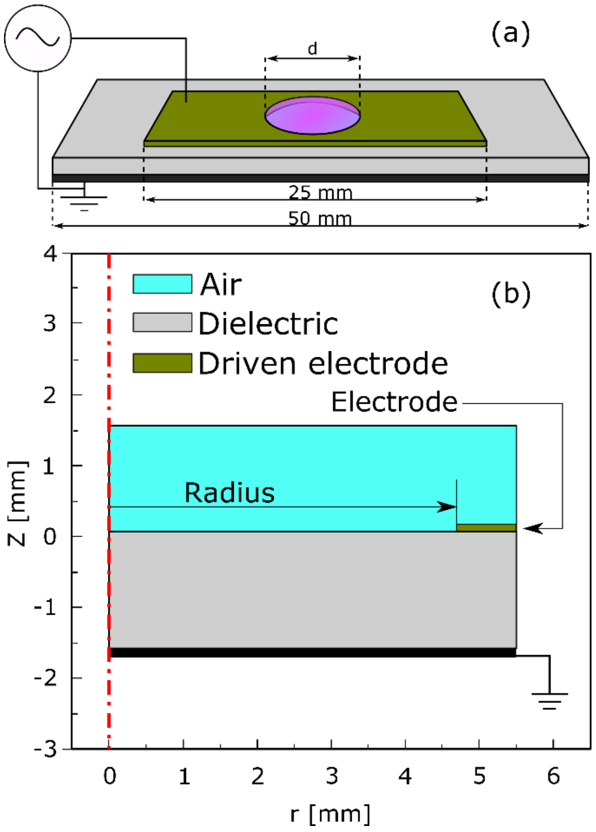

Figure 23: (a) Illustration of SBD used in investigation; d is the diameter of the discharge gap. (b) Schematic showing the axisymmetric computational domain; red dashed line denotes the axis of symmetry.

All electrode edges were sealed using silicone as to prevent any undesired discharges apart from those that take place in the discharge gap identified in. As to confirm that no other discharges took place other than those in the discharge gap optical imaging was used. The HV drive signal was generated by a homemade sinusoidal power supply at a frequency of 15 kHz.

4.2.2 Experimental breakdown measurement

The procedure used to determine the breakdown voltage was based on monitoring the discharge current. Using an oscilloscope (Tektronix 5054, 500 MHz, 5 GS/s) operating in single shot mode, a trigger was placed just above the peak of the displacement current signal recorded via a current probe (Pearson 4100, 1 V/A, 50 Ω). The voltage supplied to the driven electrode was then gradually increased at a rate of approximately 50 Vs^{-1} until activation of the trigger was achieved due to the first current spike, indicating breakdown voltage has been reached as at least one filament had been produced. Within an SBD such filaments take the form of short and intense spikes occurring on time scales ranging from 10 to 100 ns; each current spike represents at least one discharge event and usually has a magnitude several times larger than the underlying sinusoidal displacement current, as shown in figure 24.

The voltage was measured at the driven electrode using a high voltage probe (Tektronics P6015A, 75 MHz, 20 kV, 1000:1) when the single shot measurement was triggered was then recorded as the breakdown voltage. This procedure was repeated six times for each SBD configuration and an average value was calculated to provide statistical robustness.

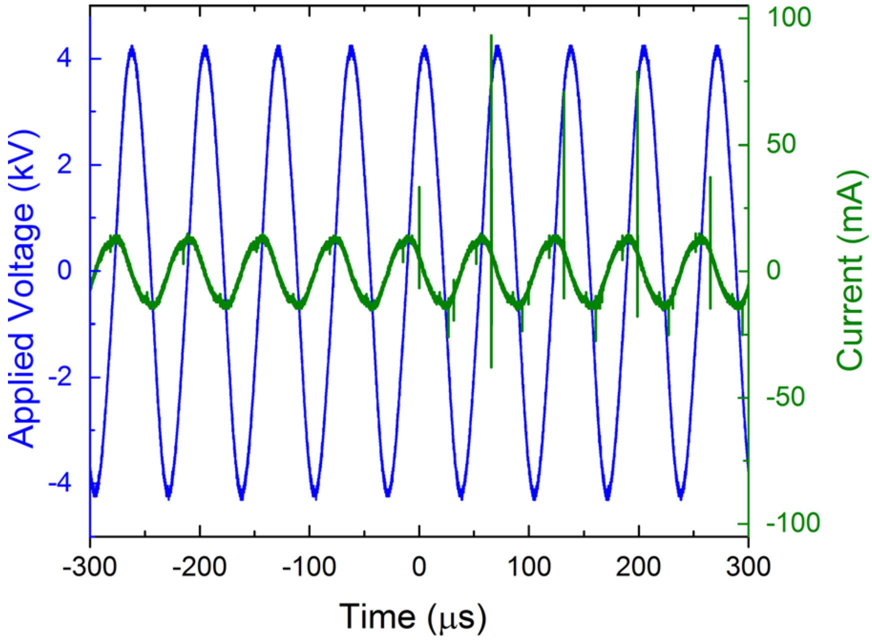

Figure 24: Applied voltage & current waveforms at the breakdown voltage for a discharge gap diameter of 4 mm.

4.2.3 PIV setup

Particle imaging velocimetry enabled time averaged measurements of the flow field created by the EHD induced flow to be obtained, for the SBD operating at an applied peak-to-peak voltage of 7 KV. The procedure used mirrored that detailed in chapter 3 (section 3.1).

4.2.4 Numerical model implementation

Only the plasma sub-model (discussed in section 3.4) required solving in both parts of the computational domain shown in figure 23, in order to make a comparison to the experimental results and determine the underpinning mechanisms involved. A spike in the power deposited in the discharge was used to characterise the breakdown event in the numerical model. Ohmic heating, $J.E$, (where J is the current density & E the electric field) was used to define the deposited power in the computational domain. This was integrated in the air domain and plotted as a function of time.

Similar to the experimental procedure used in determining the breakdown voltage V_B, for the model the simulation was run multiple times with the applied voltage systematically increased each time. For applied voltages < V_B, no power spikes were detected at any point in the applied waveform. Once a power spike was observed, the voltage magnitude used to generate it was assumed to be the V_B. Each discharge gap diameter was investigated using this procedure. To explain the observed trends in breakdown, the numerical model was run using a constant applied voltage for each discharge gap diameter in the absence of a plasma discharge. This was done to focus on the geometrical effects involved without influence from any plasma effects. As such an assumption mimics the discharge conditions before the breakdown voltage is met, thus only the Laplace equation requires solving.

4.3 Results and discussion

4.3.1 Impact on breakdown

The influence of the variation in discharge gap diameter from 1 to 10 mm on the breakdown voltage is presented in figure 25. For discharge gaps ≥5 mm a signal of ~3.5 KV amplitude applied to the driven electrode was sufficiently high enough to initiate breakdown. The minor variations observed in the breakdown voltages for discharge gaps of ≥5 mm diameters are considered to be a result of surface imperfections on the electrode edge arising from the machining process.

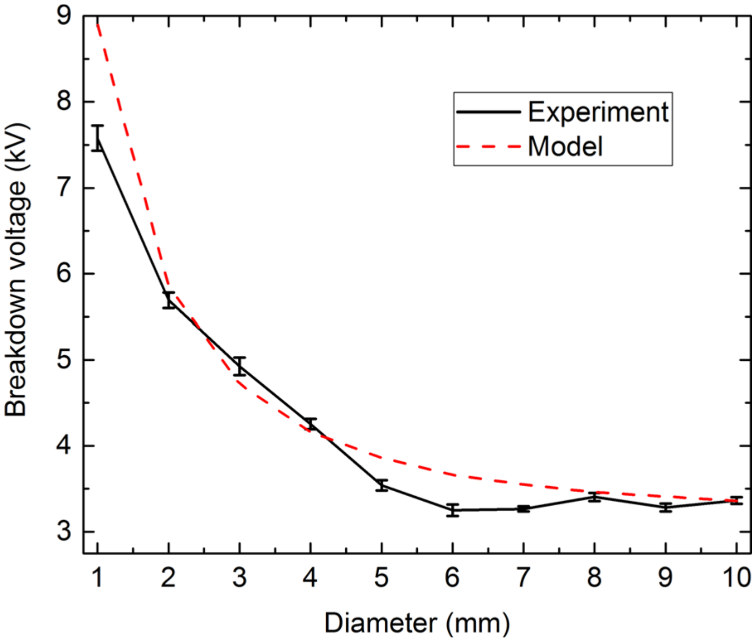

Figure 25: Experimental and numerical data of breakdown voltage as a function of discharge gap diameter.

A rapid increase in the breakdown voltage is seen to occur when the diameter of the discharge gap was reduced below 5 mm. This is despite the inter-electrode distance (*i.e.* the distance between the driven and grounded electrodes) which remains constant as it is determined by the thickness of the dielectric material.

These experimental measurements fit well with those predicted by the numerical model which displays the same trend of increasing breakdown voltage with reduced discharge gap diameter, also shown on figure 25.

4.3.2 Impact on deposited power

The impact of discharge gap diameter on power deposition was also investigated to identify any effects that could compromise the composition or density of the generated reactive species as a result of variations in discharge gap diameter. For discharge gap diameters of 4, 6, 8 and 10 mm the deposited powers were calculated experimentally and via the plasma model. To ensure that breakdown occurs in all cases a constant peak applied potential of 7 kV was chosen. The power deposited in the computational domain was integrated in the air domain then averaged in time over the duration of a single cycle of an assumed applied drive signal at 15 kHz, matching that used in the experimental investigations, and then normalised by the surface area of the discharge gap for each gap diameter.

Table 6 shows the calculated deposited power density as a function of the gap diameter which closely matches those from experimental measurements. There is a clear trend of decreasing power deposition when reducing the discharge gap diameter at any given voltage.

Table 6: Calculate deposited power density at a constant applied voltage of 7 kV as a function of electrode diameter.

Diameter (mm)	**Power density (W cm^{-2})**
10	0.2
8	0.16
6	0.11
4	0.1

It is well documented that SBD's operating under high dissipated power conditions (>0.2W cm^{-2}) favour the production of reactive nitrogen species (RNS), *e.g.* NO, N_2O and NO_2 [52]. Given that such chemistries are known to be highly effective for several healthcare related applications including biofilm decontamination and wound healing [104], [144], any factor that impacts the power deposition in the discharge requires careful consideration. Thus, it is extremely disadvantageous to reduce the discharge gap diameter if RNS dominated regimes are required as it becomes increasingly difficult to access these chemistries due to the reduction in power deposition with decreasing discharge gap diameters as demonstrated.

4.3.3 Potential difference across discharge gap

The results obtained using the assumptions made in the numerical model to determine the geometrical effects in the absence of plasma for each electrode configuration is shown in figure 26. A decrease in the potential drop in the gap is observed with a reduction in the diameter of the discharge gap.

For discharge gaps larger than 5 mm, the data in figure 26 implies that the potential at the center of the gap is essentially independent of the applied voltage at the driven electrode.

Regardless of the discharge gap diameter, the potential difference across the gap (*i.e* from its centre to the electrode edge) remains constant, thus V_B will also remain constant.

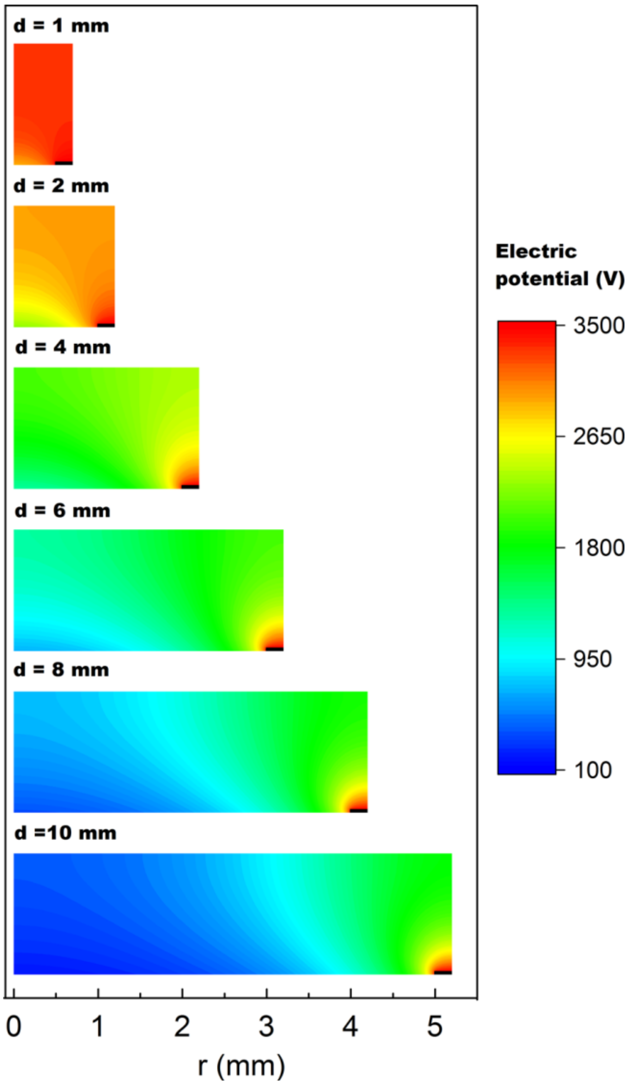

Figure 26: Electric potential for various gap diameters at a constant applied voltage of 3.5 KV. Electrodes shown as black boxes.

When the diameter of the discharge gap is reduced below 5 mm, the potential applied to the driven electrode causes an elevation of the potential across the whole gap. This phenomenon results in a reduction of the potential difference across the discharge gap, weakening the electric field at any given applied voltage, thus V_B is increased.

4.3.4 Impact on EHD induced flow

The impact of discharge gap diameter on the electrohydrodynamic forces was also investigated using PIV measurements of the velocity flow fields induced by the plasma discharge. To assess the impact of gap diameter on species transport the flow velocity from gap diameters of 6, 8 and 10 mm at a constant applied voltage of 7KV was measured. The results of these measurements are shown in figure 27.

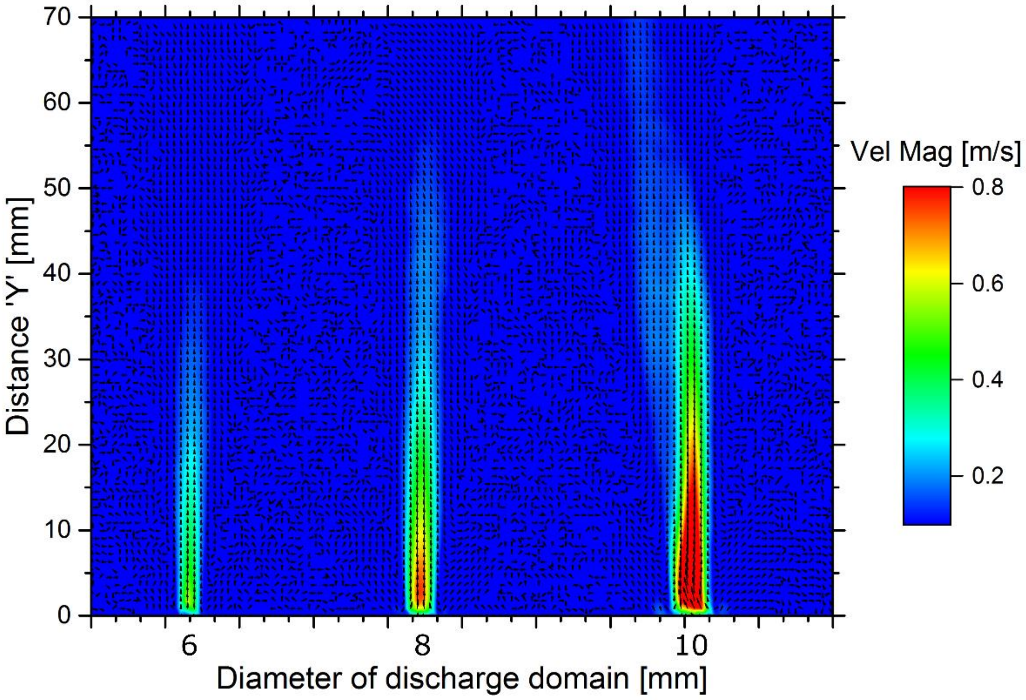

Figure 27: velocity flow plots for circular electrode geometries of 6, 8 & 10 mm diameters, driven by a constant 7 kV signal.

From the figure it is clear to see that increasing the gap diameter yields an increase in the velocity magnitude of the EHD induced flow near the surface of the dielectric and downstream of the discharge gap. In the 6 mm case the maximum velocity achieved was ~0.4

ms^{-1} while for a discharge gap of 10 mm in diameter the maximum velocity of the induced flow is ~0.8 ms^{-1}.

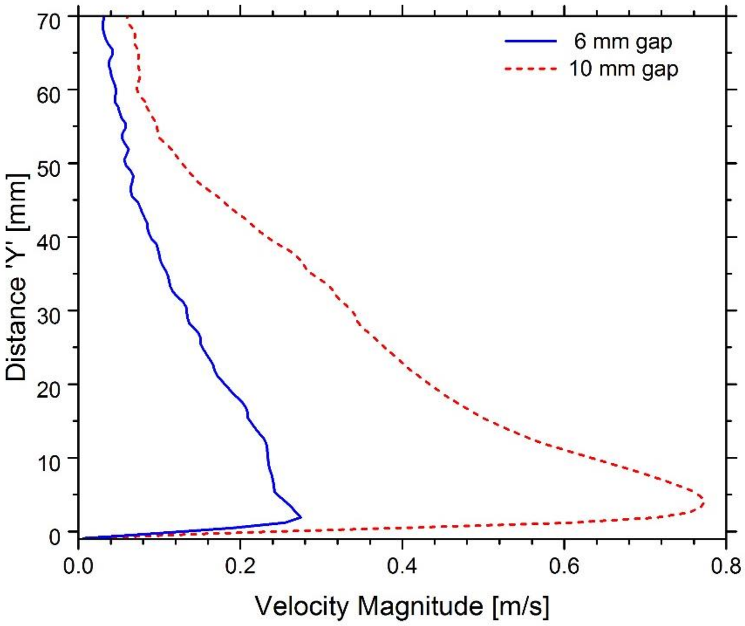

Figure 28: Centreline velocity profiles for 6 & 10 mm diameter discharge gaps.

Velocity profiles were taken perpendicular to the dielectric surface from the center of the discharge gap as seen in figure 27. The magnitude of the flow velocity for the 10 mm diameter discharge gap is shown to reach a much higher value of ~0.75 m/s compared to that off the 6 mm gap, which reaches a magnitude of ~0.25 m/s, despite both discharges being operated at a constant applied voltage.

Given that the breakdown voltage increases rapidly for diameters <5 mm, the EHD induced flow would inherently be affected. A decrease in the deposited power density in the discharge and a reduction in the electric field potential across the discharge gap, will result in less charged particles due to weaker ionisation, that acquire less energy from the electric field thus impeding the magnitude of the plasma induced flow as indicated in a number of investigations referenced in chapter 2. The velocity increase in the induced flow was regarded as a direct result of an increase in streamer formation and thus charge deposition to occur, as shown in table 6. This results in an increased flux of charged species moving to and from the dielectric surface in the discharge gap thus increasing the EHD forces and inducing a stronger flow. [65]

4.4 Conclusions

In this chapter, the importance of the geometrical configuration of the electrodes in a SBD has been highlighted. It was shown that the electrode geometry can have a significant impact on several key plasma parameters, including the breakdown voltage and deposited power in the discharge, which are strongly affected by a reductions in the discharge gap diameter below a critical value. The critical value in this experiment was found to be 5 mm, which was the diameter of a circular discharge gap fabricated on FR4 dielectric sheets. For discharge gap diameters below 5mm the breakdown voltage was observed to increase rapidly and the power deposited within the discharge was reduced compared to that of the larger diameter gaps.

The underpinning mechanisms behind these observations were found to be a result of the potential in the circular discharge gap becoming increasingly uniform as the diameter is reduced. This leads to a reduction in the potential difference across the discharge gap and an increase in the required breakdown voltage due to the diminished electric field at any given voltage. As the deposited power can directly influence the generation of reactive species in a non-thermal discharge, the findings presented in this chapter have significant implications for the development of large area and uniform SBD arrays. A compromise between the discharge area of the individual SBD’s and the applied voltage required to achieve a desired discharge chemistry must be made.

The chapter also highlighted that the EHD forces created by the plasma are also directly affected by electrode geometry. A decrease in the velocity magnitude was shown to occur with a reduction in gap diameter, this is as result of the weakened electric field at any given point across the discharge gap which results in a reduction to the transfer of momentum through collisions of charged particles with heavy neutral particles. As the mass transport of plasma generated species heavily relies on this flow, as discussed in chapter 6, it is an import aspect to consider when designing SBDs for applications where shorter lived reactive species are required. Although the results in this chapter have been obtained from an SBD with a circular gap geometry, it is highly likely that the underpinning physical mechanisms involved apply to all SBD systems, including those employing other electrode geometries, as well as other widely used gases such as oxygen, carbon dioxide, argon and helium.

Chapter 5: Tailored generation of RONS through temperature & flow manipulation

This chapter explores the effect of dielectric surface temperature on the composition of the reactive chemistry generated by an atmospheric surface barrier discharge, via a custom-built temperature controlled system. It is well known that increasing both the gas temperature and/or power deposition can initiate a transition from an ROS rich regime to a RNS dominated regime. This chapter hypothesises that controlling the dielectric temperature could provide a means to control species composition at a constant plasma power. Using a thermoelectric element, the temperature of the dielectric in an SBD was varied from 20 to 100 ^{o}C; enable the ROS/RNS transition to be attained under constant plasma power conditions, the first report of such a phenomenon. The underpinning mechanisms behind the ROS/RNS transition was considered to be related to NOx production. The effect of increasing the flow rate of air into the reactor was also analysed under controlled temperature and dissipated plasma conditions. It was found that an increase in the flow rate could delay poisoning and/or essentially negate ozone poisoning entirely. These findings demonstrate how the species generated from a surface barrier discharge can be tailored for the particular needs of an application.

5.1 Introduction

Depending on the operating conditions of an SBD different reactive chemistries can be accessed. It has already been well established that increasing the power deposited in the plasma discharge can have an adverse effect on the production of reactive species such as ozone. [4], [145] The underpinning mechanisms behind the transition into an "ozone-poisoning" mode are still a matter for intense debate.

Certain reactive species generated by a plasma discharge, can cause specific chemical reactions that are beneficial to a number of industrial applications. [28], [146], [147] Ozone & Hydroxyl have been widely used in the decontamination of microorganisms due to their potent oxidising properties. [92], [93], [148] While NO has proven to aid wound healing by the stimulation and proliferation of wound related skin cells. [29], [44], [149] Other nitrogen species such as N_2O have catalytic and nitration properties that are not only beneficial within healthcare application but can also be beneficial within the food and agriculture sectors. [150], [151]

Due to the scalability of SBDs and the tantalising possibility to tailor the composition of generated reactive species they have attracted a vast amount of interest in the research community. In this chapter the effect of altering the operating conditions and surface temperature of the dielectric material in an SBD was investigated. FTIR was used to analyse the gas phase species produced at different deposited powers, input air feed flow rates, and temperatures ranging from 20-100 ^{o}C.

The impact of dielectric temperature under different operating conditions was explored in an effort to uncover a viable method to control the composition of the longer-lived afterglow chemistries generated from the SBD. Using gas phase analysis, the possible underpinning mechanisms involved in the transition from a ROS to RNS regime are discussed.

5.2 Experimental Methodology

5.2.1 Controlled low-temperature plasma source

A schematic of the SBD used in this investigation is presented in figure 29. To achieve a degree of temperature control over the dielectric surface, one side of a Peltier element was adhered to the grounded side of the SBD using a thermal epoxy (with high thermal conductivity). The SBD was constructed using a 50 mm^2 alumina sheet of thickness 1 mm, with copper electrodes attached either side. Plasma formed on the powered electrode outer edges as seen in figure 29, while the epoxy adhesive restricted the formation of plasma on the grounded electrode edges. 35 µm thick copper film was used for both electrodes.

A high-voltage sinusoidal waveform was used to drive the powered electrode at a frequency of 25 kHz which was generated from a custom-made power supply. The effect of temperature at different discharge powers was investigated. Voltage and current measurements of the high-voltage signal were respectively made using a Tektronix P6015A high voltage probe and Pearson 2877 current monitor. Both waveforms were recorded using a Tektronix DPO 5054 oscilloscope which enabled the dissipated power within the discharge to be calculated via multiplication of the applied voltage and discharge current waveforms.

Heating or cooling of the dielectric surface from 20 to 90 ^{o}C was achieved by application of a DC (+/-) voltage to the Peltier element using a benchtop power supply. The temperature was recorded via a thermocouple attached to the plasma forming side of the dielectric. In order to confirm the temperature recorded by the thermocouple wasn’t being affected by the high voltage signal applied to the powered electrode an infra-red camera was also used to measure the dielectric temperature over the range of experimental conditions investigated.

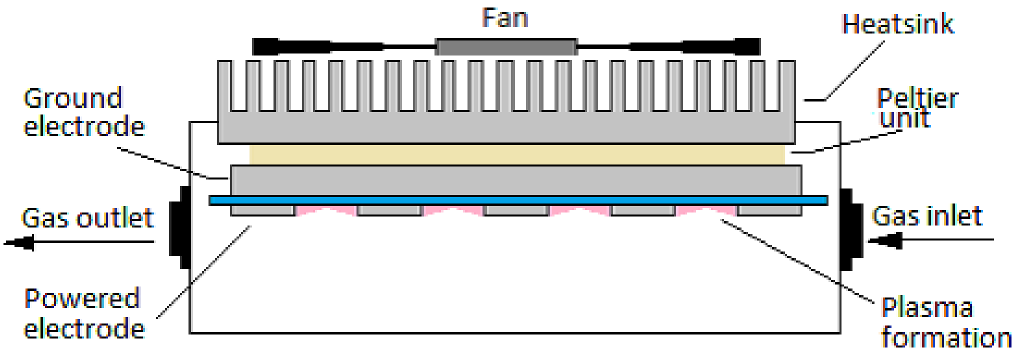

Figure 29: Schematic of the temperature controlled surface barrier discharge device confined in an enclosure.

5.2.2 Gas phase species quantification

Measurements of the gaseous phase species were conducted using FTIR spectroscopy in conjunction with ozone monitoring, as detailed in the methodology chapter (section 3.2.1). All FTIR measurements were taken for a constant dissipated plasma power of 1.33 W cm^{-2} and air feed flow rate of 1 LPM. Two separate measurement techniques were used in the investigation, first a constant dielectric temperature of 90 °C was set and spectral acquisitions were taken every 30 seconds after plasma ignition for a total period of 2 minutes, as seen in section 5.3.4. Then finally the spectral acquisition was taken every 15 second for a total period of 30 minutes while the temperature was changed every 5 minutes, as seen in section 5.3.5.

5.3 Results and discussion

5.3.1 Steady state temperature analysis

Using discharge powers of 5, 10 and 15 W, the temperature of the dielectric material was seen to rise from ~20 ^{o}C at plasma ignition to reach a steady state value over a 60 second period without any influence from the Peltier. The correlation between dissipated discharge power and dielectric surface temperature can be seen in figure 30. This temperature was considered the steady state temperature of the plasma system at each of the dissipated powers under investigation. It is clear to see that a trend exists, with increasing plasma power dissipation leading to a higher dielectric temperature.

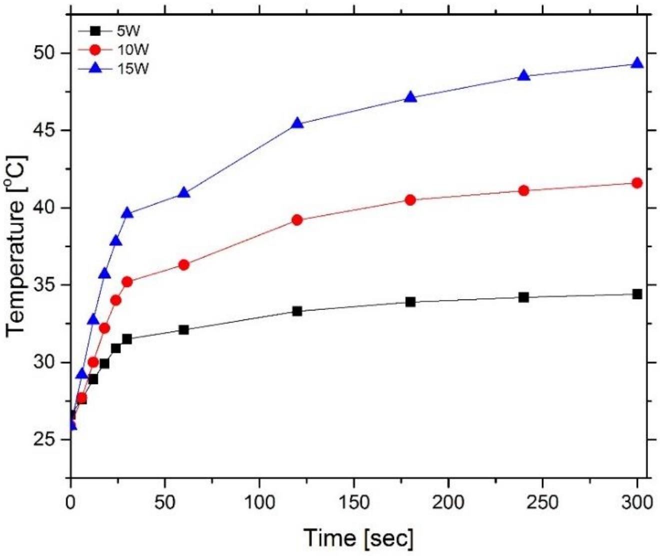

Figure 30: Steady state dielectric temperature for different dissipated powers.

5.3.2 Impact of dielectric temperature on ozone production

The evolution of ozone production over time was performed for different dielectric temperature and plasma power settings, seen in figure 31. This data was collected by preheating the dielectric prior to ignition of the discharge at each of the investigated power setting. From the figure it is clear that increasing the temperature results in a reduction in the initial rate of ozone production, as well as the final steady state ozone concentration for each power measurement. The highest concentration of ozone was produced at a temperature of 30 °C in all discharge power cases. Dissipated powers >0.57 W cm^{-2} resulted in an increase in ozone concentration at 30 °C, while further increases in the power >0.95 W cm^{-2} resulted in no further advances in the total ozone produced.

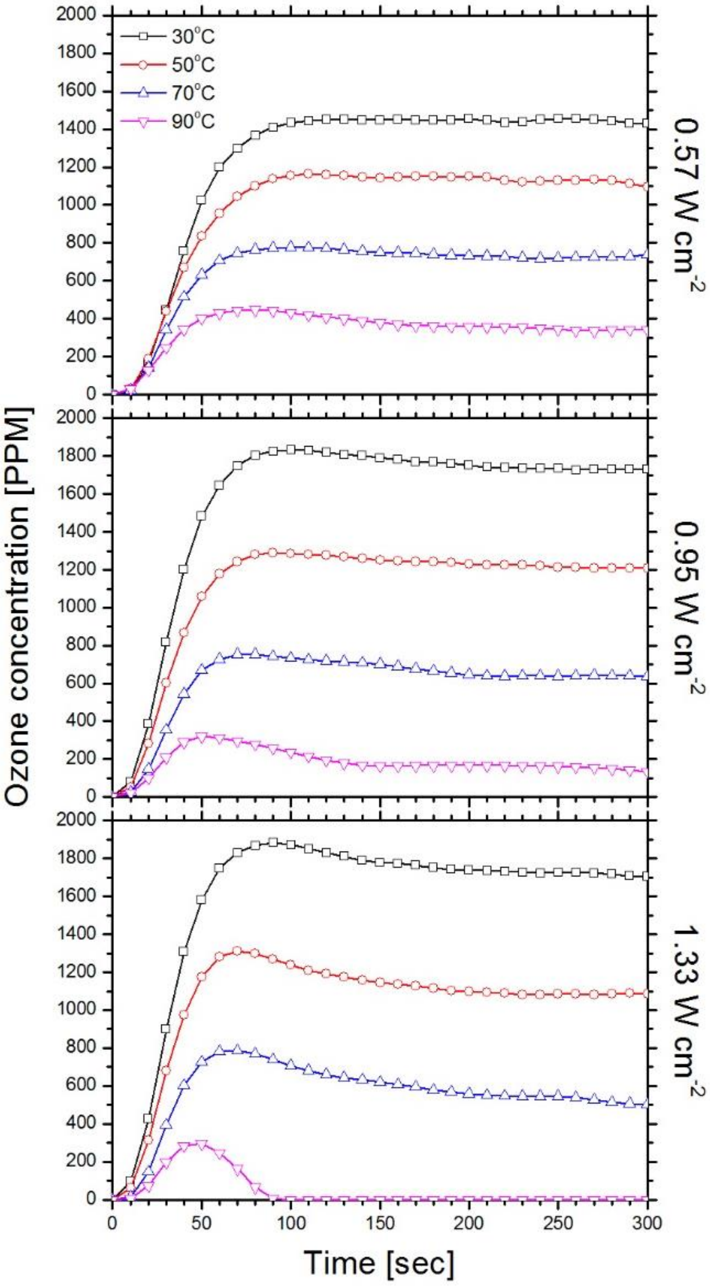

Figure 31: Temporal evolution of ozone concentration for an air feed of 1 LPM at variable dissipated powers of 0.57, 0.95 & 1.33 W cm^{-2}. Temperatures ranging from 30-90°C.

The reduction in final steady state ozone concentration observed with increasing temperature may be due to its thermal decomposition. [152] At the highest power density setting of 1.33 W cm^{-2}, a decreasing trend is seen after the initial peak concentration of ozone for each temperature measured. In the case of 90 °C ozone production is entirely inhibited (poisoned) after just 100 seconds. The threshold at which ozone starts to reduce with time is considered as a result of reactive NO_x being generated in the discharge that causes ozone to be quenched, which will be discussed in more detail in the following sections.

5.3.3 Impact of flowrate on species generation

Taking the 1.33 W cm^{-2} case where ozone is poisoned at 90 °C, the effect of increasing the airflow into the system was analysed, as seen in figure 32. Increasing the rate at which air is supplied to the plasma chamber from 0.5-1.5 LPM results in an increase in peak ozone concentration from 225 to 300 PPM along with a delay in the time taken for ozone to be fully poisoned (~50 second delay).

For the 2 LPM case ozone poisoning can be entirely prevented within the 5 minute measurement period. A peak ozone density of ~425 PPM was achieved with a final ozone concentration of ~225 PPM after 5 minutes. These findings demonstrate that a viable means of delaying the process of ozone quenching is possible by controlling the rate at which air is fed into the plasma chamber, thus enabling the manipulation of longer-lived species generation species generation. Intuitively the steady state temperature of the dielectric, seen in figure 30 would also be affected by the air feed flow rate, as an increase in air flow would have an increased cooling effect. However, in this scenario the Peltier system is operated at a higher power to maintain the temperature at a constant 90 °C.

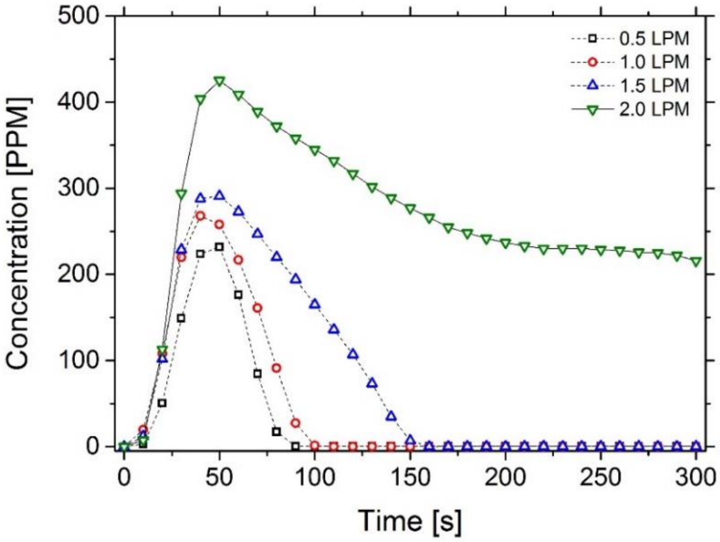

Figure 32: Temporal evolution of ozone concentration at a dissipated power of 1.33 W cm^{-2} and a constant temperature of 90^{o}C .For input air flowrate of 0.5, 1, 1.5 & 2 LPM.

5.3.4 Temporal evolution of absorption spectra

The spectral acquisitions taken every 30 seconds after plasma ignition indicate how the long-lived species transitions from ROS dominated to RNS dominated over time, as seen in figure 33. The intensity of the ozone absorption peak at ~1000 cm^{-1} can be seen to follow the measurements shown in the previous sections. Once ozone is poisoned, NO_2 starts to form and drastically increases in concentration, observed as absorption peak at ~1600 cm^{-1}. Along with reduction in absorption peaks at ~ 700 cm^{-1}, 1100 cm^{-1} and 1700 cm^{-1} which is indicative of N_2O_5 density..

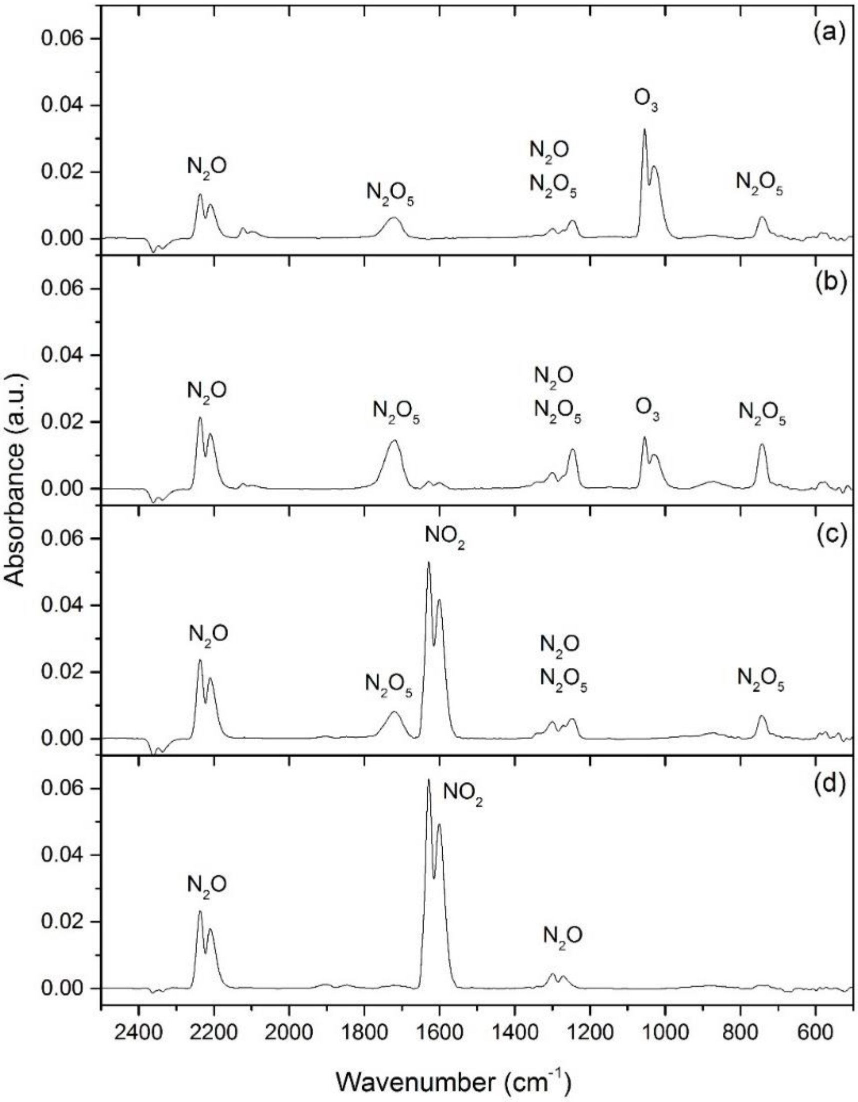

Figure 33: FTIR spectral measurements for a constant dissipated power of 1.33 cm^{-2}, temperate of 90 ° C and an input air flowrate of 1 LPM. (a) 30, (b) 60, (c) 90, (d) 120 seconds after plasma ignition.

5.3.5 Quantification of key RONS

The concentrations of three 'key' species O_3, NO_2 & N_2O, were calculated from their corresponding absorption peaks (at 1000, 1600 & 2200 cm^{-1} respectively) obtained via FTIR measurements. The results are illustrated in figure 34.

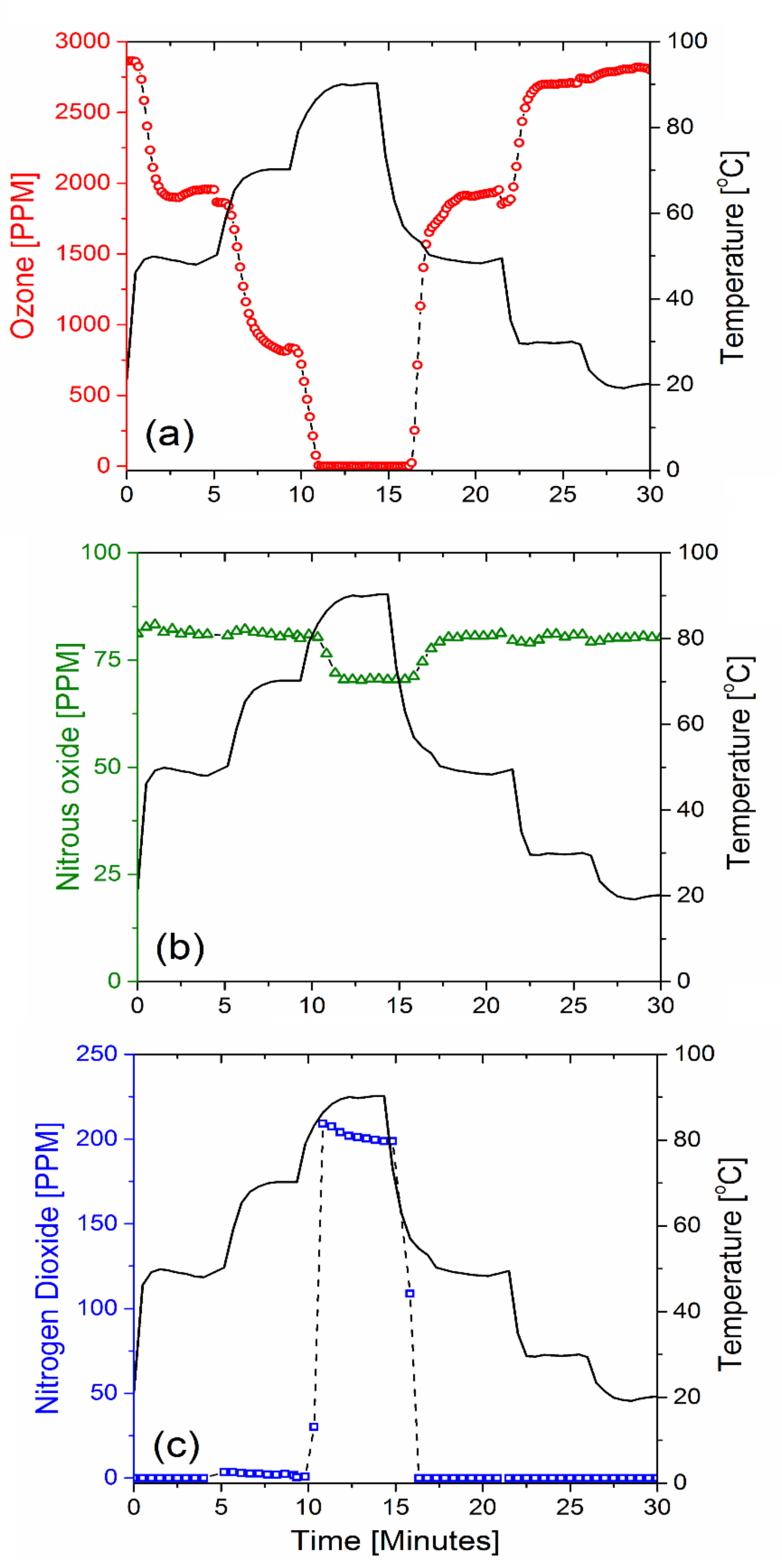

Figure 34: Concentrations of three key long lived species (a) Ozone, (b) Nitrous oxide & (c) Nitrogen dioxide at a constant dissipated power of 1.33 W cm^{-2} with corresponding electrode temperature shown in black.

Clearly, the ozone concentration is shown to follow the trend given in previous sections. As temperature increases the concentration of ozone systematically drops from its starting density of ~2800 PPM until total inhibition in ozone production is achieved at 90 °C. Reducing the temperature enables the mechanisms of ozone generation to dominate once again, thus we see the inverse effects in the concentration of ozone which increases back to its initial value, when the temperature is reverted back to its starting temperature (20 °C). At 90° there is also a distinct change in the production of the other key species. A reduction of ~20 PPM is seen in the total concentration of N_2O, once ozone is fully poisoned. This is followed by the initiation of NO_2 production which rises from 0 PPM to concentration of ~200 PPM.

5.3.6 Underpinning mechanisms

From a review of the literature, the underpinning mechanisms involved in ozone poisoning are considered to be directly related to a set of key chemical reactions that can occur. One of the dominant reaction pathway for the generation of ozone is given in R1. Ozone is generated in the discharge, from reactions between atomic oxygen and oxygen in the plasma domain [153].

$$O + O_2 + M \rightarrow O_3 + M \tag{R1}$$

Once ozone poisoning is observed, the inhibition of N_2O_5 production occurs as seen by the declining absorption peak down to 0 a.u. at ~1300 cm^{-1} in figure 33. The chemical pathways that lead to N_2O_5 are given by R2-R4 [154], [155]. This reaction pathway can explain why we see this inhibition in N_2O_5 peak, as it relies on the presence of O_3 in its production. [155]

$$NO + O_3 \rightarrow NO_2 + O_2 \tag{R2}$$

$$NO_2 + O_3 \rightarrow NO_3 + O_2 \tag{R3}$$

$$NO_2 + NO_3 \rightarrow N_2O_5 \tag{R4}$$

The set of reactions for N_2O_5 production may also explain the absence of NO_2 until the RNS regime is attained, as NO_2 reacts with O_3 (R3) at a high rate [155]. R2 & R3 present ways in which ozone can be quenched and may go some way uncovering the ozone poisoning phenomenon. The sudden increase in NO_2 seen in figure 34 following ozone depletion is considered to be through an increase in the rate of NO_2 formation by R2 & R5 that surpasses that of the rate of NO_2 reaction with O_3, seen in R3.

$$O + NO + M \rightarrow NO_2 + M \qquad \text{(R5)}$$

Other reactions taking place that contribute to the active destruction of ozone, include reactions with dissociated oxygen (O) and nitrogen (N) molecules in air:

$$O + O_3 \rightarrow 2O_2 \qquad \text{(R6)}$$

$$N + O_3 \rightarrow NO + O_2 \qquad \text{(R7)}$$

Reactions between O_3 and NO_x species are considered to be the main driving mechanism behind the destruction of ozone.

There are a number of possible reactions that can take place to form NO. It is well known that NO is a major quencher of O_3, given by R2. Some of the reactions involved in NO formation are presented in R8-R9. [156], [157]

$$O(1D) + N_2O \rightarrow 2NO \qquad \text{(R8)}$$

$$O + NO_2 \rightarrow NO + O_2 \qquad \text{(R9)}$$

$$N + O_2 \rightarrow NO + O \tag{R10}$$

In the case of N_2O, there is a slight reduction in its total concentration once ozone poisoning occurs. This phenomenon may be explained through its formation, R11. Given that N_2O is formed through reactions involving excited N_2 states and oxygen molecules, then once ozone is depleted the concentration of oxygen molecules is also reduced as seen by R2 & R3.

$$N_2^* + O_2 \rightarrow N_2O + O \tag{R11}$$

A more comprehensive list of possible reactions that can occur in the gas phase chemistry of a SBD are shown in appendix A&B. These were used in the chemistry sub-models in the investigations discussed ahead (chapter 6 & 7).

5.4 Conclusions

The density of long-lived reactive oxygen and nitrogen species generated by a surface barrier discharge in an enclosed environment, was shown to be heavily dependent on a number of key factors. Increasing the plasma dissipated power resulted in a higher concentration of ozone production up to a certain limitation, at which point the density was seen to drop over time. The findings show that there are inherent limitations in the maximum achievable ozone densities produced from a surface barrier discharge. Manipulation of the dielectric temperature was shown to enable a degree of control over the transition between ROS and RNS chemistries, allowing for specific concentrations of species to be generated up to certain thresholds set by the dissipated power into the discharge and limitations of the device itself.

The underpinning mechanisms involved in the so called “ozone-poisoning” mode were regarded to be as a result of catalytic reactions taking place with reactive NO_x species. One species that is considered to have a significant influence on the transition into this mode is NO, due to its high reactivity with ozone. It was discovered that ozone poisoning could be delayed or essentially negated through an increased flow rate of the air feed supplied to the plasma enclosure. Thus, control over the flow rate of the feed gas, plasma dissipated power and/or temperature of the dielectric insulator present viable methods of tailoring the densities of longer-lived species in the afterglow of a surface barrier discharge. These points present SBDs as promising tools in applications were both long lived nitrogen and oxygen species are required independently, as these findings show viable methods of easily accessing these regimes through simple techniques.

Chapter 6: Downstream transport of reactive species from a surface barrier discharge

The work detailed in this chapter was reported in: A. Dickenson, N. Britun, A. Nikiforov, C. Leys, M. I. Hasan & J. L. Walsh. 'The generation and transport of reactive nitrogen species from a low temperature atmospheric pressure air plasma source' *Physical Chemistry Chemical Physics*, 20, 45 (2018).

Understanding the underpinning mechanisms involved in the generation and transportation of reactive oxygen and nitrogen species from an SBD has been the focus of many previous studies but the mechanisms are still far from being fully understood. This chapter focuses on an investigation of the spatiotemporal behaviour of key reactive nitrogen species N, NO, NO_2, N_2O, generated downstream of an atmospheric pressure air surface barrier discharge using both laser induced fluorescence and particle imaging velocimetry combined with experimentally validated numerical modelling. All reactive species investigated were observed to closely follow the EHD induced flow apart from atomic Nitrogen which is confined to the active discharge region due to its high reactivity. Up to 25 mm downstream of the discharge the concentration of key RNS was found to be in the range of 10-100 ppm and the experimental results display a close agreement with the numerical model. The findings from this investigation provide a valuable insight into the role of the EHD forces in dictating the spatiotemporal distribution of reactive species beyond the plasma generation region.

6.1 Introduction

When selecting a particular plasma system for a given application, two key requirements must be met: (1) the operating conditions must favour the generation of reactive species that are of particular importance for the intended application, e.g. Nitric oxide to aid wound healing or Hydroxyl for its bactericidal properties towards pathogen decontamination; [44], [148], [158], [159] and (2) the uniformity of the plasma source must be sufficient to provide an even dose of reactive species over a characteristic surface area on a downstream target.

Several previous studies have focused on the generation of reactive chemical species from atmospheric pressure air SBD system using FTIR for characterisation and quantification.[39], [109], [160] While these studies provide a valuable insight in to the nature of the species produced, the requirement of placing the SBD into a closed chamber to undertake the measurement precludes the ability to perform spatially resolved measurements. Furthermore, operation of an SBD in a closed volume dictates “batch reactor” like conditions which likely differ from those observed when an SBD is operated in free space, as is the case in many applications.

This chapter presents an investigation that was conducted into the generation and transportation of reactive species, with a particular focus on reactive nitrogen species (RNS) using advanced diagnostic techniques. Laser induced fluorescence (LIF) and particle imaging velocimetry measurements combined with computational modelling gave insight into the underpinning reaction pathways and physicochemical processes governing the species transport. Considering that LIF can provide spatially resolved density measurements of various reactive species with high temporal resolution, it is the ideal technique for determining the distribution of species as they are transported downstream of the SBD. Indeed, previous studies have demonstrated that LIF diagnostics have been successfully applied for the measurement of NO under atmospheric pressure conditions in both helium and argon plasma jets.[60], [61], [161]–[163] The results demonstrate that convection induced by the electrohydrodynamic (EHD) forces from the discharge is the primary mode of transport of reactive chemical species beyond the active plasma region.[142], [164] PIV was used to measure the EHD induced flow under different plasma operating conditions as a means of quantifying the influence of convection on the spatial distribution of NO. In addition, a 2D numerical model, validated using the experimental measurements, was used to determine the spatial distribution of other key RNS beyond the discharge region and uncover the chemical pathways leading to their generation and loss. The findings provide a valuable insight into the role of EHD forces in dictating the spatial distribution of reactive chemical species beyond the plasma generation region, knowledge which can be used to guide the future development of plasma systems for healthcare related applications.

6.2 Experimental setup and methods

6.2.1 Low temperature plasma source

A schematic representation of the SBD used in this investigation is shown in figure 35, the electrode unit consisted of a quartz sheet of 2 mm thickness, serving as a dielectric material. Electrodes were attached either side of the quartz, made from 35 µm thick copper film. The powered electrode was configured as two parallel strips separated by a 15 mm gap, referred to as the discharge gap. The outer edges of the powered electrodes were insulated using Kapton tape to prevent plasma formation on electrode edges beyond the discharge gap.

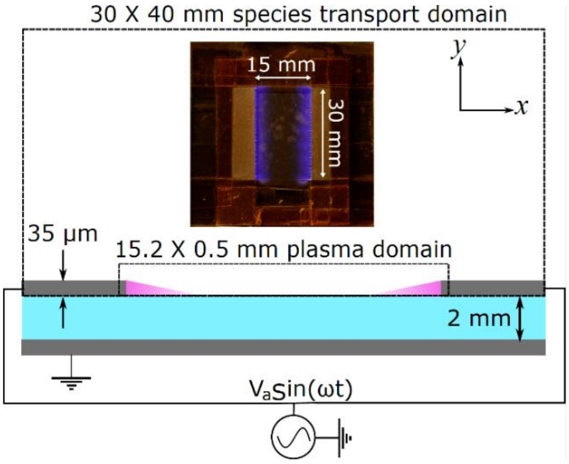

Figure 35: Schematic showing cross-section of the surface barrier discharge used in both experimental and computational investigations (not to scale), insert shows birds eye view of discharge operating at an applied voltage of 15 kV.

The powered electrode was driven by a custom-made high-voltage source capable of producing a sinusoidal output at a frequency of 18 kHz. Two voltage amplitudes of 13 kV and 15 kV were considered in this study. The discharge current and voltage waveforms were measured using a Tektronix P6015A high voltage probe and Pearson 2877 current monitor, recorded using a Tektronix DPO 5054 oscilloscope. Using the measured current and voltage waveforms, the dissipated power within the discharge was calculated and found to be 2.5 W and 4.3 W for the 13 kV and 15 kV cases, respectively. Using the calculated dissipated power at each applied voltage, estimated power densities of 4.67 kW/m^2 and 8 kW/m^2 were determined by dividing the measured power by the area covered by the visible plasma, which was estimated from photographs of the discharge operating at each applied voltage condition; these two cases will be referred to as the low power and high power cases, respectively.

6.2.2 PIV setup

Time resolved and time averaged measurements of the flow field created by the EHD induced flow were obtained via PIV, for the SBD operating under low power conditions (2.5 W). The procedure used mirrored that detailed in chapter 3 (section 3.1).

6.2.3 LIF setup

LIF measurements were conducted for the two power conditions under both steady state and pulsed operation, using the method detailed in the methodology chapter (section 3.2.2). To achieve steady state conditions, the discharge was energised for tens of seconds prior to measurements being taken. To reveal the spatiotemporal evolution of NO, the applied voltage was modulated with a square wave at a frequency of 10 Hz resulting in the plasma being on for 50 ms and off for 50 ms, with LIF measurements being taken at 5 ms intervals over both the on and off time.

6.2.4 Numerical model implementation

The main numerical model directly follows the one described in the methodology section 3.4. For the chemical sub-model, a set of 625 chemical reactions were used which are given in appendix B. The computational domains for both the plasma model and the reactive flow model, are shown in figure 35.

6.3. Results and discussion

6.3.1 Temporal evolution of velocity field

To study the evolution of the EHD induced flow from the SBD, the discharge was pulse modulated with a period of 100 ms and duty cycle of 50 %. During the discharge on-time, the

EHD induced velocity field were measured in a region that extended 10 mm from the dielectric surface and 1 mm either side of the discharge gap. Figure 36 shows the temporal evolution of the velocity field from the instant the 13 kV signal was applied to the powered electrodes (0 ms) over the 50 ms on-time and a further 20 ms of the off-time. From the figure it is clear that the flow originates close to the electrodes edges, in the regions where the visible plasma was observed, and is directed toward the opposite electrode. Between 10 and 20 ms the two opposing induced flows coalesce in the centre of the discharge gap and as a result of conservation of momentum the flow is redirected vertically, forming a jet perpendicular to the dielectric surface. The vertical jet was observed to have a narrow width at the point where the two opposing horizontal flows met which expanded as it propagated away from the dielectric surface. After 40 ms the flow was observed to have reached steady

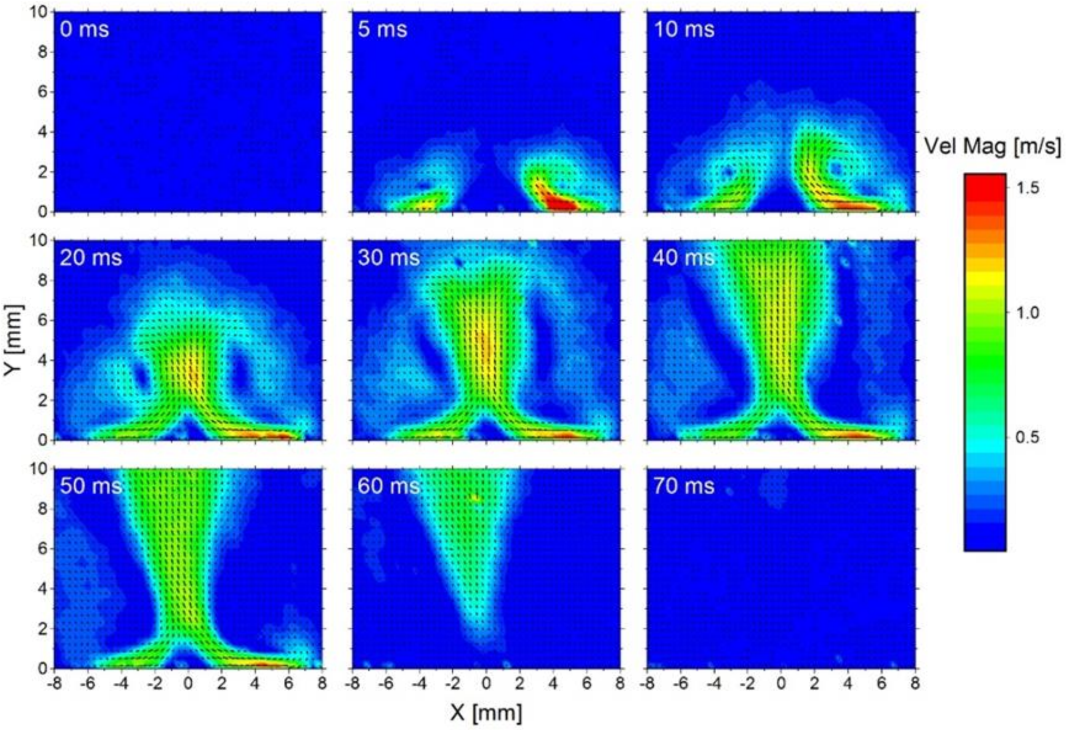

Figure 36: Spatiotemporal evolution of the velocity vector field from the SBD under low power conditions measured using PIV. Time t = 0 ms shows the instant the discharge was energised and t = 50 ms the instant the discharge was terminated.

state conditions, showing no further changes in spatial profile regardless of operation time; consequently, this profile was considered to represent the steady-state conditions. At 50 ms the applied voltage was terminated and a rapid inhibition of the flow parallel to the dielectric surface, as highlighted at 60 ms, was observed. The sudden termination in flow was attributed to friction forces exerted by the dielectric surface. Within a further 10 ms, no flow was observed within the entire measurement domain. Due to slight irregularities in the construction of the SBD device it can be observed that the right-hand side discharge was slightly more intense compared to the left, creating a higher velocity flow leading to a slightly tilted vertical jet.

6.3.2 Temporal evolution of NO generation

The spatiotemporal evolution of NO generation, seen in figure 37, was measured using LIF with the same modulated discharge operation characteristics and time points corresponding to the PIV measurements. The visible artefact seen to appear on the right side of the image at time frames of 0, 60 & 70 ms was attributed to possible contact of the laser beam with the insulating tape on the solid surface of the electrode system and broadband fluorescence. This reflection of the laser beam cannot affect the NO density map and was excluded in analysis of the results.

Following application of the high voltage signal at 0 ms, it can be seen that the NO concentration within the vicinity of the electrodes rose to approximately 300 ppm within 5 ms. Between 5 ms and 50 ms a close correlation can be observed between the profile of ground state NO density and the spatial profile of the induced gas flow, shown in figure 36. As NO molecules are transported vertically away from the dielectric surface the concentration dropped from approximately 300 ppm at the surface to approximately 50 ppm at a distance of 6 mm above the surface. Following termination of the plasma at 50 ms, it can be seen that the NO concentration across the dielectric surface dropped rapidly, while downstream of the dielectric surface several tens of ppm remain.

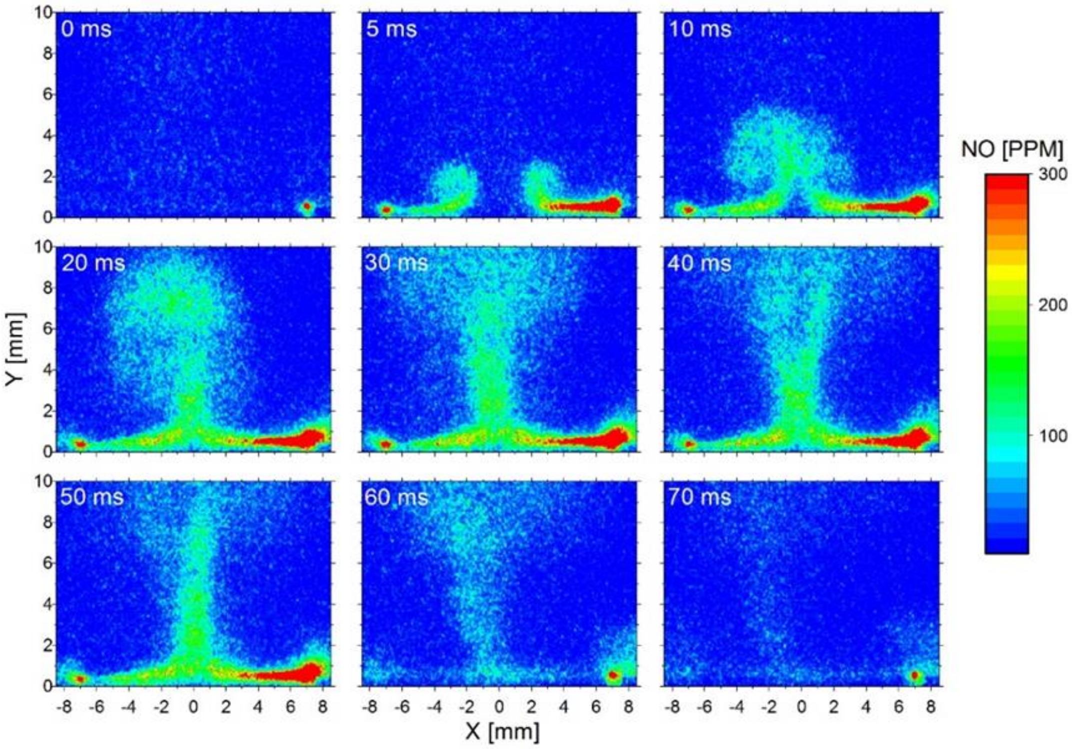

Figure 37: Spatiotemporal evolution of the NO density from the SBD under low power conditions measured using LIF. Time t = 0 ms shows the instant the discharge was energised and t = 50 ms the instant the discharge was terminated.

These measurements indicate that the loss rate of NO in the vicinity of the dielectric surface is greater than that downstream, a comprehensive explanation for this observation is provided in section 3.2. Within 20 ms of discharge termination, the NO concentration was observed to drop to approximately zero everywhere within the measurement domain.

Through comparison of figures 36 and 37, it is very clear that the NO concentration follows the velocity field at any given time. This observation clearly demonstrates that the induced EHD force and the generation of NO occur at the same position (*i.e.* next to the electrode edges where the visible discharge exists) and some proportion of the generated NO is transported by convection to the centre of the discharge gap and downstream along the resultant perpendicular jet. Critically, such observations give credence to the assumptions made in the computational model relating to the generation of reactive species being primarily confined to a small region close to the electrodes edges.

6.3.3 Comparison of predicted & measured parameters

The computational model was validated by comparing the calculated steady state velocity field and resulting spatial profile of NO to those measured under identical conditions. The discharge was run continuously for a few seconds to ensure steady state conditions under both applied voltage conditions. Figure 38 shows the measured and modelled steady state velocity field and NO concentration profile. It is clear that the 2D structure of both the velocity field and NO concentration predicted by the model is highly consistent with measured data. To provide further comparison, both the velocity and concentration data was extracted along a cut line extending from the centre of the discharge gap at the dielectric surface to 10 mm above the surface and plotted in figure 38(e) and (f), respectively. The comparison highlights that the calculated parameters are in good qualitative agreement with the measured values under both of the discharge conditions considered. While the calculated velocity profile showing excellent agreement with the measured values, the predicted NO concentration appears to be less consistent. Notably, it is clear that the model slightly underestimates the NO concentration, particularly close to the dielectric surface, while the agreement improves in the downstream region. This difference can be attributed to the assumptions made in the model relating to the generation of species at the same point in the discharge region. For different discharge voltages, the trend predicted by the model is consistent with the measured data and it is evident that the model can reliably predict not only the trends, but also the absolute concentrations to within an order of magnitude of the measured data.

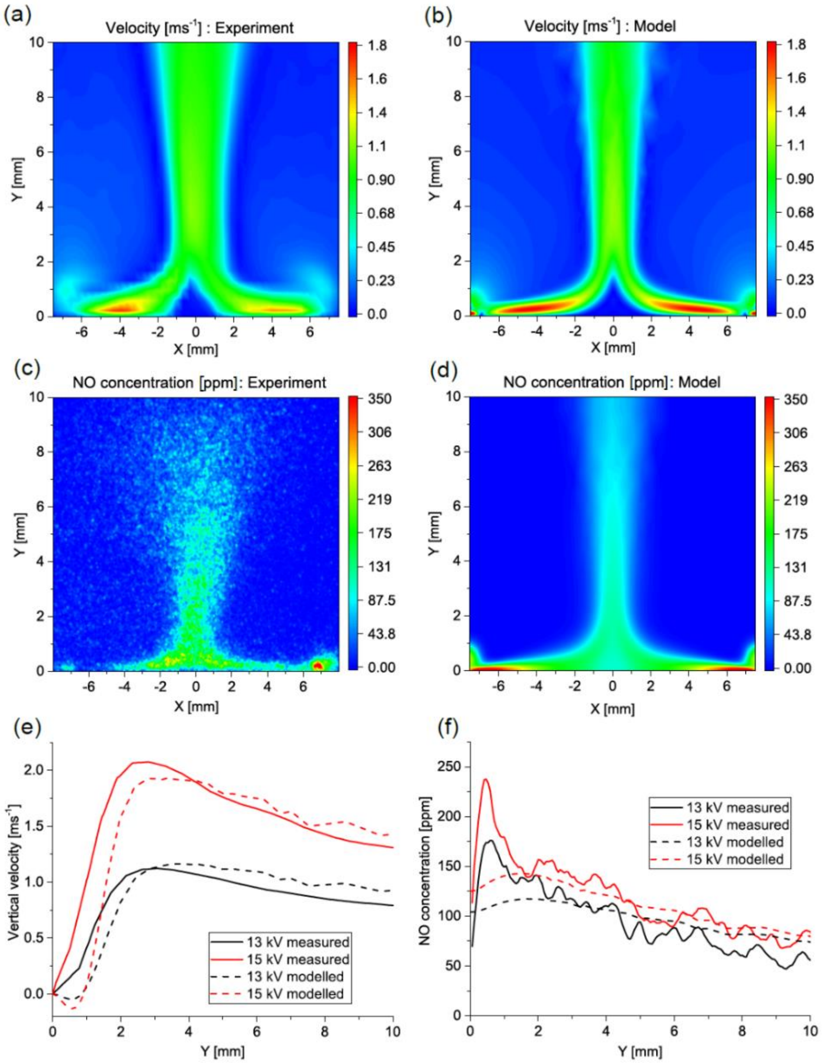

Figure 38: Steady state velocity profiles at an applied voltage of 13 kV: (a) measured data and (b) modelled data. Steady state NO concentration profiles at an applied voltage of 13 kV: (c) measured data and (d) modelled data. (e) Comparison of measured and modelled velocity along a cut line from the discharge gap centre at applied voltages of 13 and 15 kV. (f) Comparison of the measured and modelled NO concentration along a cut line from the discharge gap centre at applied voltages of 13 and 15 kV.

6.3.4 Generation and loss of Nitric Oxide

The computational model was used to identify the dominant reaction pathways leading to the generation and loss of NO and other key RNS species. The dominant generation mechanism of NO is given by reaction (R12), which describes an effective chemical route in which atomic Oxygen reacts with vibrationally excited N_2, forming NO and atomic Nitrogen. Considering that the reaction coefficients describing this chemical pathway do not exist, an effective rate coefficient between atomic oxygen and molecular nitrogen was fitted in air over a range of pressures and temperatures close to ambient conditions, as described by Shimizu, Bansemer *et al*. [39], [160] The dominant loss mechanism of NO is given by reaction (R2) (given in chapter 5, section 5.3.6).

$$O + N_2 \longrightarrow NO + N \qquad \text{(R12)}$$

$$NO + O_3 \longrightarrow NO_2 + O_2 \qquad \text{(R2)}$$

Considering that O and vibrationally excited N_2 only exist in the visible plasma region, close to the electrodes, it can be concluded that this is the only location where any significant amount of NO is generated. NO observed beyond this region can only be attributed to transport by the induced flow. On the other hand, as O_3 is relatively stable and spreads significantly beyond the discharge gap, [165] the loss reaction of NO occurs at every point where NO and O_3 coexist. Hence NO is gradually lost as it is transported downstream through reaction (R2). Based on this insight, it is clear that a combination of the widening of the jet downstream and the loss reaction with ozone are responsible for the decay in the concentration of NO downstream.

The rapid loss of NO at the dielectric surface identified in figure 37 can be explained by two factors, the first is that the O_3 highest concentration was found by the model to reach approximately 200 ppm in the vicinity of the dielectric surface, meaning that reaction (R2) plays a comparatively larger role in this region compared to any downstream location, leading to a higher loss rate of NO in the vicinity of the surface. The second factor is the induced flow, which removes NO from the discharge region to the downstream region. When the applied voltage was increased from 13 kV to 15 kV, the discharge power was increased by a factor of 1.72. This increase in discharge power caused an increase in the induced velocity by a factor of 1.85 at the peak velocity point and a 1.65 increase further downstream. Hence the increase in discharge power caused a proportional increase in the induced velocity field. For the NO concentration, however, the increase in discharge power caused an increase in NO concentration by a factor of 1.37 at the electrode surface and less downstream, as highlighted in figure 38(f). The increase in NO concentration is less than the increase in the discharge power or the induced velocity. As described earlier, NO is mainly generated through reaction (R12) which depends on O. The model shows that the O concentration increases by a factor of ~1.7, which is proportional to the increase in the discharge power. Given that O is an important precursor for both NO, O_3, and many other species the resulting increase in O concentration is essentially distributed across the spectrum of species created from reactions involving O; thus explaining why the NO concentration only increases by a factor of 1.37, compared to that of 1.72 for the discharge power.

6.3.5 Generation and loss of other RNS species

It was established in section 6.3.3 that the model could accurately predict the concentration of NO to within an order of magnitude, it is anticipated that a similar degree of accuracy can be achieved for the many other chemical species produced by the discharge. Under the same experimental conditions as those examined in section 6.3.4, the spatial distribution of a further three key RNS species: N, N_2O, and NO_2, were calculated and are depicted in figure 39.

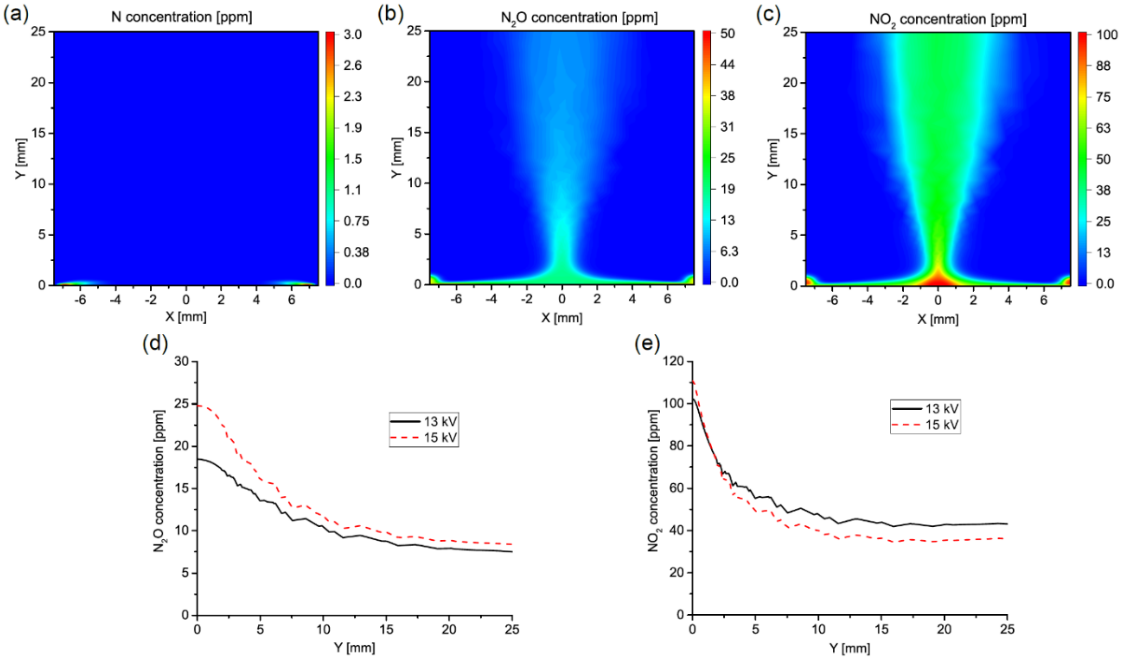

Figure 39: Calculated spatial distribution of: (a) N, (b) N2O and (c) NO2 at an applied voltage of 13 kV. Predicted centre line density profiles of (d) N2O and (e) NO2 for applied voltages of 13 and 15 kV.

From figure 39(a) it is clear than atomic nitrogen, N, is generated only within the plasma region and that it does not live long enough to be transported downstream by the induced flow. This is due to the high reactivity of N, causing it to be lost through rapid reactions, primarily reaction (R13). Despite the consumption of NO in reaction (R13), it is a relatively minor loss pathway for NO in comparison to reaction (R2).

$$N + NO \longrightarrow N_2 + O \qquad \text{(R13)}$$

$$N + NO_2 \longrightarrow N_2O + O \qquad \text{(R14)}$$

Figure 39(b) shows the spatial distribution of N_2O which exhibits clear similarities to the spatial profile of NO, shown in figure 38. Critically, N_2O is primarily generated in the discharge region through reaction (R14) and it is inherently stable. Given that its loss rate due to chemical reactions is negligible compared to its generation rate any reduction in N_2O concentration in the downstream jet region can be solely attributed to the widening of the jet and the dispersal of the molecules over a larger volume. Figure 39(c) shows the spatial distribution of NO_2, similar to N_2O and NO, the concentration of NO_2 reaches a maximum at the centre of the discharge gap and drops as it is transported downstream. NO_2 is mainly generated by reaction (R2). involving both NO and O_3; critically, both of these precursors are present in the induced jet in high concentrations meaning NO_2 is generated in the downstream jet region, away from the discharge. It can be observed that the generation rate of NO_2 downstream counteracts the effect of the widening jet meaning the concentration reduces very slowly as the jet broadens.

The influence of increasing the applied voltage on N_2O and NO_2 concentration is highlighted in figures 39(d) and 39(e), respectively. Similar to NO, the change in concentration of both species is not proportional to the change in the discharge power. This is attributed to both species having at least one precursor species that only depend on the discharge power indirectly, hence the increase in the discharge power is “dissipated” into many cascade reactions leading to the formation of N_2O and NO_2. It is noticeable that the NO_2 concentration decreases in the downstream region as the discharge power is increased, this occurs as a result of the competition between the widening jet and the further generation of NO_2, reaction (R12). An increase in discharge power causes a proportional increase in the flow velocity of the induced jet, while the increase in the generation reaction rate does not increase sufficiently to balance the loss, leading to a shift toward a lower NO_2 concentration in the downstream region.

6.4 Conclusions

The reaction pathways and transport mechanisms of key reactive nitrogen species produced by a surface barrier discharge operating in open air were examined using computational modelling and experimental measurements. Particle imaging velocimetry was used to uncover the induced flow structure created by electrohydrodynamic forces generated by the plasma while laser induced fluorescence was used to obtain measurements of ground state NO density. Both techniques facilitated time and space resolved measurements and were applied to analyse the discharge under two different applied voltage conditions. Steady state measurements of the discharge were used to benchmark the developed numerical model, which was then used to identify the main reaction pathways and predict the behaviour of other reactive nitrogen species.

It was shown that the induced velocity and source of NO both originated at the edge of the driven electrodes which corresponded to the visible plasma region; beyond this region the NO concentration was seen to extend into the centre of the discharge gap and vertically away from the dielectric surface in the form of a perpendicular jet, closely mirroring the measured velocity profile. Along the axis of the induced vertical jet, steady state measurements showed that the NO concentration peaked at the dielectric surface and then dropped downstream. Using the numerical model, it was found that NO is generated through an effective reaction pathway involving vibrationally excited N_2 and atomic oxygen. While the dominant loss reaction of NO was found to be with O_3, creating NO_2. Since both NO and O_3 are transported by the induced flow, the decay reaction contributes to a drop in NO concertation in the downstream region.

In addition to capturing the spatiotemporal behaviour of NO, the model was used to predict the 2D distribution of N, N_2O, and NO_2. It was shown that N is entirely restricted to a region near the electrodes, where it is generated through electron driven dissociation and rapidly consumed by reactions leading to the formation of N_2 and O. The spatial profiles of both N_2O and NO_2 were seen to be similar to NO in that they appeared to follow the induced flow; however, unlike NO and N_2O, NO_2 was found to be created downstream by a reaction involving NO with O_3.

The effect of increasing the discharge power was also investigated and it was shown that the resulting increase in velocity is proportional to the increase in discharge power, while the change in the concentrations of NO, N_2O, and NO_2 does not follow the same trend. This phenomenon occurs because these species are indirectly influenced by the discharge power through a sequence of cascade reactions involving species such as O, which are directly influenced by the discharge power. As the respective increase in the flow velocity is larger than the respective increase in NO and O_3 concentration, which are the precursors of NO_2, increasing the discharge power leads to a drop in the concertation of NO_2, while NO and N_2O concentrations increase as the discharge power is increased.

Overall, this chapter highlighted that significant densities of reactive nitrogen species can be delivered significant distances downstream of a surface barrier discharge. Notably NO, which is of considerable biological importance and a key application enabler, was observed to be transported several centimetres downstream of the discharge region by the plasma induced flow. Through computational modelling the key reaction pathways responsible for the generation and loss of major reactive nitrogen species have been identified and this insight can be used to aid in the development and understanding of plasma-based healthcare devices employing the surface barrier discharge configuration.

Chapter 7: EHD induced flow manipulation

The work detailed in this chapter was reported in: A. Dickenson, Y. Morabit, M. I. Hasan & J. L. Walsh. ‘Directional mass transport in an atmospheric pressure surface barrier discharge’, *Nature Scientific Reports*, 7, 14003, (2017)

Manipulating the phase angle of the applied voltage waveform to the driven electrodes in a surface barrier discharge is shown to exert a level of control over the Electrohydrodynamic forces generated by the plasma. As these forces produce a convective flow which is the primary mechanism of species transport, the technique facilitates the targeted delivery of reactive species to a given downstream point without compromising the underpinning generation mechanisms. Particle Imaging Velocimetry measurements were used to demonstrate that a phase shift between sinusoidal voltages applied to two adjacent electrodes in a surface barrier discharge results in a significant deviation in the direction of the plasma induced flow of neutral species. Using a two-dimensional air plasma model, it was shown that the voltage phase shift impacts the spatial distribution of the deposited surface charge on the dielectric surface between the adjacent electrodes. The modified surface charge distribution weakens the propagation of the discharge ignited on the lagging electrode, thus creating an imbalance in the generated electrodynamic forces and consequently a variation in the direction of the resulting gas flow.

7.1 Introduction

Several of the reactive species generated in the active plasma region of a SBD are confined to the induced convective flow, as seen in chapter 6. In most applications of the SBD, a spatial separation of >> 1 mm is typically employed between the active plasma region and the sample to be treated; this reduces the possibility of intense plasma filaments from interacting directly with delicate substrates (*e.g.* living tissues) and limits the potential for cross-contamination of the sample and electrodes. In such a scenario it is extremely unlikely that charged species or highly reactive neutrals will reach the downstream sample, having a negative impact on application efficacy. [72] To overcome these challenges, several studies have posited that plasma induced electrohydrodynamic (EHD) forces could be manipulated to induce a convective gas flow through the active discharge region, thus transporting reactive neutral species downstream and enhancing mass-transport. [45], [73] Indeed, the previous computational studies of Hasan *et al* [72] have demonstrated that such convective flows could enable the transport of relatively short-lived species, such as OH and NO, to considerable distances downstream of the active discharge region; furthermore, it has been demonstrated that the introduction of a convective flow impacts the generation and loss rates of species in the downstream gas region, resulting in enhanced production of key RONS. [48], [72]

This chapter details an investigation that examined the effects of the application of a phase shift between the voltage waveforms applied to two adjacent electrodes in a surface barrier discharge to exert a level of control over the direction of the EHD force, facilitating the targeted delivery of plasma generated reactive species to a given downstream spatial location. Previous studies exploring the use of SBD devices for aerodynamic flow control applications have reported that the direction of the induced flow can be varied by manipulating the amplitude of the applied voltage or by pulse modulating the voltage applied to adjacent electrodes. [80]–[82] While both of these approaches are effective in steering the induced flow, and therefore meeting the requirements of their intended application, they both rely on impeding plasma formation on one of the electrodes and are therefore not ideal for use when the density and nature of the plasma generated RONS are the key application drivers.

7.2 Experimental Methodology

7.2.1 Plasma source configuration

Two high voltage sinusoidal power sources were used to energise adjacent electrodes in the SBD configuration shown in figure 40(a). A quartz sheet of 1 mm thickness was used as the dielectric material and a single grounded electrode was positioned beneath the quartz to form a counter electrode for both powered electrodes. The power sources consisted of two home-made high-voltage power amplifiers driven by a single low-voltage sinusoidal signal generator (Tektronix AFG3101C). The signal generator provided two sinusoidal outputs at a constant frequency of 15 kHz and was equipped with the functionality to introduce a user-programmable phase shift between the two generated waveforms. The outputs from the high-voltage amplifiers were connected directly to the electrodes shown schematically in figure 40(a). A calibration procedure was employed to ensure that the voltages applied to each electrode were a constant 8 kV peak to peak throughout all experiments.

It is well known that adjacent strip electrodes produce an Electrohydrodynamic (EHD) flow in a direction perpendicular to the dielectric material. [68] In both experimental and numerical investigations, one electrode was energised with a sinusoidal voltage having a phase angle of 0^o, a second sinusoidal waveform was applied to the other electrode with a variable phase angle between +/- 60^o. Figure 40(b) shows the high-voltage waveforms applied to the powered electrodes with a phase difference of +/-15^o.

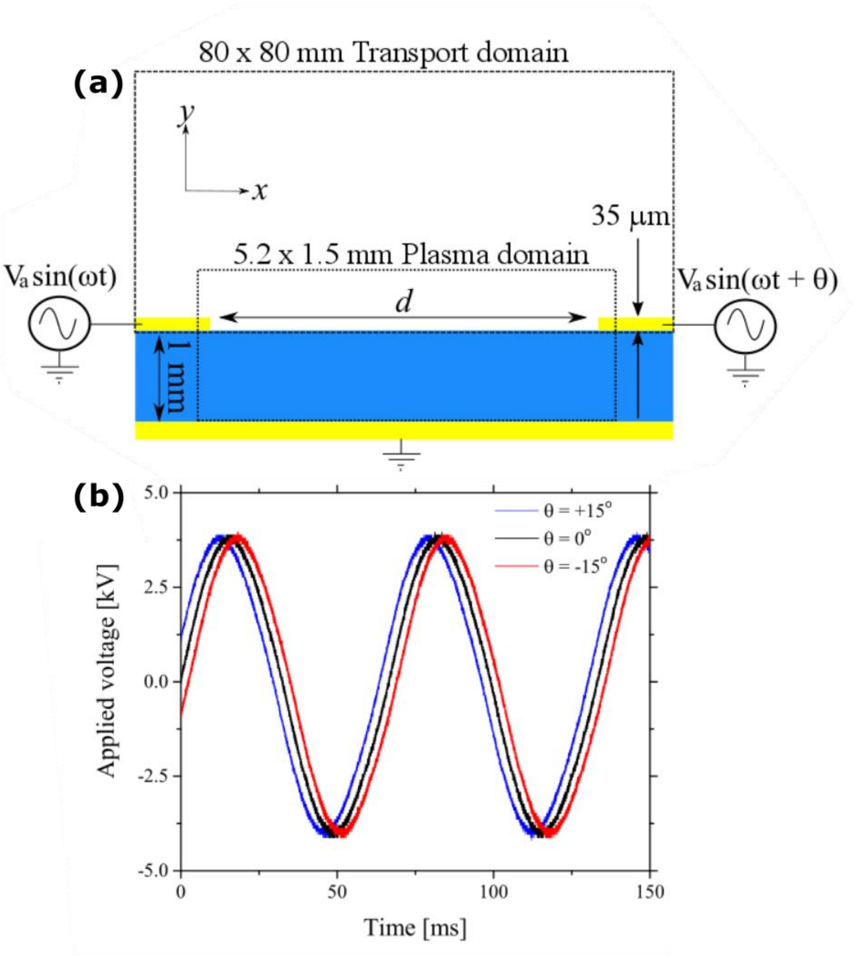

Figure 40: (a) Surface barrier discharge electrode configuration and (b) phase shifted sinusoidal voltage applied to right-hand electrode.

7.2.3 Particle imaging velocimetry setup

Similar to previous chapters, particle imaging velocimetry was used to obtain time averaged measurements of the flow fields created by the EHD induced flow under different operating conditions. Measurements of the induced velocity fields were taken for each of the applied phase shift between +/- 60^o. The procedure used mirrored that described in chapter 3 (section 3.1).

7.2.4 LIF setup

LIF measurements were also conducted to reveal the spatiotemporal evolution of NO for a phase shift between +/-60^o and a discharge gap of 10mm. The methodology used for these measurements reflect those detailed in section 3.2.2 & 6.2.3, using modulation of the plasma discharge as to obtain time resolved measurements. Slight differences were seen in the LIF measurements due to the dielectric thickness being 2 mm instead of 1 mm, as measurements were conducted alongside those seen in the previous chapter.

7.2.3 Numerical model implementation

Using the model detailed in the methodology section 3.4, the plasma model was solved for a single cycle of the non-phase shifted waveform assuming a frequency of 15 kHz. During which the EHD forces, and the generation rate of O3 were integrated in time. Subsequently, the time integrated EHD force field and the time integrated generation rate of O3 were divided by the period and input into the reactive flow and chemical sub-model. The chemical sub-model, used the set of chemical reactions given in the appendix C. While the reactive flow model solved the continuity equation of the gas mixture (air and O3), the Navier-Stokes equation for the gas mixture, and the mass conservation equation for O3. The time-averaged EHD forces and O3 generation rate were introduced in the reactive flow model as source terms in the Navier-Stokes equations and O3 mass conservation equation. The reactive flow part is solved until steady state conditions are reached.

7.3. Results and discussion

7.3.1 Impact of phase shift on induced flow

Particle Imaging Velocimetry was used to quantify the resulting gas flow velocity from the arrangement shown in figure 40. The measured velocity profile generated by the discharge generated by two adjacent electrodes placed 5 mm apart and energised with high-voltage sinusoidal waveforms employing a phase difference of +15°, 0° and -15°, are shown in Figure 41.

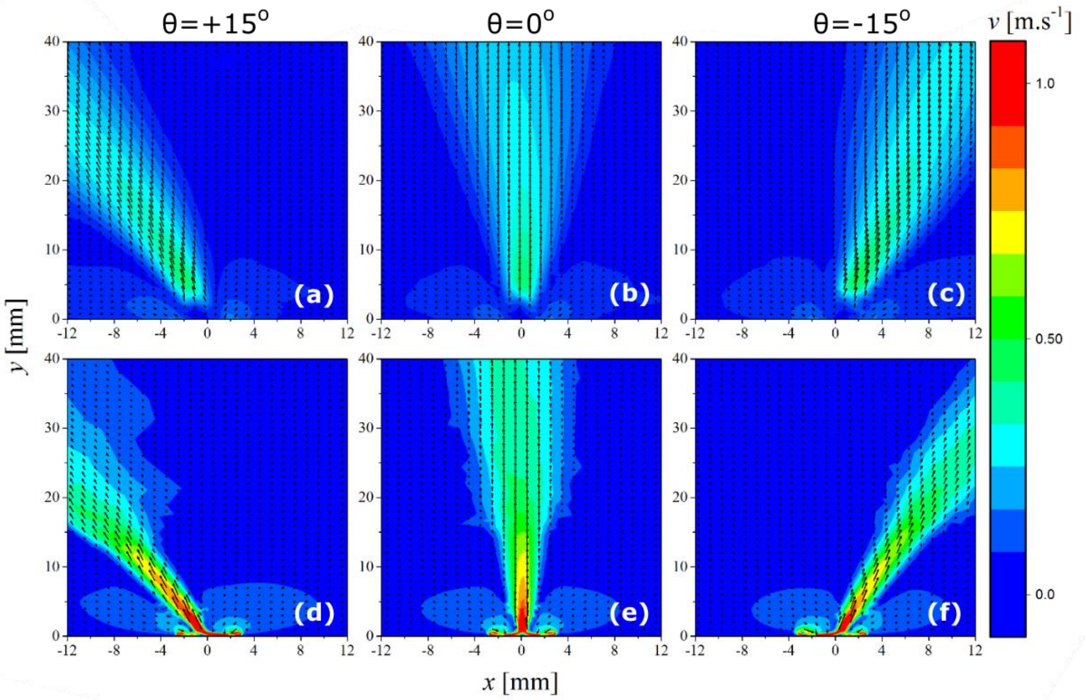

Figure 41: (a - c) Measured velocity vector maps showing impact of a +15°, 0° and -15° phase difference between applied voltages, respectively. (d - f) Calculated velocity vector maps showing impact of +15°, 0° and -15° phase difference between applied voltages, respectively.

Clearly, the introduction of a phase difference between the voltages applied to the individual electrodes resulted in a shift in the direction of the downstream convective flow generated by the plasma. Velocity vectors in the discharge region are not captured due to the limitations of the PIV technique; however, it is clear to see that the introduction of a +/- 15^o phase shift causes a significant deviation in the direction of the flow downstream of the plasma generation region. To assist in identifying the underpinning mechanisms responsible for the observed variation in flow direction, the 2D air plasma model was used. Figure 41 (d-f) shows the calculated velocity profiles obtained by applying phase shifts of $+15^o$, 0^o and -15^o to one electrode, under identical conditions to those used in the experiment. As can be seen, the simulation data closely matches that measured experimentally in the region downstream of the discharge.

The results presented in figure 41 were obtained using a spatial separation between the two electrodes of 5 mm, *d* = 5 mm. The spatial separation between the electrodes was found to be a critical parameter influencing the extent to which the voltage phase difference caused a shift in the direction of the generated gas flow. Figure 42 shows the direction of the generated flow obtained from PIV measurements as a function of the applied voltage phase difference and electrode separation distance. From the presented data it is clear that an increased electrode separation distance yields a less pronounced variation in the direction of the induced flow. At large electrode separations, considered to be *d* => 20 mm in this investigation, the generated flow shows no dependence on the voltage phase difference.

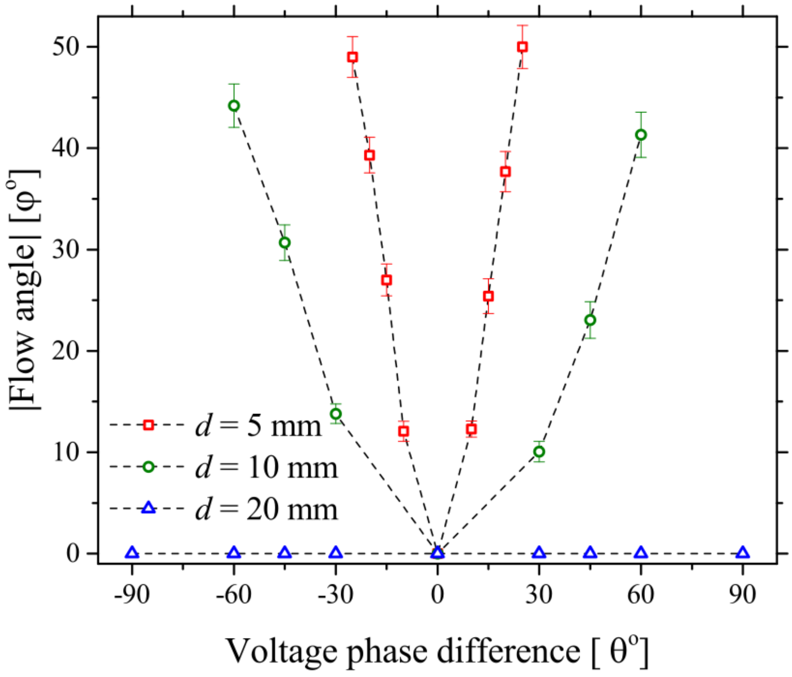

Figure 42: Measured deviation of the electrohydrodynamic flow direction from the perpendicular as a function of applied voltage phase difference and electrode separation distance.

7.3.2 Impact of phase shift on long-lived species generation

From the results presented in figures 410 and 42 it is clear that the use of a voltage phase difference between two adjacent electrodes in an SBD can be used to influence the direction of the induced flow. While it is important from an application perspective to be able to electrically control the direction of species transport and delivery, it is also vital that the method used to achieve this directionality does not impede the production of RONS within the discharge region. To confirm this, the numerical model was employed to calculate the density distribution of ozone 10 mm from the active discharge region for applied phase differences of +15°, 0° and -15°, data shown in figure 43. Regardless of the voltage phase difference, the generated ozone density is seen to remain constant providing a strong indication that the underpinning generation mechanisms are not impacted. Furthermore, the spatial position at which the peak ozone density occurred corresponded directly with the highest velocity region shown in figure 41, confirming that the EHD generated flow was indeed the main mechanism of species transport.

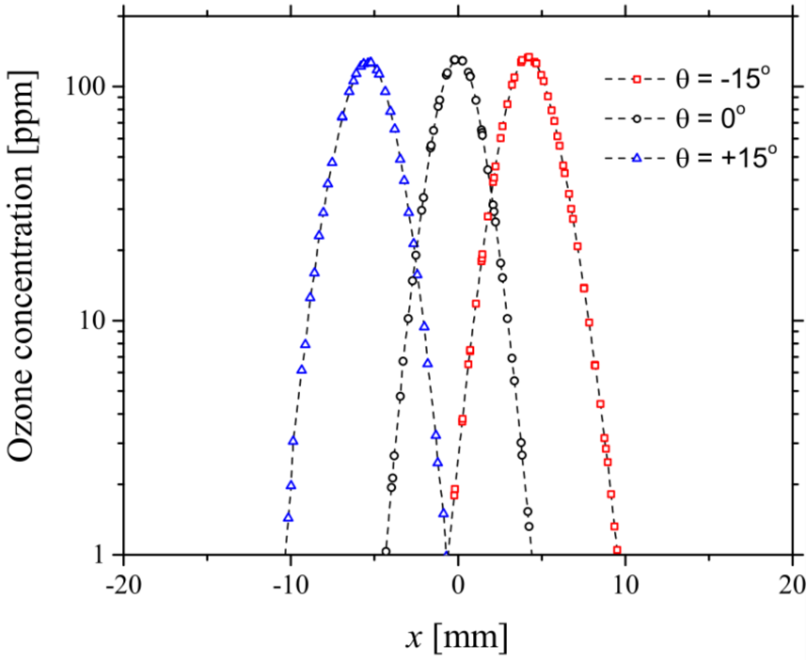

Figure 43: Calculated ozone density 10 mm from the active discharge region (y = 10 mm), for applied voltage phase differences of +15°, 0° and -15°.

7.3.3 Impact of phase shift on Nitric Oxide generation & transport

The effects of phase shifting the energising waveform on the spatiotemporal evolution of NO from a discharge gap of 10 mm is shown in figure 44. Application of a phase difference from +-60° to -60° resulted in a shift in the mass transport of NO from left to right, which resembles the downstream convective flow characteristics seen in section 7.3.1. These results also further confirm the conclusions presented in chapter 5, regarding the induced flow being the primary method of transport of such reactive species. Interestingly, a slight shift of the point in which the two counter propagating flows interact can also be observed from figure 44. As the point at which the two NO density distributions generated by the adjacent electrodes coalesce, are slightly shifted (by ±1 mm). This is explained by the nature of the phenomenon explained in the following section.

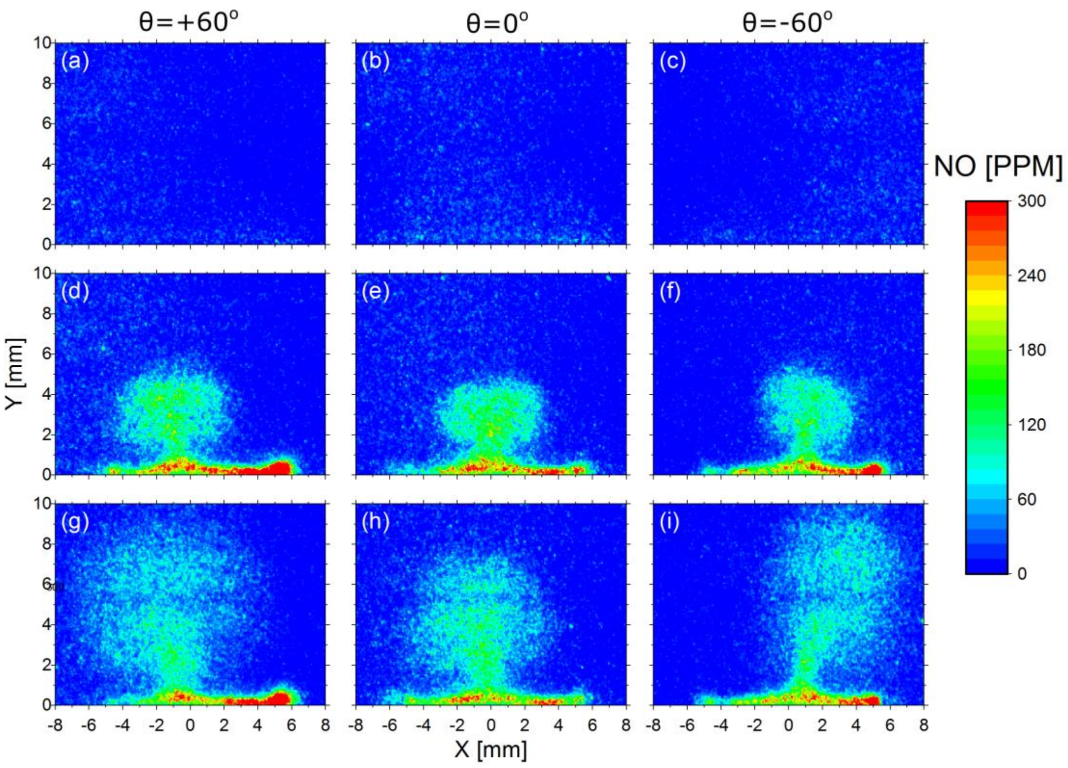

Figure 44: Spatiotemporal evolution of NO for SBD operated under high power condition with electrode separation of 10mm; Before plasma ignition (a-c) 0 ms and after plasma ignition (d-f) 10 ms & (g-i) 20 ms.

7.3.4 Underpinning mechanisms of phase controlled EHD transport

While the results presented in figures 41 - 44 fully demonstrate the utility of the approach, the underpinning mechanisms behind the phenomenon are yet to be explained and likely differ significantly from other studies examining directional control of flow for aerodynamic applications. In previous studies, efforts have been directed toward impeding the flow generated from one of the electrodes, enabling the flow from the other electrode to dominate and thus causing a change in direction of the overall fluid flow. Such efforts include using a lower voltage on one electrode or by pulsing the applied voltage to the electrodes with a significant time delay (> ms) which enables the flow from one electrode to fully develop before the other is ignited. In this study a phase shift is employed between the voltage waveforms applied to adjacent electrodes. As the operating frequency employed in this study is a constant, a phase difference of 15^o represents a time delay of 2.78 µs between the two waveforms, a delay that is several orders of magnitude lower than those used in previous studies. [82] As the fluid flow is known to develop on a millisecond timescale in a dielectric barrier discharge it is surprising that such small time delays have a significant impact on the direction of the fluid flow.

Given that the change in flow direction is a function of the spatial separation between the adjacent electrodes, it is reasonable to assume that the phenomenon occurs due to a mutual interaction between the discreet plasmas generated on each electrode edge. Clearly, as the two propagating discharges are placed closer together, their interaction becomes increasingly intense. In an SBD, the discharge is in the form of streamers that are ignited at the edge of the electrode and propagate rapidly (<50 ns) across the dielectric surface, resulting in charge deposition on the surface. Streamer propagation continues until the electric field at the streamer tip becomes insufficient to initiate new electron avalanches. Upon termination, the quasi-neutral region behind the streamer tip gradually decays through a process of recombination and further charge deposition on the dielectric surface. When an adjacent electrode is placed in close proximity, streamers from both electrodes propagate towards each other and the possibility for mutual interaction arises. To investigate this, the numerical model was employed to calculate the maximum surface charge density deposited on the dielectric surface during streamer propagation from two adjacent electrodes placed 5 mm apart. The resulting surface charge density profiles are shown in figure 45.

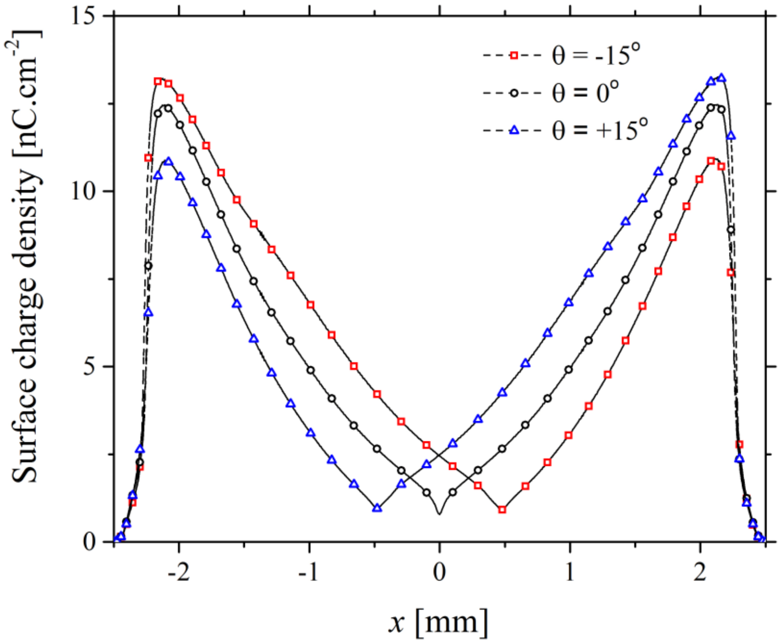

Figure 45: Calculated surface charge density for applied voltage phase differences of +15°, 0° and -15°.

The surface charge density profiles presented in figure 45 demonstrate that a phase difference between the applied voltage waveforms causes a distortion in the deposition of charge on the dielectric surface. Taking the -15° phase difference case as an example, a streamer originating from the electrode positioned at -2.5 mm is the first to be ignited due to the phase difference and subsequently propagates towards the adjacent electrode depositing charge on the dielectric surface. A short time later, a second streamer is ignited from the adjacent electrode situated at + 2.5 mm and begins to propagate; however, the positive charge deposited by the first streamer covers more than half of the dielectric surface between the electrodes. The presence of positive charge on the dielectric surface impedes the propagation length of the second streamer. As a result, the minimum surface charge density point is closer to the electrode situated at + 2.5 mm. Essentially, propagation is terminated at $x = 0.5$ mm for both streamers, meaning the length of the streamer originating from the electrode at -2.5 mm is 3 mm and the streamer originating from the electrode at +2.5 mm is 2 mm . When a phase difference of +15^{o} is applied, the same process occurs with the first streamer originating from the electrode edge at +2.5 mm and the minimum surface charge point is at x = -0.5 mm, closer to the -2.5 mm electrode. In the case when no phase difference is applied, both streamers ignite simultaneously, demonstrated by the location of the minimum surface charge point being exactly in the middle between the two electrodes.

In an SBD the EHD force is generated by the movement of charged species drifting in the electric field, resulting in momentum transfer to neutral species through repeated collisions. This force exerted as the streamer tip propagates away from the electrode. Given that the localised electric field in the streamer is determined by the voltage difference between the streamer and the voltage due to deposited surface charge, it is to be expected that any distortion in the surface charge profile would subsequently impact upon the force generated by the propagating streamer. [166] Figure 46 shows the time-averaged force exerted by the streamers generated from adjacent electrodes for phase differences of -15^{o}, 0^{o} and +15^{o}.

From the figure it can be seen that the introduction of a phase difference results in a shift of the equilibrium position of the horizontal force (the point where the force is zero), indicating that the force by one streamer acts over a longer distance than the streamer ignited by the opposite electrode. Interestingly, the location of the equilibrium point coincides with the minimum surface charge points shown in figure 45.

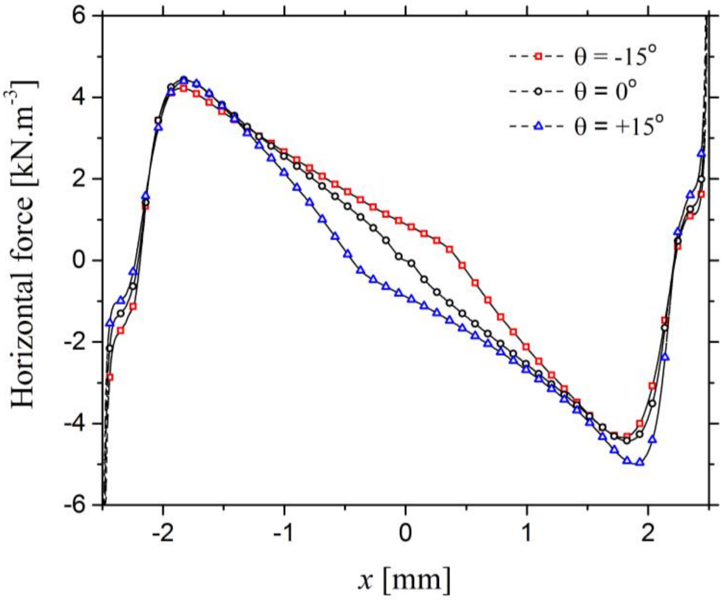

Figure 46: Calculated time-averaged horizontal force generated by the plasma for applied voltage phase differences of $+15^o$, 0^o and -15^o.

The implications of this shift in the equilibrium position is that a net horizontal force is exerted on the flow by the force acting on a longer distance. Consequently, this shift in the equilibrium position causes the direction of the resulting gas flow to diverge from the expected perpendicular direction. In the case of a -15^o phase difference, the equilibrium position of the force is shifted towards the electrode situated at +2.5 mm, thus the resulting gas flow is observed to bend towards the right-hand side, as seen in figures 41(c) and 40(g). Conversely, a $+15^o$ phase difference results causes a shift in the equilibrium position of the force to the left, thus causing the resulting gas flow to bend to the left, as seen in figures 41(a) and 40(d). When no phase difference is applied, the equilibrium position of the force is in the centre of the dielectric surface, resulting in gas flow that is directed away from the dielectric surface in a perpendicular direction, as seen in figures 41(b) and 41(e). Critically, as the electrodes are moved further apart, the localised electric field in the region around each electrode becomes less distorted by the presence of the streamer propagating from the adjacent electrode. In this situation the force exerted by each streamer remains constant and no force imbalance occurs regardless of the applied voltage phase difference, explaining the results presented for *d* = 20 mm in figure 42.

7.4 Conclusions

A technique has been presented that enables the direction of reactive species transport in a SBD to be manipulated without compromising the generation efficacy of the reactive species. By applying a phase difference between the voltages applied to adjacent electrodes in an SBD an imbalance in the EHD forces generated by the propagating streamers occurs, yielding a change in the direction of the EHD induced gas flow. Voltage phase differences between +/- 60^o were investigated and shown to give rise to shifts in the gas flow direction of +/- 50^o from the conventional perpendicular direction.

A 2D numerical air plasma model was used to investigate the underpinning physical processes giving rise to the observed phenomenon. Using the model it was determined that an interaction occurs between the two counter-propagating streamers as a result of a distortion in the charge deposition profile in the region between the two electrodes. The profile of charge distribution between the two electrodes influences the localised electric field which in turn impacts the EHD forces generated by each streamer.

Through the introduction of a phase difference between the applied voltage waveforms, it was established that one streamer was able to propagate longer and exert force in its direction of propagation over larger distance compared to that by the streamer originating from the opposite electrode, resulting in a shift in flow direction.

As the generation of reactive plasma species is not compromised by the introduction of a phase difference between the two applied voltage waveforms, this technique can be safely used to facilitate the targeted delivery of plasma generated reactive species to a given downstream location without compromising generation efficacy. Essentially, the technique could be used to enable large area samples to be uniformly exposed to plasma generated species using a smaller and potentially non-uniform SBD electrode.

Chapter 8: Surface Barrier Discharges for microbial inactivation

Bacteria in the natural environment are rarely found in a dehydrated state, understanding the interaction between plasma generated species liquid media is a crucial step in optimising the SBD for microbial inactivation. In this chapter Plasma activated water (PAW) was generated using an SBD using the lessons learnt in previous chapters. The PAW was used to indirectly treat several pathogenic microorganisms prevalent in nosocomial infections and the decontamination efficacy was compared to that of other fluids of a similar pH including nitric/acetic acids. Gram-negative strains of bacteria were seen to be more susceptible to PAW treatment than gram-positive strains. Nitric acid displayed different kill kinetics than that seen from PAW indicating that the nitric acid present in PAW is not solely responsible for its biocidal activity. Acetic acid was found to be the most effective at decontamination despite it having a higher pH value than PAW & nitric acid, indicating that the chemical composition of the liquid is a key factor for bactericidal activity rather than pH alone. The decontamination efficacy of a plasma treated buffer solution (sodium phosphate) was also assessed and found to have negligible biocidal activity. This was considered to be a result of the chemical pathways leading to the generation of active species responsible for the antimicrobial action being inhibited by the buffer solution.

8.1 Introduction

Within the healthcare sector, microbial decontamination is of great importance, especially in the context of reusable and invasive medical devices. While several conventional thermal-based decontamination techniques are extremely effective, many of the materials commonly used in medical devices are thermosensitive. The use of such thermal techniques, or aggressive chemical treatments can cause morphological or chemical changes to the material surface and thus alter viability. Therefore the need for less aggressive decontamination techniques, that don't adversely affect surface properties, are in great demand. [146] [167]

While the use of the effluent of gas phase plasmas has been used for decades it can also cause morphological or compositional changes to exposed surfaces, especially those polymeric in nature. Given this and that bacteria in the natural environment is often found in a hydrated state, several researchers have explored the use of plasma activated water (PAW) for microbial decontamination. In this scenario, plasma species are directed towards a volume of water either through direct or indirect exposure, the flux of RONS reaching the liquid layer induce both physical and chemical changes. The 'activated' liquid is subsequently applied to the decontamination target. *Tian et al* demonstrated that PAW obtained through surface jet treatment whereby the plume of a plasm jet impacted the surface of the water sample, was less effective at bacterial decontamination than PAW obtained through submerged jet treatment in which the plume was placed beneath the surface of the water. Indicating that the gas-liquid boundary significantly impacts the chemical pathways that lead to bactericidal species generation. [168] These finding along with those from recent studies indicate that a wide number of factors affect the chemical composition of the treated liquid and its subsequent antimicrobial action. [86], [87], [169] Given the wide variation in antimicrobial efficacy of PAW reported in the literature and the complexity of the arising liquid chemistry much work is still required to gain a complete understanding of the underpinning decontamination modes of action. Recent studies have investigated the liquid phase chemistry and shown that the generation of $H_2O_2, ONOO^-, HNO_2\ and\ HNO_3$ are all possible in PAW.

This chapter considers the use of an indirect SBD treatment to activate distilled water which is subsequently used to decontaminate several healthcare relevant pathogens, including *A. baumannii, P. aeruginosa & K. pneumoniae S. aureus* & *E. faecalis C. albicans*. To gain an understanding of the underpinning decontamination pathways the inactivation kinetics are compared against those obtained using Nitric and Acetic acid solutions with a pH matching that of the generated PAW.

8.2 Experimental Methodology

8.2.1 Plasma system configuration

Findings from the previous chapters were used to construct an effective plasma system for treating fluids. To increase the total plasma surface area circular discharge gaps with a diameter of 5 mm were employed, as sub 5 mm diameter gaps increased the required applied breakdown voltage exponentially, discussed in chapter 4. The SBD device construction consisted of two copper electrodes, each with a diameter of 58 mm and 0.2 mm thickness. The electrodes were adhered to either side of a fused quartz disc of 75 mm diameter & 1 mm thickness. One electrode was perforated with the circular discharge gaps (5 mm diameter), thus forming 41 individual regions for plasma generation over the electrode surface. The perforated electrode was connected to the ground of the power source while the non-perforated electrode was connected to the high-voltage output terminal of the power source. On application of a sufficiently high voltage an air plasma discharge was observed to form within the 41 holes on the perforated sheet. The SBD electrode was confined in a sealed enclosure to maximise the contact time of plasma generated reactive species. The volume of the container was sufficient to house a 90 mm diameter Petri dish, when filled with 20 ml of water, the separation of the liquid surface to the region of plasma generation was approximately 2 mm.

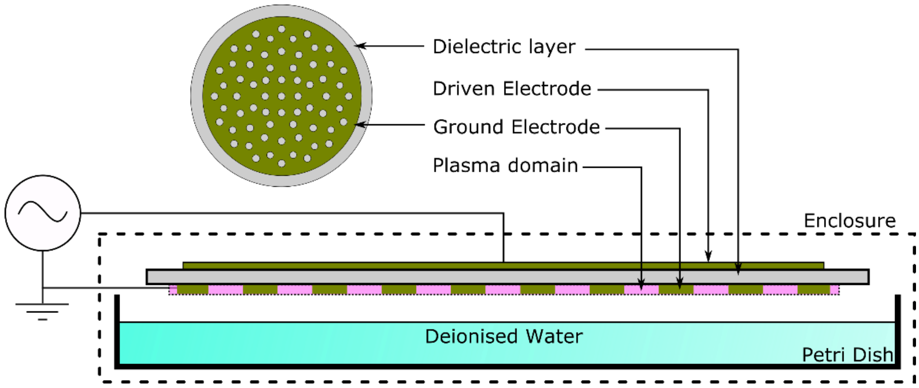

Figure 47: Schematic of SBD plasma fluid treatment system.

A 24 kHz sinusoidal voltage amplifier was used to generate an output voltage of 9.4 kV pk–pk. Variable discharge powers were investigated but only treatment at the highest investigated power of 19.7 W was sufficiently effective at reducing the microbial counts for a comparison to be made. As described in previous chapters, low power operation (< 7 W in this investigation) favours the generation of ROS dominated chemistries and high-power operation (>11 W in this investigation) favours the generation of RNS dominated chemistries. Electrical measurements were made using a Tektronix B051469 voltage probe and a Pearson 115617 current probe connected to a Tektronix DPO 5054 500 MHz 5 GS/s digital oscilloscope.

8.2.2 Gas & liquid phase species measurements

The concentration of ozone was measured in the gas phase via a 2B technologies 106-M ozone monitor while the Indigo colorimetric technique and HPLC were employed for measurement of dissolved ozone and nitrogen species $(NO_2^- \& NO_3^-)$ in the liquid phase respectively, as detailed in the methodology chapter (section 3.4).

8.2.3 Investigated Microorganisms

Six different microorganisms were used in this investigation, two gram-positive bacteria, three gram-negative bacteria and a fungus. The gram-positive strains included *S. aureus* 9144 and *E. faecalis 775*, while the gram-negative strains included *A. baumannii AYE*, *P. aeruginosa PA01*, *K. pneumoniae* 13368. In addition, the fungal strain *C. albicans* 03179 was also investigated. All strains were chosen due to their pathogenic nature and their prevalence in healthcare related nosocomial infections. A mixture of gram negative and positive strains along with a fungal species were selected as a means of comparison between structurally different microorganisms.

8.2.4 Preparation of cultures

Overnight cultures were produced by suspending each strain in 5 ml of tryptic soy broth (TSB). After a 24 h incubation in a Gallenkamp Orbital Incubator (37 °C, at 200 rpm) optical densities of each culture was taken using a Spectrophotometer. 5 mL suspensions of each strain were then diluted to a concentration of 10^{-7} CFU ml^{-1} by adding the calculated amounts of each overnight culture to TSB.

8.2.5 PAW production

This investigation looked at two different fluids treated with plasma, de-ionised water (pH 6.0) and the buffer solution Sodium Phosphate (pH 6.37). Treatment was performed by placing 20 ml of fluid in a 90 mm Petri dish with a 28 mm stir bar. The samples were sealed within the plasma system enclosure and placed on a magnetic stirrer, set to a stir rate of 200 rpm. The plasma was then energised for the duration of the treatment time at the discharge power under investigation.

8.2.6 Preparation of acid solutions

Two acids of a similar pH were used for comparison to the results obtained from a PAW solution created using a 30 minute plasma exposure (PAW-30). Nitric acid (pH 1.97) and Acetic acid (CH_3COOH, pH 2.24) were used for comparison to PAW. HNO_3 was chosen as it is believed to be one of the products resulting from the interaction of plasma generated RONS and liquid. The active species present in Acetic acid were expected to be entirely different to those found in PAW, thus allowing for a comparison based solely on pH.

8.2.7 Microorganism treatment

The plasma treated fluid (PTF) and acids were added to each strain at a 10:1 dilution ratio (*i.e.* 225 µl of PTF/acid to 25 µl of strain suspension) in a 96 well plate and held for a contact time of 0, 2.5, 5, 10 & 30 minutes (0 minutes was conducted using untreated de-ionised water). After each contact time a dilution series of 1:10 steps were taken for each sample, to a dilution factor of 10^6. Each dilution series was then plated out onto Tryptic Soy Agar (TSA) plates in three 10 µl spots, which were then left to incubate at 37 °C for 24 hours.

8.2.8 Quantification of CFUs

Colonies that were present on the TSA plates after a 24 hour incubation were manually counted with the aid of a backlight. The colony forming units (CFU) for each of the treated samples were then calculated to quantify the changes in the number of active colonies before and after treatment of microorganisms with each PTF/acid. The optical densities of each 96 well plate were taken after 24h incubation using a BMG Labtech, Fluostar Omega Plate reader.

8.3 Results and discussion

8.3.1 Gas phase ozone

At the lowest investigated power (7 W) a relatively constant concentration of ozone (~400 PPM) was produced in the gas phase, when the power was increased the concentration of O_3 rapidly decreased with time until O_3 production was totally inhibited, indicating ozone poisoning had occurred, as seen in figure 48. As previously discussed the rapid production of RNS species [49][3] leads to catalytic reactions and the transition of the gas phase species from ROS dominant to RNS dominant regime.

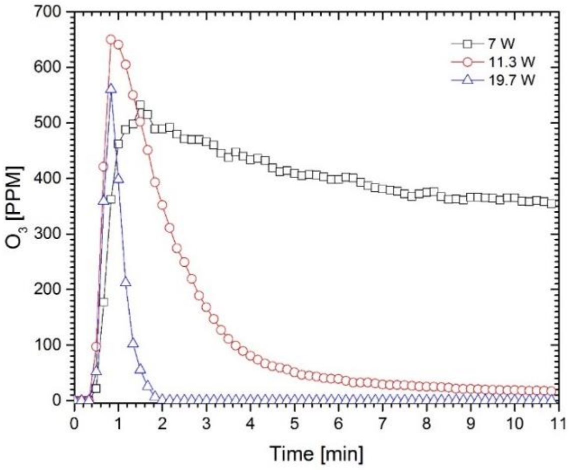

Figure 48: Temporal evolution of ozone in the sealed discharge reactor for different discharge powers.

8.3.2 Liquid phase ozone

The aqueous phase O_3 concentration as a function of discharge power at a constant treatment time of 15 minutes is shown in figure 49. Operating the plasma system at 11.3 W presented the most effective condition for O_3 generation in water (0.28 mg/L). Increasing the dissipated power above this value drastically reduced the concentration of O_3; at the discharge power of 19.7 W used in this investigation, just 0.07 mg/L of aqueous phase O_3 was measured.

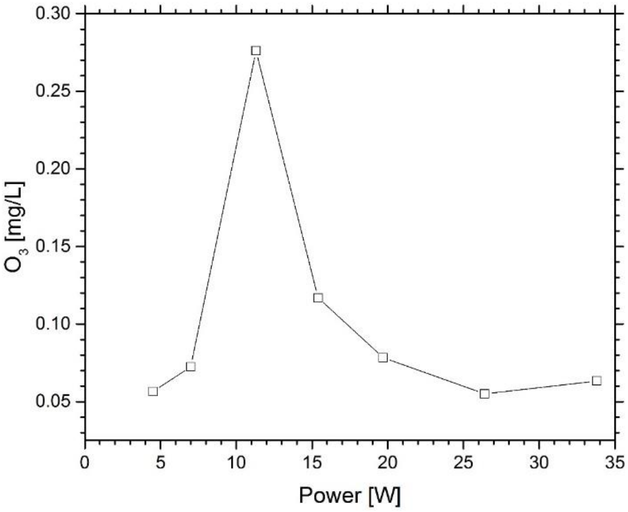

Figure 49: Ozone concentration in water after 15 minute plasma treatment, at different dissipated powers.

Figure 50 illustrates the temporal evolution of O_3 for the optimum power condition (11.3 W) identified in figure 49, and that observed in the highest investigated power condition. At 11 W it takes approximately 12 minutes to reach a stable concentration of 0.28 mg/L. The concentration of O_3 is seen in greater quantities at shorter treatment times for the high-power state compared to optimal operation power but is reduced to a minimum 0.06 mg/L for treatments >15 minutes. Notably, this trend is similar to that observed for gas phase O_3 under high power operation, where O_3 is seen to increase initially, followed by a rapid decay due to poisoning.

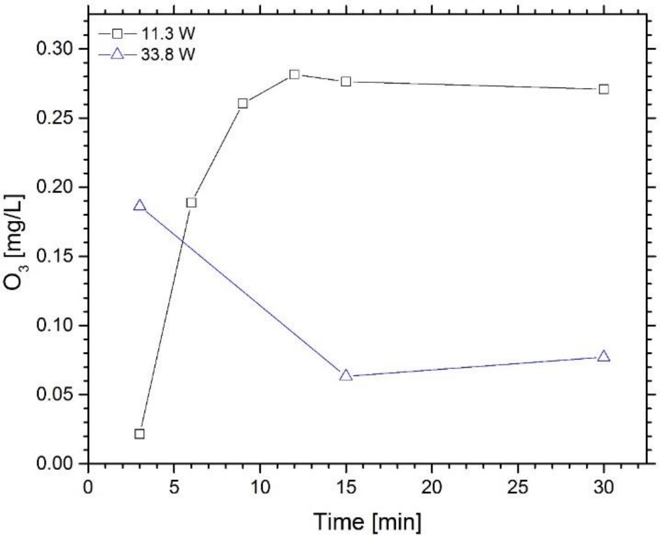

Figure 50: Temporal evolution of ozone concentration in water at at deposition powers of 11.3 & 33.8 W.

8.3.3 Liquid phase nitrites & nitrates

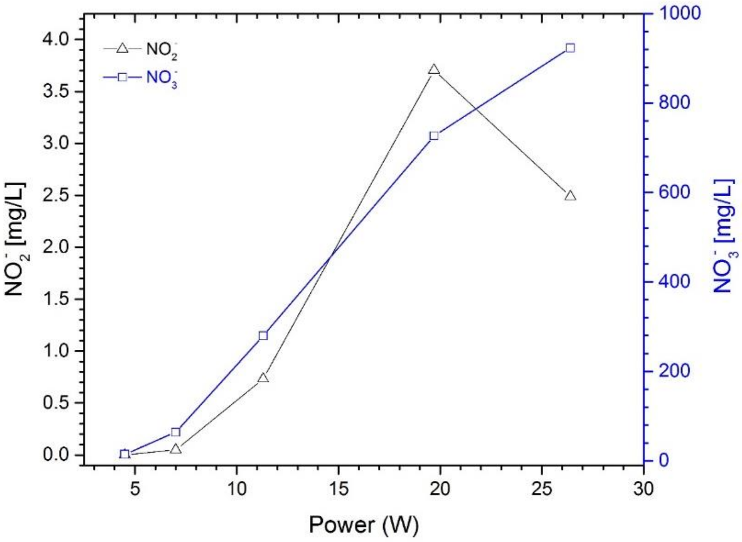

Figure 51: Nitrite & nitrate concentration in water after 15 minute plasma treatment, at different dissipated powers.

The concentration of NO_2^- and NO_3^- that are generated in the deionised water after plasma treatment is dependent on the discharge power, as seen in figure 51. Both NO_2^- and NO_3^- increased in concentration with higher discharge power until a certain threshold. Treatment at 19.7 W produced the highest concentration of NO_2^-, 3.7 mg/L and a significant quantity of NO_3^-, 726 mg/L. Operation at powers >19.7 W caused NO_2^- concentration to fall while NO_3^- continues to increase, this occurs as a result of the nitrite to nitrate conversion from reactions with NO and the increased rate of reactions under acidified conditions.

8.3.4 Acidification & conductivity

The pH of the deionised water gradually decreased over time when treated with plasma while the conductivity was observed to increase. The rate at which acidification of water occurred and conductivity increased was strongly dependent on the discharge power. The change in pH and conductivity over a 30 minute treatment time for the 19.7 W power condition is presented in figure 52.

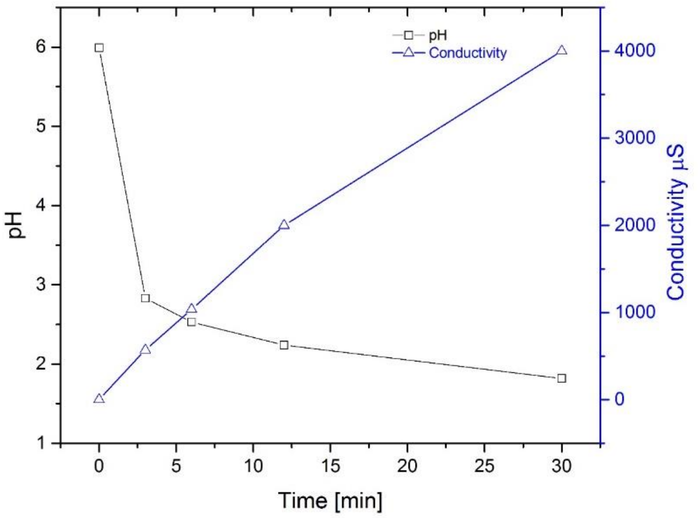

Figure 52: Temporal evolution in the pH & conductivity of water after plasma treatment at a dissipated power of 19.7 W.

8.3.5 Bactericidal efficacy of PAW-30

The plasma treatment duration, microorganism contact times and power level to use for best comparison between the bactericidal efficacy of PAW and the investigated fluids were realised from preliminary trial and error testing. PAW obtained from a 30 minute plasma exposure (PAW-30) at 19.7 W exhibited the highest decontamination efficiency for all strains used, thus these parameters were set as constants in the decontamination investigations.

The kill kinetics that were obtained in this investigation for PAW (pH ~1.82) under different contact times on all strains are displayed in figure 53. All gram-negative strains displayed high susceptibility to contact with PAW, with a contact time of just 2.5 minutes reducing *A. baumannii, P. aeruginosa and K. pneumoniae* were reduced by 4.59, 8.62 and 6.38 log respectively. The CFU counts for these strains were seen to be reduced to the limit of detection (represented by dotted line) when in contact with PAW for 20 minutes or less (In most cases this limit was reached after just 2.5 minutes). Gram-positive bacteria strains *S. aureus and E. faecalis* were more resistant to PAW compared to the gram-negative strains, with a 2.5 minute contact giving 1.46 and 3.62 log reduction for *S. aureus and E. faecalis*, respectively. Following a 20 minute contact, *S. aureus and E. faecalis* were reduced by 2.05 and 5.37 log, respectively. PAW displayed no antimicrobial effect on *C. albicans* as no reduction in CFU counts detected, regardless of contact time.

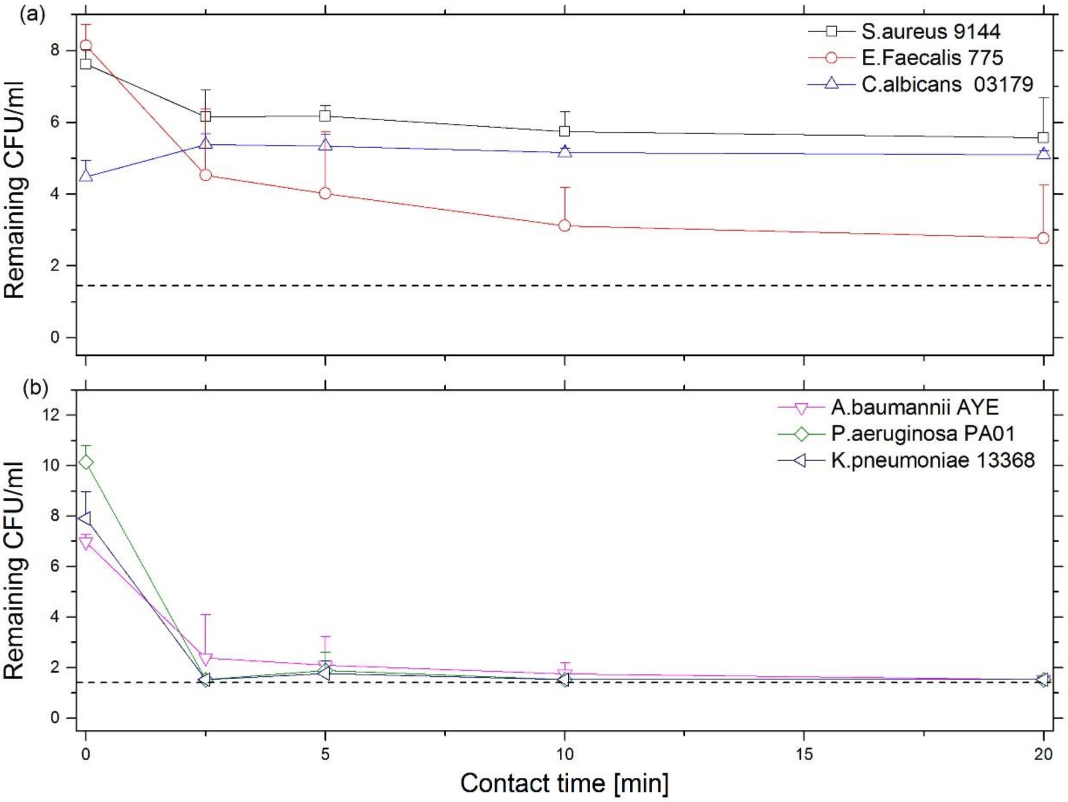

Figure 53: Log reductions of investigated strains CFU/ml with contact times up to 20 minutes with PAW-30 (pH 1.82); (a) S. aureus, E. faecalis & C. albicans *(b)* A. baumannii, P. aeruginosa & K. pneumoniae*. Dotted line represents limit of detection.*

8.3.6 Bactericidal efficacy of Nitric Acid

Figure 54 shows the bactericidal reduction when each strain was exposed to HNO_3. The only strain to be significantly affected through contact with $HN0_3$ was P.aeruginosa, of which a reduction of 8.02 log CFU/ml was seen after a 5 minute contact. Both A.baumannii and K.pneumoniae showed a slight reduction in CFU counts over the full contact time range, after 20 minutes contact with HNO_3 the CFU counts reduced by 2.4 and 4.04 log CFU/ml, respectively. All other microbial strains showed resistance to contact with HNO_3, demonstrated by no significant change in CFU/ml after the full 20 minute contact time.

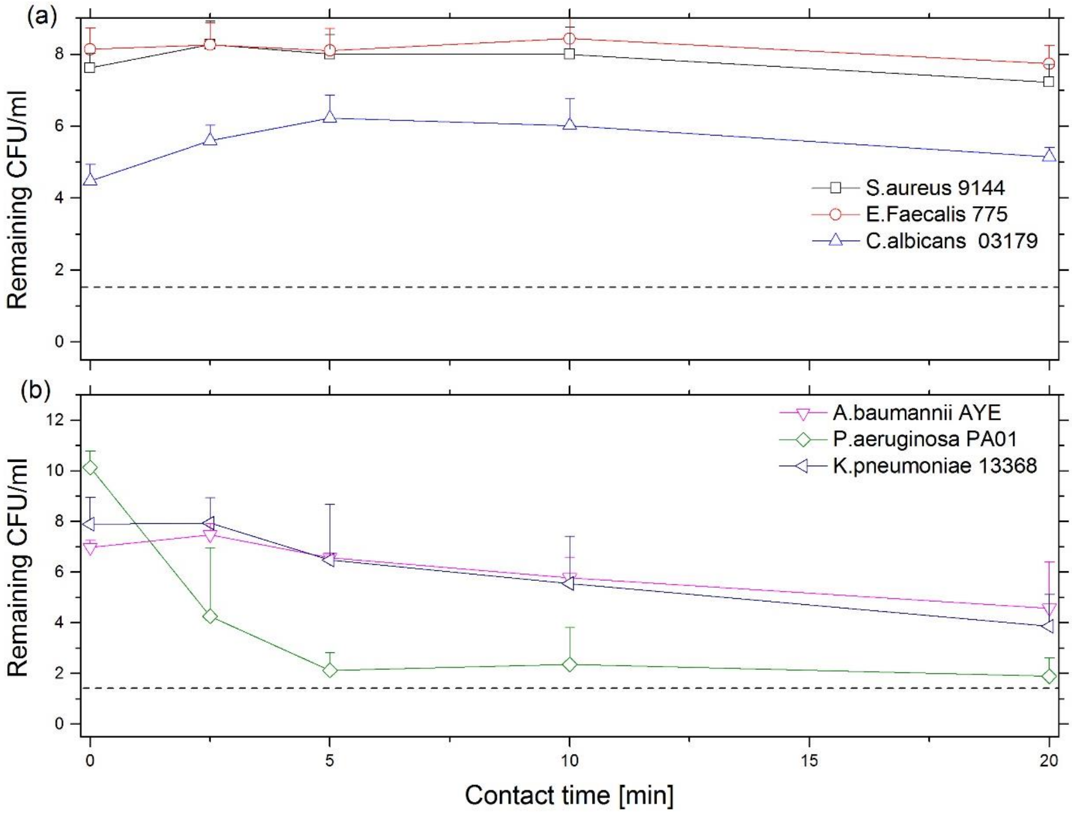

Figure 54: Log reductions of investigated strains CFU/ml with contact times up to 20 minutes with nitric acid (pH 1.97); (a) S. aureus, E. faecalis & C. albicans (b) A. baumannii, P. aeruginosa & K. pneumoniae. Dotted line represents limit of detection.

The results seen from these experiments suggest that the nitric acid that is known to be present in PAW cannot solely be responsible for its antimicrobial efficacy for most strains; however, it could play a role when it comes to inactivation of *P. aeruginosa*.

8.3.7 Bactericidal efficacy of acetic acid

After a contact time of 2.5 minutes with acetic acid, the CFU counts for all strains were reduced significantly, as seen in figure 55. *S.aureus* & *E.faecalis* were reduced by 6.1 and 5.39 log, respectively. *A.baumannii, P.aeruginosa* & *K.pneumoniae* were reduced by 5.46, 8.29 and 6.38 log, respectively, and C.albicans was reduced by 1.84 log. In almost all cases, the limit of detection was reached within the 20 minute contact time with acetic acid, the exception being S.aureus, where some colonies could still be detected.

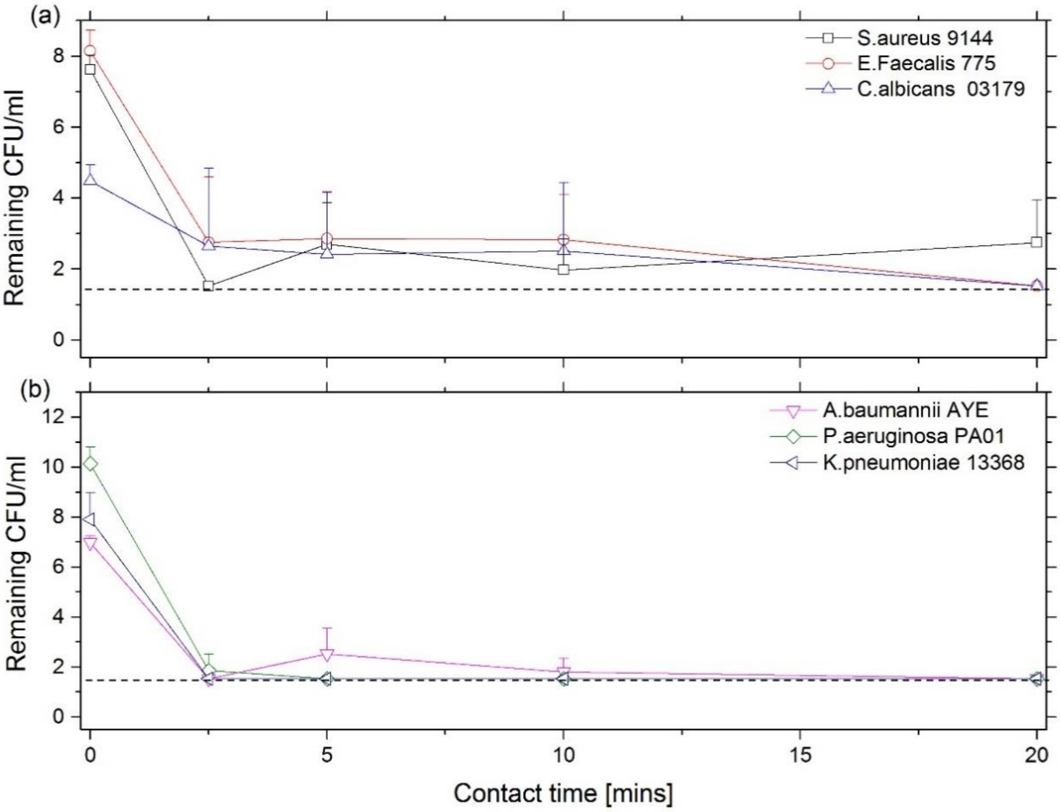

Figure 55: Log reductions of investigated strains CFU/ml with contact times up to 20 minutes with acetic acid (pH 2.24); (a) S. aureus, E. faecalis & C. albicans (b) A. baumannii, P. aeruginosa & K. pneumoniae. Dotted line represents limit of detection.

Although acetic acid had a higher pH than the PAW-30 & nitric acid used in this investigation (*i.e.* it was the least acidic) it had the highest antimicrobial efficacy. This suggests that pH is not the only factor when it comes to antimicrobial efficacy and that the nature of the active species present in the fluid being used to treat the microbes plays a significant role.

8.3.8 Bactericidal efficacy of plasma treated buffer solution

The pH of sodium phosphate buffer solution only decreased to 6.17 after 30 minutes of plasma treatment. Figure 56 shows the inactivation results for each bacterial strain in contact with the plasma treated buffer solution. No reduction was observed in CFU regardless of contact time.

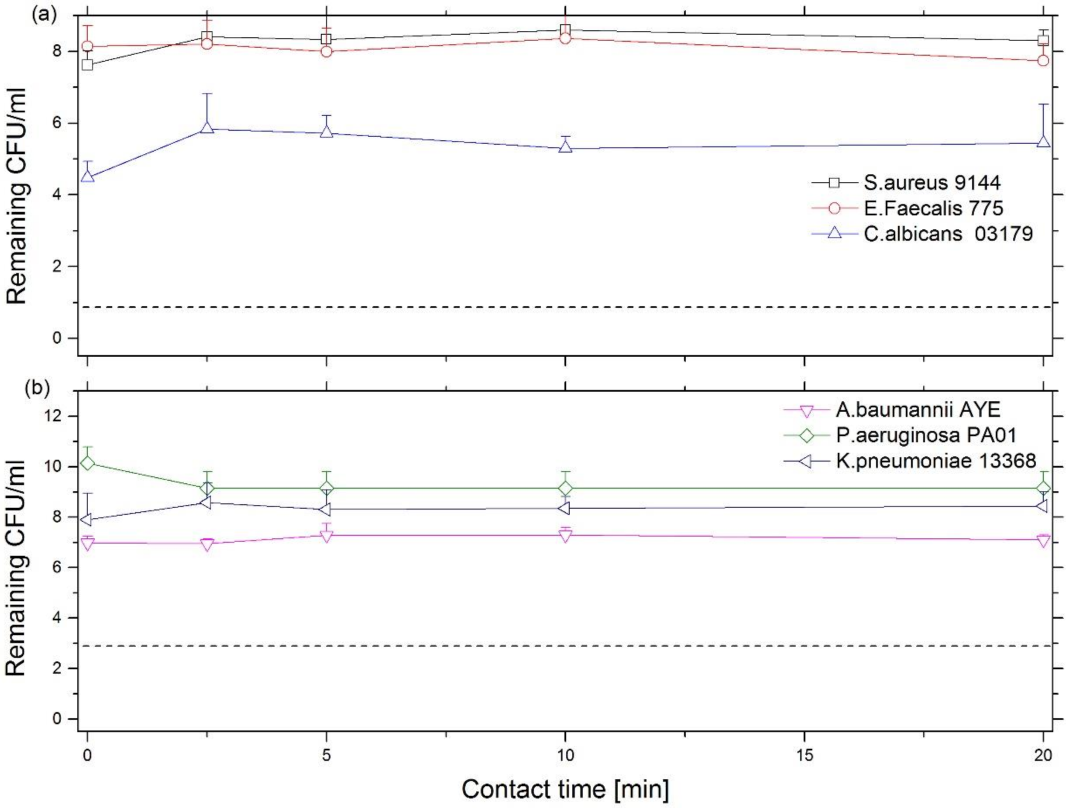

Figure 56: Log reductions of investigated strains CFU/ml with contact times up to 20 minutes with 30 minute plasma treated phosphate buffer solution (pH 6.17); (a) S. aureus, E. faecalis & C. albicans (b) A. baumannii, P. aeruginosa & K. pneumoniae. Dotted line represents limit of detection.

8.3.9 Mechanisms involved in bactericidal activity

Acidification of water treated by plasma is considered to be caused by an increase in the concentration of nitrate and nitrite ions which lead to the formation of nitric acid. [170] The pH of the plasma treated water has a significant impact on the species generation and the stability of several key aqueous phase species is impacted under acidic conditions. Several studies have indicated that nitrites and hydrogen peroxide can react in an acidic environment to form peroxynitrite (ONOO-) and peroxynitrous acid (ONOOH) via reactions R15 & 16. Nitrates may be formed by the degradation of peroxynitrous acid via reaction R17 and the reduction of nitrites and the subsequent oxidation of NO. [86], [170]

$$H_2O_2 + NO_2^- + \rightarrow ONOO^- + H_2O \tag{R15}$$

$$H_2O_2 + NO_2^- + H^+ + \rightarrow ONOOH + H_2O \tag{R16}$$

$$ONOOH \rightarrow H^+ + NO_3^- \tag{R17}$$

The fall in nitrite concentration observed for discharge powers >19.7W in figure 51 could potentially be explained by R15 - R17 as acidification of the water sample would occur at a higher rate presenting the environmental conditions for such reactions to occur sooner. Peroxynitrite is a desirable compound in PAW as it is known to be a strong bactericidal agent, it has the ability to cross biological membranes and cause damage to proteins, DNA and membrane phospholipids through oxidation and nitration. [171] [172] Finally, under the conditions tests the aqueous phase ozone is near a minimum 0.07 mg/L, thus O_3 alone can be regarded as having negligible influence on the antimicrobial activity observed from PAW-30.

In terms of fungal treatment, C. albicans shows resistance to both PAW and HNO_3 which may be as a result of its preference for lower pH environments as it is commonly found in the gastrointestinal tract. O'May *et al* [173] demonstrated that the highest cell counts recovered for C. albicans as planktonic populations was at pH 4, and at pH 3 for biofilm populations.

8.4 Conclusions

This chapter investigated the application of an optimised SBD for the decontamination of clinically relevant human pathogens via the application of an activated liquid. The findings confirm that acidification of water when plasma treated may play a role in the microbial kill efficacy of PAW. Notably, PAW created using at a 30 minute plasma treatment at a discharge power of 19.7 W was shown to have higher antimicrobial efficacy against gram-negative than gram-positive bacteria for the contact times used in the investigation. This is in agreement with other publications were gram-negative bacteria are seen to be more susceptible to a non-thermal plasma treatment than gram-positive bacteria. [112], [174], [175]

The results obtained from tests with acids with a similar pH value to PAW-30 gave variable results. Nitric acid alone had little effect against all the gram-negative strains in comparison to PAW, although it did produce similar results in the CFU reduction of *P.aeruginosa*. This observation suggests that the pH of PAW and any nitric acid it may contain cannot be solely responsible for the microbial kill seen from the PAW treatment. The formation of other species such as peroxynitrite/peroxynitrous acid in the acidic environment may be contributing factors to the bactericidal activity seen from plasma activated water.

It was established that acetic acid gave the highest antimicrobial efficacy despite being the least acidic. This reinforces the conclusion that the composition of the fluid being used to treat the microorganisms is therefore an important factor when it comes to its antimicrobial efficacy. Sodium Phosphate buffer treated with plasma for 30 minutes was shown to have negligible antimicrobial effects, indicating that the pH plays a key role in the antimicrobial action of PAW by influencing reaction pathways in the bulk phase fluid. Hydrogen peroxide (H_2O_2) was initially measured but was found in such small concentrations that it was deemed negligible to the microbial kill seen from PAW, thus was not used as an acid for comparison.

The results shown in this chapter demonstrate the potential of PAW as an antimicrobial agent and provides an insight into the chemical species and pathways underpinning the observed decontamination effects. These findings are important as the susceptibilities of different pathogens to PAW were also obtained, thus enabling the optimised generation of PAW in applications that require targeting specific pathogenic microorganisms.

Chapter 8: Conclusions and future outlook

This thesis has focused on the surface barrier discharge and has explored the link between the plasma power source, the plasma generated species, the downstream transport of reactive species and their impact on biological substrates. In doing so the main objective has been satisfied and the challenges associated with generating controlled doses of specific reactive species to elicit a specific biological response have been addressed.

It was shown that design of the electrodes in a SBD have a major influence on key parameters such as the breakdown voltage, deposited power and velocity magnitude of the plasma induced flow. It was demonstrated that reducing the diameter of the discharge gap below 5 mm caused the breakdown voltage to increase exponentially while the power deposited within the discharge was reduced. These observations were attributed to a reduction in the electric field across the discharge gap with decreasing diameter. These findings have significant implications for the development of large are uniform surface barrier discharge arrays, considering the composition of the gas phase reactive species of non-thermal discharges are directly influenced by the power deposition. Thus, a compromise between the discharge area of the individual SBD's and the applied voltage required to achieve a desired discharge chemistry must be made. This is especially important in the development of SBDs for applications in decontamination which often require significant densities of specific RNS. Any increase in the breakdown voltage makes the transition from ROS to RNS dominant chemistries more difficult as the magnitude of the applied voltage to achieve these chemistries is also increased.

Changing the geometry of the electrode was also found to affect the electrohydrodynamic (EHD) forces created by the plasma. Reducing the diameter of a circular discharge gap caused the velocity magnitude of the EHD induced flow to drop at a constant operating power. Particle imaging velocimetry measurements were used to show that the transport of reactive species downstream of the plasma discharge is heavily impeded by the reduction of the discharge gap, hence the design of a SBD for an application that relies on the transport of shorter-lived species requires careful consideration. Although the findings related to geometry focused on circular electrode arrangements, it is highly likely that the underpinning physical mechanisms involved apply to all surface barrier discharge configurations, including those employing other electrode geometries under different environmental gas compositions such as oxygen, carbon dioxide, argon and helium.

In an effort to be able to control the composition of the plasma generated RONS the impact of varying the surface temperature of the dielectric in an enclosed SBD operating under different dissipated power conditions was assessed. For the first time, it was demonstrated that the dielectric temperature plays a major role in ozone poisoning. Through gradual heating of the dielectric surface the transition from ROS to RNS could be achieved under operating discharge powers that ozone poisoning would otherwise not occur. Using the technique developed in chapter 5 it was possible to inhibit ozone poisoning whilst operating at high plasma power conditions. Furthermore, it was shown that the gas phase chemistry can be modulated simply by modulating the dielectric temperature. Such that higher densities of long-lived ROS or RNS could be obtained simply via the cooling or heating of the dielectric surface respectively.

The findings in chapter 5 offer considerable promise for any application that requires the composition of plasma generated RONS to be tailored to achieve optimum performance. In addition, the technique can be used to mitigate against potentially undesirable species (e.g. NO_2) enabling SBD's to be used in applications where they were once considered unsuitable due to the generation of harmful long-lived species.

To ascertain the generation and transportation characteristics of short-lived species downstream of the active plasma region of a SBD in open space, advanced measurement techniques were used and an insight to spatio-temporal evolution of RNS applicable to microbial decontamination was gained. The main method of transport of plasma generated species was confirmed to be via convection arising from the plasma induced flow. NO was observed to be generated in the visible plasma domain near the electrode-dialectic interface and carried by the EHD induced flow several cm downstream of the discharge gap. An increase in the discharge power was shown to give rise to an increase in the density of NO. A computational model confirmed by the experiment measurements provided an insight into the generation and transportation of other key RNS.

The inherent limitations in the distance between the discharge domain and downstream target were demonstrated. For applications that require specific doses of key RNS to be transported to a remote location, these findings are of specific importance as they provide valuable information on the separation distances required between the discharge and target domain.

Control over the mass transport direction of plasma generated species from a SBD enables coverage of species over a greater surface area, a factor which is highly beneficial when large area surface treatments are required. Manipulation of the EHD induced flow was demonstrated through imparting a phase difference to the HV signals applied between a parallel linear electrode configuration. Allowing for the convective flow of species from the discharge domain to be steered by $\pm 60^{o}$ to the normal of the dielectric surface. Furthermore, this technique holds advantages over previous reported methods of flow manipulation as it was demonstrated to have little impact on the generation of long-lived reactive chemistries.

Thus, through simple means, the technique defined in chapter 7 paves the way in the future development of SBDs for applications that require targeted delivery of RONS without any impact on performance. In the context of applications in decontamination, this is of great importance as the chemistries accessed under different operational powers can lead to different biological responses in microorganisms.

Applications in decontamination were addressed through the subjection of pathogenic microorganisms to deionised water pre-exposed to the discharge from a SBD. The role of pH in microbial inactivation was assessed through comparison of the reductions in colony forming units obtained from PAW treatment to other fluids possessing similar pH characteristics. The findings suggest that pH alone is not responsible for the bactericidal effects observed. Other mechanisms were demonstrated to be responsible for the decontamination ability of PAW. Through liquid diagnostic techniques the composition of the liquid media post plasma treatment was analysed, leading to insight into the possible bactericidal reactive species and the chemical pathways that lead to their generation.

Further investigations in the field of healthcare are continually being performed into the application of PAW as a potential alternative to other decontamination agents which are usually toxic and environmentally damaging. These findings bring forward a more comprehensive understanding of the underpinning mechanisms involved in the decontamination effects displayed by PAW. Thus, enabling the composition of PAW to be tailored to elicit levels of necrosis in specific microorganisms.

Despite the vast amount of research into non-thermal discharges generated by SBDs and the findings presented in this thesis, due to their complex nature there still lies a number of unanswered questions. Further investigations are required to gain a more comprehensive understanding of both their physical and chemical properties and the reactions that are invoked due to the presence of certain reactive chemistries. There is still much to be learnt regarding the generation and transportation of other key reactive species generated in the gas phase and over the gas-liquid boundary from a SBD relevant to decontamination e.g. hydroxyl, peroxynitrites and peroxynitrous acids. The effects of manipulation over the EHD induced flow via phase shifting in SBD arrays is also a point for investigation as in the majority of SBD applications arrays will be necessary for large area uniform treatments. Finally, there is still yet to be a comprehensive study to be carried out on the reactive species that are responsible for microbial inactivation effects seen from plasma treated substrates such as PAW. Regardless of these unanswered questions, from the research reviewed and carried out in this work, the SBD shows great promise for future applications in the field of microbial decontamination. With the insights into the physiochemical pathways from an SBD seen in this contribution, it provides the community with a better understanding of ways to apply and bring forward this technology for decontamination applications within the healthcare sector.

Appendix A: Main model description

The plasma module solved the continuity equation, equation A.1, for the densities of electrons, N_2^+, O_2^+, O_2^- and the electron energy density.

$$\frac{\partial n_i}{\partial t} + \nabla \cdot \left(-n_i \mu_i \nabla V - D_i \nabla n_i \right) = R_i \tag{A.1}$$

In equation A.1, n_i is the density of the *i*th species (m^{-3}), μ_i is the mobility of the *i*th species ($m^2 \cdot V^{-1} \cdot s^{-1}$), V is the electric potential (V), D_i is the diffusion coefficient of the *i*th species ($m^2 \cdot s^{-1}$). The last term R_i is the rate expression of the *i*th species where all generation and loss terms are included in that term.

The plasma module also solved the Poisson equation, given by equation A.2, for the electric potential V (V) in the discharge gap and the dielectric. In addition to the equation for the evolution of the surface charge density on the plasma-dielectric interface ρ_s ($C \cdot m^{-2}$), given by equation A.3.

$$\nabla^2 V = \frac{-e}{\varepsilon_0 \varepsilon_r} \left(\sum n_+ - \sum n_- \right) \tag{A.2}$$

$$\frac{\partial \rho_s}{\partial t} = e\hat{n} \cdot \left(\sum \vec{\Gamma}_+ - \sum \vec{\Gamma}_- \right) \tag{A.3}$$

In equations A.2 and A.3, e is the electron charge (C), ε_r is the relative dielectric permittivity ($F \cdot m^{-1}$), which was assumed to be 4.7 in the dielectric and 1 in air, $\hat{n}$ is the normal unit vector on the dielectric surface. The summations $\sum n_+$ and $\sum \Gamma_+$ run over the densities and the fluxes of positively charged species respectively, identically the summations $\sum n_-$ and $\sum \Gamma_-$ run over the densities and the fluxes of negatively charged species respectively.

Considering that the plasma module was run for one period only, it was assumed that convection is ignored on this timescale, and that gas temperature was fixed at room temperature. After the module was solved, the time averaged EHD force field was exported to the reactive flow model, while the plasma power density as function of time was exported to the chemistry module.

Outputs from the plasma model are passed as inputs to the chemistry module which was based on a 0D global model following 52 species including electrons, ions, excited and neutral species involved in the set of reactions given in appendix A, for the investigation of chapter 5 or appendix B, in the case of chapter 6. The output of the plasma module showed that most of the electron-driven reactions occurred within a small area in the discharge gap next to the electrode and that the reaction rates decayed rapidly away from the small region. These findings were consistent with experimental observations showing the plasma emission, which is known to be primarily driven through electronic excitation, to be confined to a region close to the electrode edges. Based on these findings, the 0D chemistry module was used to describe the chemistry at that location. The power density at the centre of the region was extracted from the plasma module, then used as input to the chemistry module to make the simulated chemistry consistent with the physical conditions. The chemistry module solved the conservation equation for every species in the module, as given in equation A.4, in addition to an equation for the electron temperature, as given in equation A.5.

$$\frac{\partial n_i}{\partial t} = R_i - \frac{n_i \bar{u}}{d} \tag{A.4}$$

$$\frac{\partial}{\partial t}\left(\frac{3}{2}n_e T_e\right) = P_{dep} - S_{en} \tag{A.5}$$

In equations A.4 and A.5, n_i is the density of the i^{th} species, R_i is the rate expression of the i^{th} species, $\vec{u}$ is the velocity field at the point where the chemistry module is evaluated, which is calculated from the reactive flow model as described later, and d is a characteristic length of the high reactivity region where the chemistry module is defined, n_e is the electron density, T_e is the electron temperature, P_{dep} is the power deposition obtained from the plasma module, and S_{en} is the energy collisional loss computed by the chemistry module.

The chemistry module was solved for 10 periods of the applied voltage waveform, which provided sufficient time for short-lived species to obtain the expected periodic behaviour. In the final period, the effective generation or loss rates of long-lived species due to short lived species were averaged in time, then used as an input to the reactive flow model. An example of this procedure is given in the supplementary information. Since the chemistry module was dependant on the reactive flow model via the flow velocity, and the reactive flow model was dependant on the chemistry module, via generation and loss rates, the two components were solved iteratively as the reactive flow model was run.

The last and the main frame of the overall model was the reactive flow model. The reactive flow model solved for the velocity field of the gas mixture and the concentrations of only the neutral (long-lived) species in the entire computational domain. In this context, long-lived species are those that are defined as having a lifetime longer than the period of the waveform. To describe the flow, the model required the EHD force field induced by the SBD calculated by the plasma module. Equations solved in the reactive flow model are essentially

Navier-Stokes equations for the flow of the gas mixture, coupled to continuity equation for the specie followed in the reactive flow model, as given in equations A.6-A.8.

$$\frac{\partial \rho}{\partial t} + \nabla \cdot (\rho \vec{u}) = 0 \tag{A.6}$$

$$\rho \frac{\partial \vec{u}}{\partial t} + \rho \vec{u} \cdot \nabla \vec{u} = -\nabla P + \zeta \nabla^2 \vec{u} + \vec{F}_{EHD} \tag{A.7}$$

$$\frac{\partial n_i}{\partial t} + \nabla \cdot (-D_i \nabla n_i + n_i \vec{u}) = R_i \tag{A.8}$$

In equations A.6-A.8, ρ is the mass density of the species mixture (kg.m^{-3}), which was defined in terms of the individual species as $\rho = \sum_k m_k n_k$ such that m_k is the molecular mass (kg) of the *k*th species and n_k is its number density (m^{-3}), $\vec{u}$ is the velocity field (m.s^{-1}), ζ is the air's viscosity (Pa.s), P is the pressure (Pa), and $\vec{F}_{EHD}$ is the time-averaged EHD force field obtained from the plasma module, given by equation (A.9). All the parameters of equation A.8 were already defined.

$$\vec{F}_{EHD} = \frac{1}{T} \int_0^T -e\left(\sum n_{+(t)} - \sum n_{-(t)}\right) \nabla V_{(t)} dt \tag{A.9}$$

In equation (A.9), T is the period of the waveform (s), and all other parameters were previously defined. The values of the EHD force field ranged from 0 to 5 kN.m^{-3}. It should be noted that equation (A.9) implicitly implies that the momentum gained by the ions from the electric field is instantly transferred to the neutrals forming the background gas. Considering that the time between two consecutive ion-neutral collision, in the order of ~10^{-10} s, is shorter than the timescale of the simulated plasma, this assumption is well justified.

The chemical reactions among the long-lived species were treated explicitly while the chemical reactions between the long-lived and the short-lived species were treated implicitly, using effective generation and loss rates of the long-lived species due to the short-lived species, obtained from the chemistry module. The term R_i in equation A.8 thus includes both the explicit long-lived species reactions and the implicit short-lived species reactions.

It was assumed in the reactive flow model that the gas temperature was equal to room temperature. Experimental evidence showed that heating became significant after minutes of operation. Considering that the timescales investigated in this work, ranged from milliseconds to seconds, the increase in gas temperature was insignificant and thus ignored.

Appendix B: Chemistry sub-model reactions (chapter 5)

Table 7: List of reactions and the rate constants. [46]

Index	Reaction	Rate constant^a
(R1)	$e + N_2 \rightarrow N(^2D) + N + e$	$3.99 \times 10^{-17} \varepsilon^{2.24} \exp(-9.10/\varepsilon)$
(R2)	$e + N_2 \rightarrow N_2(A\,^3\Sigma) + e$	$3.34 \times 10^{-16} \varepsilon^{-0.06} \exp(-8.50/\varepsilon)$
(R3)	$e + N_2 \rightarrow N_2(B\,^3\Pi) + e$	$8.44 \times 10^{-15} \varepsilon^{-0.33} \exp(-9.15/\varepsilon)$
(R4)	$e + N_2 \rightarrow N_2^+ + e + e$	$1 \times 10^{-16} \varepsilon^{1.90} \exp(-14.6/\varepsilon)$
(R5)	$e + N \rightarrow N(^2D) + e$	$5.06 \times 10^{-15} \exp(-10.8/\varepsilon^{3.95})$
(R6)	$e + N \rightarrow N^+ + e + e$	$1.45 \times 10^{-17} \varepsilon^{2.58} \exp(-8.54/\varepsilon)$
(R7)	$e + O_2 \rightarrow O + O + e$	$2.03 \times 10^{-14} \varepsilon^{-0.10} \exp(-8.47/\varepsilon)$
(R8)	$e + O_2 \rightarrow O(^1D) + O + e$	$1.82 \times 10^{-14} \varepsilon^{-0.13} \exp(-10.7/\varepsilon)$
(R9)	$e + O_2 \rightarrow O_2(a\,^1\Delta) + e$	$1.04 \times 10^{-15} \exp(-2.59/\varepsilon)$
(R10)	$e + O_2 \rightarrow O_2^+ + e + e$	$9.54 \times 10^{-12} \varepsilon^{-1.05} \exp(-55.6/\varepsilon)$
(R11)	$e + O_3 \rightarrow O + O_2 + e$	$1.78 \times 10^{-12} \varepsilon^{-0.614} \exp(-11.5/\varepsilon)$
(R12)	$e + O \rightarrow O(^1D) + e$	$7.46 \times 10^{-15} \exp(-5.58/\varepsilon^{1.47})$
(R13)	$e + O \rightarrow O^+ + e + e$	$4.75 \times 10^{-15} \varepsilon^{0.61} \exp(-22.1/\varepsilon)$
(R14)	$e + H_2O \rightarrow H_2O^+ + e + e$	$9.65 \times 10^{-18} \varepsilon^{2.53} \exp(-8.99/\varepsilon)$
(R15)	$e + H_2O \rightarrow OH^+ + H + e + e$	$9.89 \times 10^{-12} \varepsilon^{-1.64} \exp(-67.6/\varepsilon)$
(R16)	$e + H_2O \rightarrow H^+ + OH + e + e$	$7.45 \times 10^{-15} \varepsilon^{0.34} \exp(-54.2/\varepsilon)$
(R17)	$e + H_2O \rightarrow O^+ + H_2 + e + e$	$7.4 \times 10^{-16} \varepsilon^{0.45} \exp(-55.5/\varepsilon)$
(R18)	$e + H_2O \rightarrow H_2^+ + O + e + e$	$8.49 \times 10^{-15} \varepsilon^{-1.23} \exp(-74.0/\varepsilon)$
(R19)	$e + H_2O \rightarrow OH + H + e$	$5.15 \times 10^{-15} \varepsilon^{0.62} \exp(-10.9/\varepsilon)$
(R20)	$e + H_2O \rightarrow H_2 + O(^1D) + e$	$5.19 \times 10^{-18} \varepsilon^{1.2} \exp(-13.8/\varepsilon)$
(R21)	$e + H_2 \rightarrow H + H + e$	$3.29 \times 10^{-15} \varepsilon^{0.578} \exp(-7.56/\varepsilon)$
(R22)	$e + H_2 \rightarrow H_2^+ + e + e$	$4 \times 10^{-17} \varepsilon^{2.13} \exp(-14.9/\varepsilon)$
(R23)	$e + N_2O_5 \rightarrow NO_2^+ + NO_3 + e + e$	$2.43 \times 10^{-17} \varepsilon^{2.77} \exp(-5.62/\varepsilon)$
(R24)	$e + N^+ + M \rightarrow N + M$	$3.12 \times 10^{-35} / T_e^{1.5}$
(R25)	$e + N_2^+ \rightarrow N + N$	$1.66 \times 10^{-12} / T_e^{0.7}$
(R26)	$e + N_2^+ \rightarrow N(^2D) + N$	$1.5 \times 10^{-12} / T_e^{0.7}$
(R27)	$e + N_2^+ + M \rightarrow N_2 + M$	$3.12 \times 10^{-35} / T_e^{1.5}$
(R28)	$e + N_3^+ \rightarrow N_2 + N$	$3.46 \times 10^{-12} / T_e^{0.5}$
(R29)	$e + N_4^+ \rightarrow N_2 + N_2$	$4.73 \times 10^{-11} / T_e^{0.53}$
(R30)	$e + O^+ + M \rightarrow O + M$	$3.12 \times 10^{-35} / T_e^{1.5}$
(R31)	$e + O_2^+ \rightarrow O + O$	$1.68 \times 10^{-11} / T_e^{0.7}$
(R32)	$e + O_2^+ \rightarrow O + O(^1D)$	$1.24 \times 10^{-11} / T_e^{0.7}$
(R33)	$e + O_2^+ + M \rightarrow O_2 + M$	$3.12 \times 10^{-35} / T_e^{1.5}$
(R34)	$e + O_4^+ \rightarrow O_2 + O_2$	$2.42 \times 10^{-11} / T_e^{0.5}$
(R35)	$e + N_2O^+ \rightarrow N_2 + O$	$3.46 \times 10^{-12} / T_e^{0.5}$
(R36)	$e + NO^+ \rightarrow N + O$	$1.07 \times 10^{-11} / T_e^{0.85}$
(R37)	$e + NO^+ \rightarrow N(^2D) + O$	$4.28 \times 10^{-11} / T_e^{0.85}$
(R38)	$e + NO^+ + M \rightarrow NO + M$	$3.12 \times 10^{-35} / T_e^{1.5}$
(R39)	$e + NO_2^+ \rightarrow NO + O$	$3.46 \times 10^{-12} / T_e^{0.5}$
(R40)	$e + H_2^+ \rightarrow H + H$	$1.86 \times 10^{-13} / T_e^{0.43}$
(R41)	$e + H_3^+ \rightarrow H + H_2$	$5.20 \times 10^{-11} / T_e^{0.5}$
(R42)	$e + H_3^+ \rightarrow H + H + H$	$1.14 \times 10^{-11} / T_e^{0.97}$
(R43)	$e + H_2O^+ \rightarrow OH + H$	$2.73 \times 10^{-12} / T_e^{0.5}$
(R44)	$e + H_2O^+ \rightarrow O + H_2$	$1.37 \times 10^{-12} / T_e^{0.5}$
(R45)	$e + H_2O^+ \rightarrow O + H + H$	$1.37 \times 10^{-12} / T_e^{0.5}$
(R46)	$e + H_3O^+ \rightarrow OH + H + H$	$5.46 \times 10^{-12} / T_e^{0.5}$
(R47)	$e + e + N^+ \rightarrow N + e$	$1 \times 10^{-31}\ (T_g/T_e)^{4.5}$
(R48)	$e + e + N_2^+ \rightarrow N_2 + e$	$1 \times 10^{-31}\ (T_g/T_e)^{4.5}$
(R49)	$e + e + O^+ \rightarrow O + e$	$1 \times 10^{-31}\ (T_g/T_e)^{4.5}$
(R50)	$e + e + O_2^+ \rightarrow O_2 + e$	$1 \times 10^{-31}\ (T_g/T_e)^{4.5}$
(R51)	$e + e + NO^+ \rightarrow NO + e$	$1 \times 10^{-31}\ (T_g/T_e)^{4.5}$
(R52)	$e + e + H^+ \rightarrow H + e$	$1 \times 10^{-31}\ (T_g/T_e)^{4.5}$
(R53)	$e + e + H_2^+ \rightarrow H_2 + e$	$1 \times 10^{-31}\ (T_g/T_e)^{4.5}$
(R54)	$e + e + OH^+ \rightarrow OH + e$	$1 \times 10^{-31}\ (T_g/T_e)^{4.5}$
(R55)	$e + e + H_2O^+ \rightarrow H_2O + e$	$1 \times 10^{-31}\ (T_g/T_e)^{4.5}$
(R56)	$e + O + O_2 \rightarrow O^- + O_2$	1×10^{-43}
(R57)	$e + O + O_2 \rightarrow O_2^- + O$	1×10^{-43}
(R58)	$e + O_2 + O_2 \rightarrow O_2^- + O_2$	$1.4 \times 10^{-41} T_g/T_e \exp(-600/T_g) \times \exp\{700(T_e - T_g)/(T_e T_g)\}$
(R59)	$e + O_2 + N_2 \rightarrow O_2^- + N_2$	$1.1 \times 10^{-43} (T_g/T_e)^2 \exp(-70/T_g) \times \exp\{1500(T_e - T_g)/(T_e T_g)\}$
(R60)	$e + O_2 \rightarrow O^- + O$	$2.63 \times 10^{-16} \varepsilon^{-0.495} \exp(-5.65/\varepsilon)$
(R61)	$e + O_2 \rightarrow O_2^-$	$9.72 \times 10^{-15} \varepsilon^{-1.62} \exp(-14.2/\varepsilon)$ for $\varepsilon > 1.1$ 2.78×10^{-20} for $\varepsilon < 1.1$
(R62)	$e + O_3 \rightarrow O^- + O_2$	1×10^{-17}

(R63)	$e + O_3 \rightarrow O_2^- + O$	1×10^{-15}
(R64)	$e + O_3 + M \rightarrow O_3^- + M$	1×10^{-43}
(R65)	$e + N_2O \rightarrow O^- + N_2$	2×10^{-16}
(R66)	$e + NO + M \rightarrow NO^- + M$	8×10^{-43}
(R67)	$e + NO_2 \rightarrow O^- + NO$	1×10^{-17}
(R68)	$e + NO_2 + M \rightarrow NO_2^- + M$	1.5×10^{-42}
(R69)	$e + NO_3 + M \rightarrow NO_3^- + M$	1×10^{-42}
(R70)	$e + H_2O \rightarrow H^- + OH$	$4.42 \times 10^{-14} \varepsilon^{-2.0} \exp(-13.39/\varepsilon)$
(R71)	$e + H_2O \rightarrow O^- + H_2$	$2.97 \times 10^{-15} \varepsilon^{-1.56} \exp(-13.67/\varepsilon)$
(R72)	$e + H_2O \rightarrow OH^- + H$	$9.6 \times 10^{-16} \varepsilon^{-1.70} \exp(-13.31/\varepsilon)$
(R73)	$e + HNO_3 \rightarrow NO_2^- + OH$	5×10^{-14}
(R74)	$O^- + N \rightarrow NO + e$	2.6×10^{-16}
(R75)	$O^- + N_2 \rightarrow N_2O + e$	1×10^{-18}
(R76)	$O^- + N_2(A\,^3\Sigma) \rightarrow N_2 + O + e$	2.2×10^{-15}
(R77)	$O^- + N_2(B\,^3\Pi) \rightarrow N_2 + O + e$	1.9×10^{-15}
(R78)	$O^- + O \rightarrow O_2 + e$	1.4×10^{-16}
(R79)	$O^- + O_2 \rightarrow O_3 + e$	1×10^{-18}
(R80)	$O^- + O_2(a\,^1\Delta) \rightarrow O_3 + e$	3×10^{-16}
(R81)	$O^- + O_3 \rightarrow O_2 + O_2 + e$	3×10^{-16}
(R82)	$O^- + NO \rightarrow NO_2 + e$	2.6×10^{-16}
(R83)	$O^- + H_2 \rightarrow H_2O + e$	7×10^{-16}
(R84)	$O_2^- + N \rightarrow NO_2 + e$	5×10^{-16}
(R85)	$O_2^- + N_2 \rightarrow N_2 + O_2 + e$	$1.9 \times 10^{-18} (T_g/300)^{0.5} \exp(-4990/T_g)$
(R86)	$O_2^- + N_2(A\,^3\Sigma) \rightarrow N_2 + O_2 + e$	2.1×10^{-15}
(R87)	$O_2^- + N_2(B\,^3\Pi) \rightarrow N_2 + O_2 + e$	2.5×10^{-15}
(R88)	$O_2^- + O \rightarrow O_3 + e$	1.5×10^{-16}
(R89)	$O_2^- + O_2 \rightarrow O_2 + O_2 + e$	$2.7 \times 10^{-16}\ (T_g/300)^{0.5} \exp(-5590/T_g)$
(R90)	$O_2^- + O_3 \rightarrow O_3 + O_2 + e$	6×10^{-16}
(R91)	$O_2^- + O_2(a\,^1\Delta) \rightarrow O_2 + O_2 + e$	2×10^{-16}
(R92)	$O_2^- + H \rightarrow HO_2 + e$	1.4×10^{-15}
(R93)	$O_3^- + O \rightarrow O_2 + O_2 + e$	3×10^{-16}
(R94)	$O_3^- + O_2 \rightarrow O_3 + O_2 + e$	2.3×10^{-17}
(R95)	$O_3^- + O_3 \rightarrow O_2 + O_2 + O_2 + e$	3×10^{-16}
(R96)	$NO^- + M \rightarrow NO + M + e$	2.40×10^{-19}
(R97)	$NO^- + NO \rightarrow NO + NO + e$	5×10^{-18}
(R98)	$NO^- + N_2O \rightarrow NO + N_2O + e$	5.1×10^{-18}
(R99)	$NO^- + H_2 \rightarrow NO + H_2 + e$	2.3×10^{-19}
(R100)	$NO_2^- + O \rightarrow NO_3 + e$	1×10^{-18}
(R10)1	$NO_2^- + N \rightarrow N_2 + O_2 + e$	1×10^{-18}
(R102)	$NO_3^- + O \rightarrow NO_2 + O_2 + e$	1×10^{-18}
(R103)	$NO_3^- + N \rightarrow N_2 + O_3 + e$	1×10^{-18}
(R104)	$H^- + O_2 \rightarrow HO_2 + e$	1.2×10^{-15}
(R105)	$H^- + H \rightarrow H_2 + e$	1.8×10^{-15}
(R106)	$OH^- + O \rightarrow HO_2 + e$	2×10^{-16}
(R107)	$OH^- + H \rightarrow H_2O + e$	1.8×10^{-15}
(R108)	$N^+ + N + M \rightarrow N_2^+ + M$	1×10^{-41}
(R109)	$N^+ + N_2 + M \rightarrow N_3^+ + M$	4.6×10^{-41}
(R110)	$N^+ + N_2O \rightarrow NO^+ + N_2$	5.5×10^{-16}
(R111)	$N^+ + NO \rightarrow NO^+ + N$	4.72×10^{-16}
(R112)	$N^+ + NO \rightarrow N_2^+ + O$	8.33×10^{-17}
(R113)	$N^+ + NO \rightarrow O^+ + N_2$	1×10^{-18}
(R114)	$N^+ + NO_2 \rightarrow NO_2^+ + N$	3×10^{-16}
(R115)	$N^+ + NO_2 \rightarrow NO^+ + NO$	5×10^{-16}
(R116)	$N^+ + O \rightarrow O^+ + N$	1×10^{-18}
(R117)	$N^+ + O + M \rightarrow NO^+ + M$	1×10^{-41}
(R118)	$N^+ + O_2 \rightarrow NO^+ + O$	2.7×10^{-16}
(R119)	$N^+ + O_2 \rightarrow O^+ + NO$	2.8×10^{-17}
(R120)	$N^+ + O_2 \rightarrow O_2^+ + N$	3×10^{-16}
(R121)	$N^+ + O_3 \rightarrow NO^+ + O_2$	5×10^{-16}
(R122)	$N^+ + OH \rightarrow OH^+ + N$	3.4×10^{-16}
(R123)	$N^+ + OH \rightarrow NO^+ + H$	3.4×10^{-16}
(R124)	$N^+ + H_2O \rightarrow H_2O^+ + N$	1.19×10^{-15}
(R125)	$N^+ + H_2O \rightarrow NO^+ + H_2$	2.1×10^{-16}
(R126)	$N_2^+ + N \rightarrow N^+ + N_2$	1×10^{-18}
(R127)	$N_2^+ + N + M \rightarrow N_3^+ + M$	$1 \times 10^{-41}\ (300/T_g)$

(R128)	$N_2^+ + N_2 + M \rightarrow N_4^+ + M$	$1 \times 10^{-41}\ (300/T_g)$
(R129)	$N_2^+ + N_2(A\,^3\Sigma) \rightarrow N_3^+ + N$	3×10^{-16}
(R130)	$N_2^+ + N_2O \rightarrow N_2O^+ + N_2$	6×10^{-16}
(R131)	$N_2^+ + N_2O \rightarrow NO^+ + N + N_2$	4×10^{-16}
(R132)	$N_2^+ + NO \rightarrow NO^+ + N_2$	3.9×10^{-16}
(R133)	$N_2^+ + NO_2 \rightarrow NO^+ + N_2O$	5×10^{-17}
(R134)	$N_2^+ + NO_2 \rightarrow NO_2^+ + N_2$	3×10^{-16}
(R135)	$N_2^+ + O \rightarrow NO^+ + N$	1.4×10^{-16}
(R136)	$N_2^+ + O \rightarrow NO^+ + N(^2D)$	$1.8 \times 10^{-16}\ (300/T_g)$
(R137)	$N_2^+ + O \rightarrow O^+ + N_2$	$1 \times 10^{-17}\ (300/T_g)^{0.5}$
(R138)	$N_2^+ + O_2 \rightarrow O_2^+ + N_2$	5×10^{-17}
(R139)	$N_2^+ + O_3 \rightarrow O_2^+ + O + N_2$	1×10^{-16}
(R140)	$N_2^+ + H_2O \rightarrow H_2O^+ + N_2$	2.3×10^{-15}
(R141)	$N_3^+ + N \rightarrow N_2^+ + N_2$	6.6×10^{-17}
(R142)	$N_3^+ + O_2 \rightarrow O_2^+ + N + N_2$	2.3×10^{-17}
(R143)	$N_3^+ + O_2 \rightarrow NO^+ + O + N_2$	2×10^{-17}
(R144)	$N_3^+ + O_2 \rightarrow NO_2^+ + N_2$	4.4×10^{-17}
(R145)	$N_3^+ + NO \rightarrow NO^+ + N_2 + N$	7×10^{-17}
(R146)	$N_3^+ + NO \rightarrow N_2O^+ + N_2$	7×10^{-17}
(R147)	$N_3^+ + N_2O \rightarrow NO^+ + N_2 + N_2$	5×10^{-17}
(R148)	$N_3^+ + NO_2 \rightarrow NO^+ + NO + N_2$	7×10^{-17}
(R149)	$N_3^+ + NO_2 \rightarrow NO_2^+ + N + N_2$	7×10^{-17}
(R150)	$N_4^+ + N_2 \rightarrow N_2^+ + N_2 + N_2$	$2.1 \times 10^{-16} \exp(T_g/121)$
(R151)	$N_4^+ + N_2O \rightarrow N_2O^+ + N_2 + N_2$	3×10^{-16}
(R152)	$N_4^+ + N \rightarrow N^+ + N_2 + N_2$	1×10^{-17}
(R153)	$N_4^+ + NO \rightarrow NO^+ + N_2 + N_2$	3.9×10^{-16}
(R154)	$N_4^+ + NO_2 \rightarrow NO_2^+ + N_2 + N_2$	2.5×10^{-16}
(R155)	$N_4^+ + NO_2 \rightarrow NO^+ + N_2O + N_2$	5×10^{-17}
(R156)	$N_4^+ + O \rightarrow O^+ + N_2 + N_2$	2.5×10^{-16}
(R157)	$N_4^+ + O_2 \rightarrow O_2^+ + N_2 + N_2$	2.4×10^{-16}
(R158)	$N_4^+ + H_2 \rightarrow H_2^+ + N_2 + N_2$	$3 \times 10^{-16} \exp(-1800/T_g)$
(R159)	$N_4^+ + H_2O \rightarrow H_2O^+ + N_2 + N_2$	3×10^{-15}
(R160)	$O^+ + N + M \rightarrow NO^+ + M$	1×10^{-41}
(R161)	$O^+ + N_2 + M \rightarrow NO^+ + N + M$	$6 \times 10^{-41}\ (300/T_g)^2$
(R162)	$O^+ + O + M \rightarrow O_2^+ + M$	1×10^{-41}
(R163)	$O^+ + O_2 \rightarrow O_2^+ + O$	$2.1 \times 10^{-17}\ (300/T_g)^{0.5}$
(R164)	$O^+ + O_3 \rightarrow O_2^+ + O_2$	1×10^{-16}
(R165)	$O^+ + N(^2D) \rightarrow N^+ + O$	1.3×10^{-16}
(R166)	$O^+ + NO \rightarrow NO^+ + O$	1×10^{-18}
(R167)	$O^+ + NO \rightarrow O_2^+ + N$	3×10^{-18}
(R168)	$O^+ + N_2O \rightarrow N_2O^+ + O$	6.3×10^{-16}
(R169)	$O^+ + N_2O \rightarrow NO^+ + NO$	2.3×10^{-16}
(R170)	$O^+ + N_2O \rightarrow O_2^+ + N_2$	2×10^{-17}
(R171)	$O^+ + NO_2 \rightarrow NO^+ + O_2$	5×10^{-16}
(R172)	$O^+ + NO_2 \rightarrow NO_2^+ + O$	1.6×10^{-15}
(R173)	$O^+ + H \rightarrow H^+ + O$	6.8×10^{-16}
(R174)	$O^+ + H_2 \rightarrow OH^+ + H$	1.7×10^{-15}
(R175)	$O^+ + OH \rightarrow OH^+ + O$	3.3×10^{-16}
(R176)	$O^+ + OH \rightarrow O_2^+ + H$	3.6×10^{-16}
(R177)	$O^+ + H_2O \rightarrow H_2O^+ + O$	3.2×10^{-15}
(R178)	$O_2^+ + O_2 + M \rightarrow O_4^+ + M$	$5.5 \times 10^{-43}\ (300/T_g)^{2.7}$
(R179)	$O_2^+ + N \rightarrow NO^+ + O$	1.5×10^{-16}
(R180)	$O_2^+ + N_2 \rightarrow NO^+ + NO$	1×10^{-23}
(R181)	$O_2^+ + N_2O_5 \rightarrow NO_2^+ + NO_3 + O_2$	8.8×10^{-16}
(R182)	$O_2^+ + NO \rightarrow NO^+ + O_2$	4.6×10^{-16}
(R183)	$O_2^+ + NO_2 \rightarrow NO_2^+ + O_2$	6.6×10^{-16}
(R184)	$O_2^+ + NO_2 \rightarrow NO^+ + O_3$	1×10^{-17}
(R185)	$O_4^+ + O \rightarrow O_2^+ + O_3$	3×10^{-16}
(R186)	$O_4^+ + O_2 \rightarrow O_2^+ + O_2 + O_2$	$3.3 \times 10^{-12}\ (300/T_g)^4 \exp(-5030/T_g)$
(R187)	$O_4^+ + NO \rightarrow NO^+ + O_2 + O_2$	6.80×10^{-16}
(R188)	$O_4^+ + NO_2 \rightarrow NO_2^+ + O_2 + O_2$	3×10^{-16}
(R189)	$O^- + O_2 + M \rightarrow O_3^- + M$	$1.1 \times 10^{-42}\ (300/T_g)$
(R190)	$O^- + O_2(a\,^1\Delta) \rightarrow O_2^- + O$	1×10^{-16}
(R191)	$O^- + O_3 \rightarrow O_3^- + O$	8×10^{-16}

(R192)	$O^- + N_2O \rightarrow NO^- + NO$	2×10^{-16}
(R193)	$O^- + N_2O \rightarrow N_2O^- + O$	2×10^{-18}
(R194)	$O^- + NO + M \rightarrow NO_2^- + M$	1×10^{-41}
(R195)	$O^- + NO_2 \rightarrow NO_2^- + O$	1.2×10^{-15}
(R196)	$O^- + NO_3 \rightarrow NO_3^- + O$	3×10^{-16}
(R197)	$O^- + H_2 \rightarrow OH^- + H$	3.3×10^{-17}
(R198)	$O^- + H_2O \rightarrow OH^- + OH$	1.4×10^{-15}
(R199)	$O_2^- + O \rightarrow O^- + O_2$	3.3×10^{-16}
(R200)	$O_2^- + O_2 + M \rightarrow O_4^- + M$	$3.5 \times 10^{-43}\ (300/T_g)$
(R201)	$O_2^- + O_3 \rightarrow O_3^- + O_2$	3.5×10^{-16}
(R202)	$O_2^- + N_2O \rightarrow O_3^- + N_2$	1×10^{-17}
(R203)	$O_2^- + NO_2 \rightarrow NO_2^- + O_2$	7×10^{-16}
(R204)	$O_2^- + NO_3 \rightarrow NO_3^- + O_2$	5×10^{-16}
(R205)	$O_2^- + HNO_3 \rightarrow NO_3^- + HO_2$	2.8×10^{-16}
(R206)	$O_3^- + O \rightarrow O_2^- + O_2$	1×10^{-17}
(R207)	$O_3^- + NO \rightarrow NO_2^- + O_2$	1×10^{-17}
(R208)	$O_3^- + NO \rightarrow NO_3^- + O$	1×10^{-17}
(R209)	$O_3^- + NO_2 \rightarrow NO_3^- + O_2$	2×10^{-17}
(R210)	$O_3^- + NO_2 \rightarrow NO_2^- + O_3$	7×10^{-17}
(R211)	$O_3^- + NO_3 \rightarrow NO_3^- + O_3$	5×10^{-16}
(R212)	$O_3^- + H \rightarrow OH^- + O_2$	8.4×10^{-16}
(R213)	$O_4^- + NO \rightarrow NO_3^- + O_2$	2.5×10^{-16}
(R214)	$O_4^- + O \rightarrow O^- + O_2 + O_2$	3×10^{-16}
(R215)	$O_4^- + O \rightarrow O_3^- + O_2$	4×10^{-16}
(R216)	$O_4^- + N_2 \rightarrow O_2^- + O_2 + N_2$	$1 \times 10^{-16} \exp(-1044/T_g)$
(R217)	$N_2O^+ + NO \rightarrow NO^+ + N_2O$	2.3×10^{-16}
(R218)	$N_2O^+ + N_2O \rightarrow NO^+ + NO + N_2$	1.2×10^{-17}
(R219)	$N_2O^+ + NO_2 \rightarrow NO^+ + N_2 + O_2$	4.29×10^{-16}
(R220)	$N_2O^+ + NO_2 \rightarrow NO_2^+ + N_2O$	2.21×10^{-16}
(R221)	$N_2O^+ + O_2 \rightarrow NO^+ + NO_2$	4.59×10^{-17}
(R222)	$N_2O^+ + O_2 \rightarrow O_2^+ + N_2O$	2.24×10^{-16}
(R223)	$NO^+ + N_2O_5 \rightarrow NO_2^+ + NO_2 + NO_2$	5.9×10^{-16}
(R224)	$NO^+ + O_3 \rightarrow NO_2^+ + O_2$	1×10^{-21}
(R225)	$NO^+ + N + M \rightarrow N_2O^+ + M$	$1 \times 10^{-41}\ (300/T_g)$
(R226)	$NO^- + N_2O \rightarrow NO_2^- + N_2$	2.8×10^{-20}
(R227)	$NO^- + NO_2 \rightarrow NO_2^- + NO$	3×10^{-16}
(R228)	$NO^- + NO_3 \rightarrow NO_3^- + NO$	3×10^{-16}
(R229)	$NO^- + O_2 \rightarrow O_2^- + NO$	5×10^{-16}
(R230)	$NO^- + O_3 \rightarrow O_3^- + NO$	3×10^{-16}
(R231)	$NO^- + O \rightarrow O^- + NO$	3×10^{-16}
(R232)	$NO_2^+ + NO \rightarrow NO^+ + NO_2$	2.75×10^{-16}
(R233)	$NO_2^- + N_2O_5 \rightarrow NO_3^- + NO_3 + NO$	7×10^{-16}
(R234)	$NO_2^- + NO \rightarrow NO^- + NO_2$	2.75×10^{-16}
(R235)	$NO_2^- + NO_2 \rightarrow NO_3^- + NO$	4×10^{-18}
(R236)	$NO_2^- + NO_3 \rightarrow NO_3^- + NO_2$	5×10^{-16}
(R237)	$NO_2^- + O_3 \rightarrow NO_3^- + O_2$	1.8×10^{-17}
(R238)	$NO_2^- + H \rightarrow OH^- + NO$	4×10^{-16}
(R239)	$NO_2^- + N_2O \rightarrow NO_3^- + N_2$	5×10^{-19}
(R240)	$NO_2^- + HNO_3 \rightarrow NO_3^- + HNO_2$	1.6×10^{-15}
(R241)	$NO_3^- + NO \rightarrow NO_2^- + NO_2$	3×10^{-21}
(R242)	$H^+ + O \rightarrow O^+ + H$	3.8×10^{-16}
(R243)	$H^+ + O_2 \rightarrow O_2^+ + H$	1.17×10^{-15}
(R244)	$H^+ + NO \rightarrow NO^+ + H$	1.9×10^{-15}
(R245)	$H^+ + H_2 + M \rightarrow H_3^+ + M$	3.1×10^{-41}
(R246)	$H^+ + H_2O \rightarrow H_2O^+ + H$	8.2×10^{-15}
(R247)	$H^- + N_2O \rightarrow OH^- + N_2$	1.1×10^{-15}
(R248)	$H^- + NO_2 \rightarrow NO_2^- + H$	2.9×10^{-15}
(R249)	$H^- + H_2O \rightarrow OH^- + H_2$	3.8×10^{-15}
(R250)	$H_2^+ + O_2 \rightarrow O_2^+ + H_2$	7.83×10^{-16}
(R251)	$H_2^+ + H \rightarrow H^+ + H_2$	6.4×10^{-16}
(R252)	$H_2^+ + H_2 \rightarrow H_3^+ + H$	2×10^{-15}
(R253)	$H_2^+ + H_2O \rightarrow H_3O^+ + H$	3.43×10^{-15}
(R254)	$H_2^+ + H_2O \rightarrow H_2O^+ + H_2$	3.86×10^{-15}
(R255)	$H_3^+ + O \rightarrow OH^+ + H_2$	8×10^{-16}
(R256)	$H_3^+ + H_2O \rightarrow H_3O^+ + H_2$	3×10^{-15}
(R257)	$H_3^+ + NO_2 \rightarrow NO^+ + OH + H_2$	7×10^{-16}

(R258)	$OH^+ + O_2 \rightarrow O_2^+ + OH$	5.9×10^{-16}
(R259)	$OH^+ + NO \rightarrow NO^+ + OH$	5.2×10^{-16}
(R260)	$OH^+ + NO_2 \rightarrow NO^+ + HO_2$	1.3×10^{-15}
(R261)	$OH^+ + N_2O \rightarrow N_2O^+ + OH$	2.13×10^{-16}
(R262)	$OH^+ + H_2 \rightarrow H_2O^+ + H$	9.7×10^{-16}
(R263)	$OH^+ + OH \rightarrow H_2O^+ + O$	7×10^{-16}
(R264)	$OH^+ + H_2O \rightarrow H_2O^+ + OH$	1.59×10^{-15}
(R265)	$OH^+ + H_2O \rightarrow H_3O^+ + O$	1.3×10^{-15}
(R266)	$OH^- + O_3 \rightarrow O_3^- + OH$	9×10^{-16}
(R267)	$OH^- + NO_2 \rightarrow NO_2^- + OH$	1.9×10^{-15}
(R268)	$H_2O^+ + N \rightarrow NO^+ + H_2$	1.9×10^{-16}
(R269)	$H_2O^+ + O \rightarrow O_2^+ + H_2$	5.5×10^{-17}
(R270)	$H_2O^+ + O_2 \rightarrow O_2^+ + H_2O$	4.3×10^{-16}
(R271)	$H_2O^+ + NO \rightarrow NO^+ + H_2O$	4.6×10^{-16}
(R272)	$H_2O^+ + NO_2 \rightarrow NO_2^+ + H_2O$	1.2×10^{-15}
(R273)	$H_2O^+ + H_2 \rightarrow H_3O^+ + H$	7.6×10^{-16}
(R274)	$H_2O^+ + H_2O \rightarrow H_3O^+ + OH$	1.7×10^{-15}
(R275)	$H_3O^+ + NO \rightarrow NO^+ + H + H_2O$	1.5×10^{-18}
(R276)	$H_3O^+ + N_2O_5 \rightarrow NO_2^+ + HNO_3 + H_2O$	5.5×10^{-16}
(R277)	$O^+ + O^- \rightarrow O + O$	$2 \times 10^{-13}\ (300/T_g)^{0.5}$
(R278)	$O^+ + O_2^- \rightarrow O_2 + O$	$2 \times 10^{-13}\ (300/T_g)^{0.5}$
(R279)	$O^+ + O_3^- \rightarrow O_3 + O$	$2 \times 10^{-13}\ (300/T_g)^{0.5}$
(R280)	$O^+ + O_4^- \rightarrow O_2 + O_2 + O$	1×10^{-13}
(R281)	$O^+ + N_2O^- \rightarrow N_2O + O$	$2 \times 10^{-13}\ (300/T_g)^{0.5}$
(R282)	$O^+ + NO^- \rightarrow NO + O$	$2 \times 10^{-13}\ (300/T_g)^{0.5}$
(R283)	$O^+ + NO_2^- \rightarrow NO_2 + O$	$2 \times 10^{-13}\ (300/T_g)^{0.5}$
(R284)	$O^+ + NO_3^- \rightarrow NO_3 + O$	$2 \times 10^{-13}\ (300/T_g)^{0.5}$
(R285)	$O^+ + H^- \rightarrow O + H$	$2 \times 10^{-13}\ (300/T_g)^{0.5}$
(R286)	$O^+ + OH^- \rightarrow O + OH$	$2 \times 10^{-13}\ (300/T_g)^{0.5}$
(R287)	$O_2^+ + O^- \rightarrow O + O + O$	1×10^{-13}
(R288)	$O_2^+ + O^- \rightarrow O + O_2$	$2 \times 10^{-13}\ (300/T_g)^{0.5}$
(R289)	$O_2^+ + O_2^- \rightarrow O_2 + O_2$	$2 \times 10^{-13}\ (300/T_g)^{0.5}$
(R290)	$O_2^+ + O_2^- \rightarrow O_2 + O + O$	1×10^{-13}
(R291)	$O_2^+ + O_3^- \rightarrow O_3 + O_2$	$2 \times 10^{-13}\ (300/T_g)^{0.5}$
(R292)	$O_2^+ + O_3^- \rightarrow O_3 + O + O$	1×10^{-13}
(R293)	$O_2^+ + O_4^- \rightarrow O_2 + O_2 + O_2$	1×10^{-13}
(R294)	$O_2^+ + N_2O^- \rightarrow N_2O + O_2$	$2 \times 10^{-13}\ (300/T_g)^{0.5}$
(R295)	$O_2^+ + N_2O^- \rightarrow N_2O + O + O$	1×10^{-13}
(R296)	$O_2^+ + NO^- \rightarrow NO + O_2$	$2 \times 10^{-13}\ (300/T_g)^{0.5}$
(R297)	$O_2^+ + NO^- \rightarrow NO + O + O$	1×10^{-13}
(R298)	$O_2^+ + NO_2^- \rightarrow NO_2 + O_2$	$2 \times 10^{-13}\ (300/T_g)^{0.5}$
(R299)	$O_2^+ + NO_2^- \rightarrow NO_2 + O + O$	1×10^{-13}
(R300)	$O_2^+ + NO_3^- \rightarrow NO_3 + O_2$	$2 \times 10^{-13}\ (300/T_g)^{0.5}$
(R301)	$O_2^+ + NO_3^- \rightarrow NO_3 + O + O$	1×10^{-13}
(R302)	$O_2^+ + H^- \rightarrow H + O_2$	$2 \times 10^{-13}\ (300/T_g)^{0.5}$
(R303)	$O_2^+ + H^- \rightarrow H + O + O$	1×10^{-13}
(R304)	$O_2^+ + OH^- \rightarrow OH + O_2$	$2 \times 10^{-13}\ (300/T_g)^{0.5}$
(R305)	$O_2^+ + OH^- \rightarrow OH + O + O$	1×10^{-13}
(R306)	$O_4^+ + O^- \rightarrow O + O_2 + O_2$	1×10^{-13}
(R307)	$O_4^+ + O_2^- \rightarrow O_2 + O_2 + O_2$	1×10^{-13}
(R308)	$O_4^+ + O_3^- \rightarrow O_3 + O_2 + O_2$	1×10^{-13}
(R309)	$O_4^+ + O_4^- \rightarrow O_2 + O_2 + O_2 + O_2$	1×10^{-13}
(R310)	$O_4^+ + N_2O^- \rightarrow N_2O + O_2 + O_2$	1×10^{-13}
(R311)	$O_4^+ + NO^- \rightarrow NO + O_2 + O_2$	1×10^{-13}
(R312)	$O_4^+ + NO_2^- \rightarrow NO_2 + O_2 + O_2$	1×10^{-13}
(R313)	$O_4^+ + NO_3^- \rightarrow NO_3 + O_2 + O_2$	1×10^{-13}
(R314)	$O_4^+ + H^- \rightarrow H + O_2 + O_2$	1×10^{-13}
(R315)	$O_4^+ + OH^- \rightarrow OH + O_2 + O_2$	1×10^{-13}
(R316)	$N^+ + N_2O^- \rightarrow N_2O + N$	$2 \times 10^{-13}\ (300/T_g)^{0.5}$
(R317)	$N^+ + NO^- \rightarrow NO + N$	$2 \times 10^{-13}\ (300/T_g)^{0.5}$
(R318)	$N^+ + NO_2^- \rightarrow NO_2 + N$	$2 \times 10^{-13}\ (300/T_g)^{0.5}$
(R319)	$N^+ + NO_3^- \rightarrow NO_3 + N$	$2 \times 10^{-13}\ (300/T_g)^{0.5}$
(R320)	$N^+ + O^- \rightarrow O + N$	$2 \times 10^{-13}\ (300/T_g)^{0.5}$

(R321)	$N^+ + O_2^- \rightarrow O_2 + N$	$2 \times 10^{-13}\ (300/T_g)^{0.5}$
(R322)	$N^+ + O_3^- \rightarrow O_3 + N$	$2 \times 10^{-13}\ (300/T_g)^{0.5}$
(R323)	$N^+ + O_4^- \rightarrow O_2 + O_2 + N$	1×10^{-13}
(R324)	$N^+ + H^- \rightarrow N + H$	$2 \times 10^{-13}\ (300/T_g)^{0.5}$
(R325)	$N^+ + OH^- \rightarrow N + OH$	$2 \times 10^{-13}\ (300/T_g)^{0.5}$
(R326)	$N_2^+ + N_2O^- \rightarrow N_2O + N_2$	$2 \times 10^{-13}\ (300/T_g)^{0.5}$
(R327)	$N_2^+ + N_2O^- \rightarrow N_2O + N + N$	1×10^{-13}
(R328)	$N_2^+ + NO^- \rightarrow NO + N_2$	$2 \times 10^{-13}\ (300/T_g)^{0.5}$
(R329)	$N_2^+ + NO^- \rightarrow NO + N + N$	1×10^{-13}
(R330)	$N_2^+ + NO_2^- \rightarrow NO_2 + N_2$	$2 \times 10^{-13}\ (300/T_g)^{0.5}$
(R331)	$N_2^+ + NO_2^- \rightarrow NO_2 + N + N$	1×10^{-13}
(R332)	$N_2^+ + NO_3^- \rightarrow NO_3 + N_2$	$2 \times 10^{-13}\ (300/T_g)^{0.5}$
(R333)	$N_2^+ + NO_3^- \rightarrow NO_3 + N + N$	1×10^{-13}
(R334)	$N_2^+ + O^- \rightarrow O + N + N$	1×10^{-13}
(R335)	$N_2^+ + O^- \rightarrow O + N_2$	$2 \times 10^{-13}\ (300/T_g)^{0.5}$
(R336)	$N_2^+ + O_2^- \rightarrow O_2 + N + N$	1×10^{-13}
(R337)	$N_2^+ + O_2^- \rightarrow O_2 + N_2$	$2 \times 10^{-13}\ (300/T_g)^{0.5}$
(R338)	$N_2^+ + O_3^- \rightarrow O_3 + N + N$	1×10^{-13}
(R339)	$N_2^+ + O_3^- \rightarrow O_3 + N_2$	$2 \times 10^{-13}\ (300/T_g)^{0.5}$
(R340)	$N_2^+ + O_4^- \rightarrow O_2 + O_2 + N_2$	1×10^{-13}
(R341)	$N_2^+ + H^- \rightarrow H + N_2$	$2 \times 10^{-13}\ (300/T_g)^{0.5}$
(R342)	$N_2^+ + H^- \rightarrow H + N + N$	1×10^{-13}
(R343)	$N_2^+ + OH^- \rightarrow OH + N_2$	$2 \times 10^{-13}\ (300/T_g)^{0.5}$
(R344)	$N_2^+ + OH^- \rightarrow OH + N + N$	1×10^{-13}
(R345)	$N_2O^+ + N_2O^- \rightarrow N_2O + N_2O$	$2 \times 10^{-13}\ (300/T_g)^{0.5}$
(R346)	$N_2O^+ + N_2O^- \rightarrow N_2O + N_2 + O$	1×10^{-13}
(R347)	$N_2O^+ + NO^- \rightarrow NO + N_2O$	$2 \times 10^{-13}\ (300/T_g)^{0.5}$
(R348)	$N_2O^+ + NO^- \rightarrow NO + N_2 + O$	1×10^{-13}
(R349)	$N_2O^+ + NO_2^- \rightarrow NO_2 + N_2O$	$2 \times 10^{-13}\ (300/T_g)^{0.5}$
(R350)	$N_2O^+ + NO_2^- \rightarrow NO_2 + N_2 + O$	1×10^{-13}
(R351)	$N_2O^+ + NO_3^- \rightarrow NO_3 + N_2O$	$2 \times 10^{-13}\ (300/T_g)^{0.5}$
(R352)	$N_2O^+ + NO_3^- \rightarrow NO_3 + N_2 + O$	1×10^{-13}
(R353)	$N_2O^+ + O^- \rightarrow O + N_2O$	$2 \times 10^{-13}\ (300/T_g)^{0.5}$
(R354)	$N_2O^+ + O^- \rightarrow O + N_2 + O$	1×10^{-13}
(R355)	$N_2O^+ + O_2^- \rightarrow O_2 + N_2O$	$2 \times 10^{-13}\ (300/T_g)^{0.5}$
(R356)	$N_2O^+ + O_2^- \rightarrow O_2 + N_2 + O$	1×10^{-13}
(R357)	$N_2O^+ + O_3^- \rightarrow O_3 + N_2O$	$2 \times 10^{-13}\ (300/T_g)^{0.5}$
(R358)	$N_2O^+ + O_3^- \rightarrow O_3 + N_2 + O$	1×10^{-13}
(R359)	$N_2O^+ + O_4^- \rightarrow O_2 + O_2 + N_2O$	1×10^{-13}
(R360)	$N_2O^+ + H^- \rightarrow H + N_2O$	$2 \times 10^{-13}\ (300/T_g)^{0.5}$
(R361)	$N_2O^+ + H^- \rightarrow H + N_2 + O$	1×10^{-13}
(R362)	$N_2O^+ + OH^- \rightarrow OH + N_2O$	$2 \times 10^{-13}\ (300/T_g)^{0.5}$
(R363)	$N_2O^+ + OH^- \rightarrow OH + N_2 + O$	1×10^{-13}
(R364)	$N_3^+ + N_2O^- \rightarrow N_2O + N_2 + N$	1×10^{-13}
(R365)	$N_3^+ + NO^- \rightarrow NO + N_2 + N$	1×10^{-13}
(R366)	$N_3^+ + NO_2^- \rightarrow NO_2 + N_2 + N$	1×10^{-13}
(R367)	$N_3^+ + NO_3^- \rightarrow NO_3 + N_2 + N$	1×10^{-13}
(R368)	$N_3^+ + O^- \rightarrow O + N_2 + N$	1×10^{-13}
(R369)	$N_3^+ + O_2^- \rightarrow O_2 + N_2 + N$	1×10^{-13}
(R370)	$N_3^+ + O_3^- \rightarrow O_3 + N_2 + N$	1×10^{-13}
(R371)	$N_3^+ + O_4^- \rightarrow O_2 + O_2 + N + N_2$	1×10^{-13}
(R372)	$N_3^+ + H^- \rightarrow H + N_2 + N$	1×10^{-13}
(R373)	$N_3^+ + OH^- \rightarrow OH + N_2 + N$	1×10^{-13}
(R374)	$N_4^+ + N_2O^- \rightarrow N_2O + N_2 + N_2$	1×10^{-13}
(R375)	$N_4^+ + NO^- \rightarrow NO + N_2 + N_2$	1×10^{-13}
(R376)	$N_4^+ + NO_2^- \rightarrow NO_2 + N_2 + N_2$	1×10^{-13}
(R377)	$N_4^+ + NO_3^- \rightarrow NO_3 + N_2 + N_2$	1×10^{-13}
(R378)	$N_4^+ + O^- \rightarrow O + N_2 + N_2$	1×10^{-13}
(R379)	$N_4^+ + O_2^- \rightarrow O_2 + N_2 + N_2$	1×10^{-13}
(R380)	$N_4^+ + O_3^- \rightarrow O_3 + N_2 + N_2$	1×10^{-13}
(R381)	$N_4^+ + O_4^- \rightarrow O_2 + O_2 + N_2 + N_2$	1×10^{-13}
(R382)	$N_4^+ + H^- \rightarrow H + N_2 + N_2$	1×10^{-13}
(R383)	$N_4^+ + OH^- \rightarrow OH + N_2 + N_2$	1×10^{-13}
(R384)	$NO^+ + N_2O^- \rightarrow N_2O + NO$	$2 \times 10^{-13}\ (300/T_g)^{0.5}$
(R385)	$NO^+ + N_2O^- \rightarrow N_2O + N + O$	1×10^{-13}
(R386)	$NO^+ + NO^- \rightarrow NO + NO$	$2 \times 10^{-13}\ (300/T_g)^{0.5}$

(R387)	$NO^+ + NO^- \rightarrow NO + N + O$	1×10^{-13}
(R388)	$NO^+ + NO_2^- \rightarrow NO_2 + NO$	$2 \times 10^{-13}\ (300/T_g)^{0.5}$
(R389)	$NO^+ + NO_2^- \rightarrow NO_2 + N + O$	1×10^{-13}
(R390)	$NO^+ + NO_3^- \rightarrow NO_3 + NO$	$2 \times 10^{-13}\ (300/T_g)^{0.5}$
(R391)	$NO^+ + NO_3^- \rightarrow NO_3 + N + O$	1×10^{-13}
(R392)	$NO^+ + O^- \rightarrow O + N + O$	1×10^{-13}
(R393)	$NO^+ + O^- \rightarrow O + NO$	$2 \times 10^{-13}\ (300/T_g)^{0.5}$
(R394)	$NO^+ + O_2^- \rightarrow O_2 + N + O$	1×10^{-13}
(R395)	$NO^+ + O_2^- \rightarrow O_2 + NO$	$2 \times 10^{-13}\ (300/T_g)^{0.5}$
(R396)	$NO^+ + O_3^- \rightarrow O_3 + N + O$	1×10^{-13}
(R397)	$NO^+ + O_3^- \rightarrow O_3 + NO$	$2 \times 10^{-13}\ (300/T_g)^{0.5}$
(R398)	$NO^+ + O_4^- \rightarrow O_2 + O_2 + NO$	1×10^{-13}
(R399)	$NO^+ + H^- \rightarrow H + NO$	$2 \times 10^{-13}\ (300/T_g)^{0.5}$
(R400)	$NO^+ + H^- \rightarrow H + N + O$	1×10^{-13}
(R401)	$NO^+ + OH^- \rightarrow OH + NO$	$2 \times 10^{-13}\ (300/T_g)^{0.5}$
(R402)	$NO^+ + OH^- \rightarrow OH + N + O$	1×10^{-13}
(R403)	$NO_2^+ + N_2O^- \rightarrow N_2O + NO_2$	$2 \times 10^{-13}\ (300/T_g)^{0.5}$
(R404)	$NO_2^+ + N_2O^- \rightarrow N_2O + N + O_2$	1×10^{-13}
(R405)	$NO_2^+ + NO^- \rightarrow NO + NO_2$	$2 \times 10^{-13}\ (300/T_g)^{0.5}$
(R406)	$NO_2^+ + NO^- \rightarrow NO + N + O_2$	1×10^{-13}
(R407)	$NO_2^+ + NO_2^- \rightarrow NO_2 + NO_2$	$2 \times 10^{-13}\ (300/T_g)^{0.5}$
(R408)	$NO_2^+ + NO_2^- \rightarrow NO_2 + N + O_2$	1×10^{-13}
(R409)	$NO_2^+ + NO_3^- \rightarrow NO_3 + NO_2$	$2 \times 10^{-13}\ (300/T_g)^{0.5}$
(R410)	$NO_2^+ + NO_3^- \rightarrow NO_3 + N + O_2$	1×10^{-13}
(R411)	$NO_2^+ + O^- \rightarrow O + NO_2$	$2 \times 10^{-13}\ (300/T_g)^{0.5}$
(R412)	$NO_2^+ + O^- \rightarrow O + N + O_2$	1×10^{-13}
(R413)	$NO_2^+ + O_2^- \rightarrow O_2 + NO_2$	$2 \times 10^{-13}\ (300/T_g)^{0.5}$
(R414)	$NO_2^+ + O_2^- \rightarrow O_2 + N + O_2$	1×10^{-13}
(R415)	$NO_2^+ + O_3^- \rightarrow O_3 + NO_2$	$2 \times 10^{-13}\ (300/T_g)^{0.5}$
(R416)	$NO_2^+ + O_3^- \rightarrow O_3 + N + O_2$	1×10^{-13}
(R417)	$NO_2^+ + O_4^- \rightarrow O_2 + O_2 + NO_2$	1×10^{-13}
(R418)	$NO_2^+ + H^- \rightarrow H + NO_2$	$2 \times 10^{-13}\ (300/T_g)^{0.5}$
(R419)	$NO_2^+ + H^- \rightarrow H + N + O_2$	1×10^{-13}
(R420)	$NO_2^+ + OH^- \rightarrow OH + NO_2$	$2 \times 10^{-13}\ (300/T_g)^{0.5}$
(R421)	$NO_2^+ + OH^- \rightarrow OH + N + O_2$	1×10^{-13}
(R422)	$H^+ + N_2O^- \rightarrow N_2O + H$	$2 \times 10^{-13}\ (300/T_g)^{0.5}$
(R423)	$H^+ + NO^- \rightarrow NO + H$	$2 \times 10^{-13}\ (300/T_g)^{0.5}$
(R424)	$H^+ + NO_2^- \rightarrow NO_2 + H$	$2 \times 10^{-13}\ (300/T_g)^{0.5}$
(R425)	$H^+ + NO_3^- \rightarrow NO_3 + H$	$2 \times 10^{-13}\ (300/T_g)^{0.5}$
(R426)	$H^+ + O^- \rightarrow O + H$	$2 \times 10^{-13}\ (300/T_g)^{0.5}$
(R427)	$H^+ + O_2^- \rightarrow O_2 + H$	$2 \times 10^{-13}\ (300/T_g)^{0.5}$
(R428)	$H^+ + O_3^- \rightarrow O_3 + H$	$2 \times 10^{-13}\ (300/T_g)^{0.5}$
(R429)	$H^+ + O_4^- \rightarrow O_2 + O_2 + H$	1×10^{-13}
(R430)	$H^+ + H^- \rightarrow H + H$	$2 \times 10^{-13}\ (300/T_g)^{0.5}$
(R431)	$H^+ + OH^- \rightarrow OH + H$	$2 \times 10^{-13}\ (300/T_g)^{0.5}$
(R432)	$H_2^+ + N_2O^- \rightarrow N_2O + H_2$	$2 \times 10^{-13}\ (300/T_g)^{0.5}$
(R433)	$H_2^+ + N_2O^- \rightarrow N_2O + H + H$	1×10^{-13}
(R434)	$H_2^+ + NO^- \rightarrow NO + H_2$	$2 \times 10^{-13}\ (300/T_g)^{0.5}$
(R435)	$H_2^+ + NO^- \rightarrow NO + H + H$	1×10^{-13}
(R436)	$H_2^+ + NO_2^- \rightarrow NO_2 + H_2$	$2 \times 10^{-13}\ (300/T_g)^{0.5}$
(R437)	$H_2^+ + NO_2^- \rightarrow NO_2 + H + H$	1×10^{-13}
(R438)	$H_2^+ + NO_3^- \rightarrow NO_3 + H_2$	$2 \times 10^{-13}\ (300/T_g)^{0.5}$
(R439)	$H_2^+ + NO_3^- \rightarrow NO_3 + H + H$	1×10^{-13}
(R440)	$H_2^+ + O^- \rightarrow O + H + H$	1×10^{-13}
(R441)	$H_2^+ + O^- \rightarrow O + H_2$	$2 \times 10^{-13}\ (300/T_g)^{0.5}$
(R442)	$H_2^+ + O_2^- \rightarrow O_2 + H + H$	1×10^{-13}
(R443)	$H_2^+ + O_2^- \rightarrow O_2 + H_2$	$2 \times 10^{-13}\ (300/T_g)^{0.5}$
(R444)	$H_2^+ + O_3^- \rightarrow O_3 + H + H$	1×10^{-13}
(R445)	$H_2^+ + O_3^- \rightarrow O_3 + H_2$	$2 \times 10^{-13}\ (300/T_g)^{0.5}$
(R446)	$H_2^+ + O_4^- \rightarrow O_2 + O_2 + H_2$	1×10^{-13}
(R447)	$H_2^+ + H^- \rightarrow H + H_2$	$2 \times 10^{-13}\ (300/T_g)^{0.5}$
(R448)	$H_2^+ + H^- \rightarrow H + H + H$	1×10^{-13}
(R449)	$H_2^+ + OH^- \rightarrow OH + H_2$	$2 \times 10^{-13}\ (300/T_g)^{0.5}$

(R450)	$H_2^+ + OH^- \rightarrow OH + H + H$	1×10^{-13}
(R451)	$H_3^+ + N_2O^- \rightarrow N_2O + H + H_2$	1×10^{-13}
(R452)	$H_3^+ + NO^- \rightarrow NO + H + H_2$	1×10^{-13}
(R453)	$H_3^+ + NO_2^- \rightarrow NO_2 + H + H_2$	1×10^{-13}
(R454)	$H_3^+ + NO_3^- \rightarrow NO_3 + H + H_2$	1×10^{-13}
(R455)	$H_3^+ + O^- \rightarrow O + H + H_2$	1×10^{-13}
(R456)	$H_3^+ + O_2^- \rightarrow O_2 + H + H_2$	1×10^{-13}
(R457)	$H_3^+ + O_3^- \rightarrow O_3 + H + H_2$	1×10^{-13}
(R458)	$H_3^+ + O_4^- \rightarrow O_2 + O_2 + H + H_2$	1×10^{-13}
(R459)	$H_3^+ + H^- \rightarrow H + H + H_2$	1×10^{-13}
(R460)	$H_3^+ + OH^- \rightarrow OH + H + H_2$	1×10^{-13}
(R461)	$OH^+ + N_2O^- \rightarrow N_2O + OH$	$2 \times 10^{-13}\ (300/T_g)^{0.5}$
(R462)	$OH^+ + N_2O^- \rightarrow N_2O + O + H$	1×10^{-13}
(R463)	$OH^+ + NO^- \rightarrow NO + OH$	$2 \times 10^{-13}\ (300/T_g)^{0.5}$
(R464)	$OH^+ + NO^- \rightarrow NO + O + H$	1×10^{-13}
(R465)	$OH^+ + NO_2^- \rightarrow NO_2 + OH$	$2 \times 10^{-13}\ (300/T_g)^{0.5}$
(R466)	$OH^+ + NO_2^- \rightarrow NO_2 + O + H$	1×10^{-13}
(R467)	$OH^+ + NO_3^- \rightarrow NO_3 + OH$	$2 \times 10^{-13}\ (300/T_g)^{0.5}$
(R468)	$OH^+ + NO_3^- \rightarrow NO_3 + O + H$	1×10^{-13}
(R469)	$OH^+ + O^- \rightarrow O + O + H$	1×10^{-13}
(R470)	$OH^+ + O^- \rightarrow O + OH$	$2 \times 10^{-13}\ (300/T_g)^{0.5}$
(R471)	$OH^+ + O_2^- \rightarrow O_2 + O + H$	1×10^{-13}
(R472)	$OH^+ + O_2^- \rightarrow O_2 + OH$	$2 \times 10^{-13}\ (300/T_g)^{0.5}$
(R473)	$OH^+ + O_3^- \rightarrow O_3 + O + H$	1×10^{-13}
(R474)	$OH^+ + O_3^- \rightarrow O_3 + OH$	$2 \times 10^{-13}\ (300/T_g)^{0.5}$
(R475)	$OH^+ + O_4^- \rightarrow O_2 + O_2 + OH$	1×10^{-13}
(R476)	$OH^+ + H^- \rightarrow H + OH$	$2 \times 10^{-13}\ (300/T_g)^{0.5}$
(R477)	$OH^+ + H^- \rightarrow H + O + H$	1×10^{-13}
(R478)	$OH^+ + OH^- \rightarrow OH + OH$	$2 \times 10^{-13}\ (300/T_g)^{0.5}$
(R479)	$OH^+ + OH^- \rightarrow OH + O + H$	1×10^{-13}
(R480)	$H_2O^+ + N_2O^- \rightarrow N_2O + H_2O$	$2 \times 10^{-13}\ (300/T_g)^{0.5}$
(R481)	$H_2O^+ + N_2O^- \rightarrow N_2O + OH + H$	1×10^{-13}
(R482)	$H_2O^+ + NO^- \rightarrow NO + H_2O$	$2 \times 10^{-13}\ (300/T_g)^{0.5}$
(R483)	$H_2O^+ + NO^- \rightarrow NO + OH + H$	1×10^{-13}
(R484)	$H_2O^+ + NO_2^- \rightarrow NO_2 + H_2O$	$2 \times 10^{-13}\ (300/T_g)^{0.5}$
(R485)	$H_2O^+ + NO_2^- \rightarrow NO_2 + OH + H$	1×10^{-13}
(R486)	$H_2O^+ + NO_3^- \rightarrow NO_3 + H_2O$	$2 \times 10^{-13}\ (300/T_g)^{0.5}$
(R487)	$H_2O^+ + NO_3^- \rightarrow NO_3 + OH + H$	1×10^{-13}
(R488)	$H_2O^+ + O^- \rightarrow O + OH + H$	1×10^{-13}
(R489)	$H_2O^+ + O^- \rightarrow O + H_2O$	$2 \times 10^{-13}\ (300/T_g)^{0.5}$
(R490)	$H_2O^+ + O_2^- \rightarrow O_2 + OH + H$	1×10^{-13}
(R491)	$H_2O^+ + O_2^- \rightarrow O_2 + H_2O$	$2 \times 10^{-13}\ (300/T_g)^{0.5}$
(R492)	$H_2O^+ + O_3^- \rightarrow O_3 + OH + H$	1×10^{-13}
(R493)	$H_2O^+ + O_3^- \rightarrow O_3 + H_2O$	$2 \times 10^{-13}\ (300/T_g)^{0.5}$
(R494)	$H_2O^+ + O_4^- \rightarrow O_2 + O_2 + H_2O$	1×10^{-13}
(R495)	$H_2O^+ + H^- \rightarrow H + H_2O$	$2 \times 10^{-13}\ (300/T_g)^{0.5}$
(R496)	$H_2O^+ + H^- \rightarrow H + OH + H$	1×10^{-13}
(R497)	$H_2O^+ + OH^- \rightarrow OH + H_2O$	$2 \times 10^{-13}\ (300/T_g)^{0.5}$
(R498)	$H_2O^+ + OH^- \rightarrow OH + OH + H$	1×10^{-13}
(R499)	$H_3O^+ + N_2O^- \rightarrow N_2O + H_2O + H$	1×10^{-13}
(R500)	$H_3O^+ + NO^- \rightarrow NO + H_2O + H$	1×10^{-13}
(R501)	$H_3O^+ + NO_2^- \rightarrow NO_2 + H_2O + H$	1×10^{-13}
(R502)	$H_3O^+ + NO_3^- \rightarrow NO_3 + H_2O + H$	1×10^{-13}
(R503)	$H_3O^+ + O^- \rightarrow O + H_2O + H$	1×10^{-13}
(R504)	$H_3O^+ + O_2^- \rightarrow O_2 + H_2O + H$	1×10^{-13}
(R505)	$H_3O^+ + O_3^- \rightarrow O_3 + H_2O + H$	1×10^{-13}
(R506)	$H_3O^+ + O_4^- \rightarrow O_2 + O_2 + H_2O + H$	1×10^{-13}
(R507)	$H_3O^+ + H^- \rightarrow H + H_2O + H$	1×10^{-13}
(R508)	$H_3O^+ + OH^- \rightarrow OH + H_2O + H$	1×10^{-13}
(R509)	$N + N + M \rightarrow N_2 + M$	$8.3 \times 10^{-46} \exp(500/T_g)$
(R510)	$N + NO \rightarrow N_2 + O$	$2.1 \times 10^{-17} \exp(100/T_g)$
(R511)	$N + NO_2 \rightarrow N_2O + O$	$5.8 \times 10^{-18} \exp(220/T_g)$
(R512)	$N + NO_2 \rightarrow N_2 + O + O$	9.1×10^{-19}
(R513)	$N + NO_2 \rightarrow NO + NO$	6×10^{-19}
(R514)	$N + NO_2 \rightarrow N_2 + O_2$	7×10^{-19}
(R515)	$N + O + M \rightarrow NO + M$	$6.3 \times 10^{-45} \exp(140/T_g)$

(R516)	$N + O_2 \rightarrow NO + O$	$1.5 \times 10^{-17} \exp(-3600/T_g)$
(R517)	$N + O_3 \rightarrow NO + O_2$	5×10^{-22}
(R518)	$N + OH \rightarrow H + NO$	7.5×10^{-17}
(R519)	$N + HO_2 \rightarrow NO + OH$	$1.7 \times 10^{-17} \exp(-1000/T_g)$
(R520)	$N(^2D) + N_2 \rightarrow N + N_2$	$5 \times 10^{-18} \exp(-1620/T_g)$
(R521)	$N(^2D) + N_2O \rightarrow N_2 + NO$	$1.5 \times 10^{-17} \exp(-570/T_g)$
(R522)	$N(^2D) + NO \rightarrow N_2O$	6×10^{-17}
(R523)	$N(^2D) + NO \rightarrow O + N_2$	4.5×10^{-17}
(R524)	$N(^2D) + O \rightarrow N + O$	$7{\times}10^{-19}$
(R525)	$N(^2D) + O_2 \rightarrow NO + O$	$1.5 \times 10^{-18}\ (T_g/300)^{0.5}$
(R526)	$N(^2D) + O_2 \rightarrow NO + O(^1D)$	$6 \times 10^{-18}\ (T_g/300)^{0.5}$
(R527)	$N_2(A\,^3\Sigma) + N_2 \rightarrow N_2 + N_2$	2.2×10^{-20}
(R528)	$N_2(A\,^3\Sigma) + N_2(A\,^3\Sigma) \rightarrow N_2(B\,^3\Pi) + N_2$	4×10^{-16}
(R529)	$N_2(A\,^3\Sigma) + N_2O \rightarrow O + N_2 + N_2$	8×10^{-17}
(R530)	$N_2(A\,^3!\Sigma) + N_2O \rightarrow NO + N + N_2$	8×10^{-17}
(R531)	$N_2(A\,^3\Sigma) + NO_2 \rightarrow N_2 + NO + O$	1.3×10^{-17}
(R532)	$N_2(A\,^3\Sigma) + O_2 \rightarrow N_2 + O + O$	$5 \times 10^{-18} \exp(-210/T_g)$
(R533)	$N_2(A\,^3\Sigma) + O_2 \rightarrow O_2(a\,^1\Delta) + N_2$	1×10^{-18}
(R534)	$N_2(A\,^3\Sigma) + N \rightarrow N + N_2$	5×10^{-17}
(R535)	$N_2(A\,^3\Sigma) + O \rightarrow NO + N(^2D)$	7×10^{-18}
(R536)	$N_2(A\,^3\Sigma) + O \rightarrow O(^1D) + N_2$	2.3×10^{-17}
(R537)	$N_2(A\,^3\Sigma) + H_2O \rightarrow H + OH + N_2$	5×10^{-20}
(R538)	$N_2(B\,^3\Pi) + N_2 \rightarrow N_2(A\,^3\Sigma) + N_2$	5×10^{-17}
(R539)	$N_2(B\,^3\Pi) + \rightarrow N_2(A\,^3\Sigma)$	1.25×10^{5}
(R540)	$N_2(B\,^3\Pi) + NO \rightarrow N_2(A\,^3\Sigma) + NO$	2.4×10^{-16}
(R541)	$N_2(B\,^3\Pi) + O_2 \rightarrow N_2 + O + O$	3×10^{-16}
(R542)	$N_2(B\,^3\Pi) + H_2 \rightarrow N_2(A\,^3\Sigma) + H_2$	2.5×10^{-17}
(R543)	$O + O + M \rightarrow O_2 + M$	$3.2 \times 10^{-47} \exp(900/T_g)$
(R544)	$O + O_2 + M \rightarrow O_3 + M$	$3.4 \times 10^{-46}\ (300/T_g)^{1.2}$
(R545)	$O + O_3 \rightarrow O_2 + O_2$	$8 \times 10^{-18} \exp(-2060/T_g)$
(R546)	$O + NO + M \rightarrow NO_2 + M$	$1 \times 10^{-43}\ (300/T_g)^{1.6}$
(R547)	$O + NO_2 \rightarrow NO + O_2$	$6.5 \times 10^{-18} \exp(120/T_g)$
(R548)	$O + NO_2 + M \rightarrow NO_3 + M$	$9 \times 10^{-44}\ (300/T_g)^{2}$
(R549)	$O + NO_3 \rightarrow O_2 + NO_2$	1.7×10^{-17}
(R550)	$O + H + M \rightarrow OH + M$	1.62×10^{-44}
(R551)	$O + OH \rightarrow H + O_2$	$2.2 \times 10^{-17} \exp(-350/T_g)$
(R552)	$O + H_2O_2 \rightarrow OH + HO_2$	$3.3 \times 10^{-17} \exp(-2950/T_g)$
(R553)	$O + HO_2 \rightarrow OH + O_2$	$8.3 \times 10^{-17} \exp(-500/T_g)$
(R554)	$O + HNO \rightarrow OH + NO$	5.99×10^{-17}
(R555)	$O + HNO_2 \rightarrow NO_2 + OH$	$2 \times 10^{-17} \exp(-3000/T_g)$
(R556)	$O(^1D) + O_2 \rightarrow O + O_2$	$6.4 \times 10^{-18} \exp(67/T_g)$
(R557)	$O(^1D) + O \rightarrow O + O$	8×10^{-18}
(R558)	$O(^1D) + O_2(a\,^1\Delta) \rightarrow O + O_2$	1×10^{-17}
(R559)	$O(^1D) + O_2 \rightarrow O + O_2(a\,^1\Delta)$	1×10^{-18}
(R560)	$O(^1D) + O_3 \rightarrow O + O + O_2$	1.2×10^{-16}
(R561)	$O(^1D) + O_3 \rightarrow O_2 + O_2$	1.2×10^{-16}
(R562)	$O(^1D) + N_2 \rightarrow O + N_2$	$1.8 \times 10^{-17} \exp(107/T_g)$
(R563)	$O(^1D) + N_2 + M \rightarrow N_2O + M$	9×10^{-49}
(R564)	$O(^1D) + N_2O \rightarrow N_2 + O_2$	4.4×10^{-17}
(R565)	$O(^1D) + N_2O \rightarrow NO + NO$	7.2×10^{-17}
(R566)	$O(^1D) + NO \rightarrow O + NO$	4×10^{-17}
(R567)	$O(^1D) + NO_2 \rightarrow NO + O_2$	1.4×10^{-16}
(R568)	$O(^1D) + H_2 \rightarrow OH + H$	1.1×10^{-16}
(R569)	$O(^1D) + H_2O \rightarrow OH + OH$	2.2×10^{-16}
(R570)	$O_2(a\,^1\Delta) + O_2 \rightarrow O_2 + O_2$	$3.8 \times 10^{-24} \exp(-205/T_g)$
(R571)	$O_2(a\,^1\Delta) + O_3 \rightarrow O + O_2 + O_2$	$5.2 \times 10^{-17} \exp(-2840/T_g)$
(R572)	$O_2(a\,^1\Delta) + M \rightarrow O_2 + M$	8×10^{-27}
(R573)	$O_2(a\,^1\Delta) + NO \rightarrow O_2 + NO$	2.5×10^{-17}
(R574)	$O_2(a\,^1\Delta) + N_2 \rightarrow O_2 + N_2$	1.5×10^{-24}
(R575)	$O_3 + NO \rightarrow NO_2 + O_2$	$1.8 \times 10^{-18} \exp(-1370/T_g)$
(R576)	$O_3 + NO_2 \rightarrow NO_3 + O_2$	$1.4 \times 10^{-19} \exp(-2470/T_g)$
(R577)	$O_3 + M \rightarrow O + O_2 + M$	$3.92 \times 10^{-16} \exp(-11\,400/T_g)$
(R578)	$O_3 + H \rightarrow OH + O_2$	$2.8 \times 10^{-17}\ (T_g/300)^{0.75}$

(R579)	$O_3 + OH \rightarrow HO_2 + O_2$	$1.6 \times 10^{-18} \exp(-1000/T_g)$
(R580)	$O_3 + HO_2 \rightarrow OH + O_2 + O_2$	$1.4 \times 10^{-20} \exp(-600/T_g)$
(R581)	$NO + NO_2 + M \rightarrow N_2O_3 + M$	$3.09 \times 10^{-46} (300/T_g)^{7.7}$
(R582)	$NO + NO_3 \rightarrow NO_2 + NO_2$	$1.8 \times 10^{-17} \exp(110/T_g)$
(R583)	$NO + OH + M \rightarrow HNO_2 + M$	$7.4 \times 10^{-43} (300/T_g)^{2.4}$
(R584)	$NO + H + M \rightarrow HNO + M$	$1 \times 10^{-44} \exp(300/T_g)$
(R585)	$NO + HO_2 \rightarrow OH + NO_2$	$3.4 \times 10^{-18} \exp(270/T_g)$
(R586)	$NO + HO_2 \rightarrow O_2 + HNO$	$3.3 \times 10^{-19} \exp(-1000/T_g)$
(R587)	$NO_2 + NO_2 + M \rightarrow N_2O_4 + M$	$1.17 \times 10^{-45} (300/T_g)^{3.8}$
(R588)	$NO_2 + NO_3 + M \rightarrow N_2O_5 + M$	$2.8 \times 10^{-42} (300/T_g)^{3.5}$
(R589)	$NO_2 + NO_3 \rightarrow NO_2 + NO + O_2$	$2.3 \times 10^{-19} \exp(-1600/T_g)$
(R590)	$NO_2 + H \rightarrow OH + NO$	1.47×10^{-16}
(R591)	$NO_2 + OH + M \rightarrow HNO_3 + M$	$2.2 \times 10^{-42} (300/T_g)^{2.9}$
(R592)	$NO_3 + NO_3 \rightarrow NO_2 + NO_2 + O_2$	$5 \times 10^{-18} \exp(-3000/T_g)$
(R593)	$NO_3 + H \rightarrow OH + NO_2$	$5.8 \times 10^{-16} \exp(-750/T_g)$
(R594)	$NO_3 + OH \rightarrow HO_2 + NO_2$	2×10^{-17}
(R595)	$NO_3 + HO_2 \rightarrow NO_2 + OH + O_2$	4.8×10^{-18}
(R596)	$NO_3 + HO_2 \rightarrow HNO_3 + O_2$	9.2×10^{-19}
(R597)	$N_2O_3 + M \rightarrow NO + NO_2 + M$	$1.03 \times 10^{-16} \exp(-2628/T_g)$
(R598)	$N_2O_4 + M \rightarrow NO_2 + NO_2 + M$	$1.09 \times 10^{-13} \exp(-4952/T_g)$
(R599)	$N_2O_5 + M \rightarrow NO_2 + NO_3 + M$	$1 \times 10^{-9} (300/T_g)^{3.5} \exp(-11\,000/T_g)$
(R600)	$H + O_2 + M \rightarrow HO_2 + M$	$5.4 \times 10^{-44} (T_g/300)^{-1.8}$
(R601)	$H + H + M \rightarrow H_2 + M$	$1.8 \times 10^{-42}/T_g$
(R602)	$H + OH + M \rightarrow H_2O + M$	$6.1 \times 10^{-38}/T_g^2$
(R603)	$H + H_2O_2 \rightarrow OH + H_2O$	$1.69 \times 10^{-17} \exp(-1800/T_g)$
(R604)	$H + H_2O_2 \rightarrow HO_2 + H_2$	$2.8 \times 10^{-18} \exp(-1900/T_g)$
(R605)	$H + HO_2 \rightarrow H_2 + O_2$	5.6×10^{-18}
(R606)	$H + HO_2 \rightarrow O + H_2O$	2.4×10^{-18}
(R607)	$H + HO_2 \rightarrow OH + OH$	$4.2 \times 10^{-16} \exp(-950/T_g)$
(R608)	$H + HNO \rightarrow NO + H_2$	$3 \times 10^{-17} \exp(-500/T_g)$
(R609)	$H + HNO_2 \rightarrow NO_2 + H_2$	$2 \times 10^{-17} \exp(-3700/T_g)$
(R610)	$H + HNO_3 \rightarrow NO_2 + H_2O$	$1.39 \times 10^{-20} (T_g/298)^{3.29} \exp(-3160/T_g)$
(R611)	$H_2 + OH \rightarrow H + H_2O$	$3.2 \times 10^{-17} \exp(-2600/T_g)$
(R612)	$OH + OH \rightarrow O + H_2O$	$8.8 \times 10^{-18} \exp(-503/T_g)$
(R613)	$OH + OH + M \rightarrow H_2O_2 + M$	$6.9 \times 10^{-43} (T_g/300)^{-0.8}$
(R614)	$OH + HO_2 \rightarrow O_2 + H_2O$	$4.8 \times 10^{-17} \exp(250/T_g)$
(R615)	$OH + H_2O_2 \rightarrow HO_2 + H_2O$	$2.9 \times 10^{-18} \exp(-160/T_g)$
(R616)	$OH + HNO \rightarrow NO + H_2O$	$8 \times 10^{-17} \exp(-500/T_g)$
(R617)	$OH + HNO_2 \rightarrow NO_2 + H_2O$	$1.8 \times 10^{-17} \exp(-390/T_g)$
(R618)	$OH + HNO_3 \rightarrow NO_3 + H_2O$	$1.5 \times 10^{-20} \exp(650/T_g)$
(R619)	$HO_2 + HO_2 \rightarrow H_2O_2 + O_2$	$2.2 \times 10^{-19} \exp(600/T_g)$
(R620)	$HNO + O_2 \rightarrow NO + HO_2$	$5.25 \times 10^{-18} \exp(-1510/T_g)$
(R621)	$HNO + O_2 \rightarrow NO_2 + OH$	1.66×10^{-21}
(R622)	$HNO + HNO \rightarrow N_2O + H_2O$	$1.4 \times 10^{-21} \exp(-1600/T_g)$
(R623)	$HNO_2 + HNO_2 \rightarrow NO + NO_2 + H_2O$	1×10^{-26}
(R624)	$HNO_2 + HNO_3 \rightarrow NO_2 + NO_2 + H_2O$	1.6×10^{-23}

Appendix C: Chemistry sub-model reactions (chapter 6)

Table 8: List of reactions and the rate constants. [142]

Index	Reaction	Rate constant
(R1)	$e + N_2 \rightarrow e + N_2$	$f(\varepsilon_{avg})^{b}$
(R2)	$e + O_2 \rightarrow e + O_2$	$f(\varepsilon_{avg})^{b}$
(R3)	$e + N_2 \rightarrow 2e + N_2^+$	$1 \times 10^{-16}\ \varepsilon_{avg}\ 1.9 \exp(-14.6/\varepsilon_{avg})$
(R4)	$e + O_2 \rightarrow 2e + O_2^+$	$9.54 \times 10^{-12}\ \varepsilon_{avg}-1.05 \exp(-55.6/\varepsilon_{avg})$
(R5)	$e + O_2 \rightarrow O_2^-$	$9.72 \times 10^{-15}\ \varepsilon_{avg}-1.62 \exp(-14.2/\varepsilon_{avg})\ \varepsilon_{avg} > 1.13\ 2.78 \times 10^{-20}\ \varepsilon_{avg} < 1.13$
(R6)	$e + N_2 + O_2 \rightarrow N_2 + O_2^-$	$1.1 \times 10^{-43}\ (T_g/T_e)2 \exp(-70/T_g) \exp(1500(Te - T_g)/(TeT_g))$
(R7)	$e + 2O_2 \rightarrow O_2 + O_2^-$	$1.4 \times 10^{-41}\ (T_g/T_e) \exp(-600/T_g) \exp(700(T_e - T_g)/(TeT_g))$
(R8)	$M + e + N_2^+ \rightarrow M + N_2$	$3.12 \times 10^{-35}/Te$
(R9)	$N_2 + O_2^- \rightarrow e + O_2 + N_2$	$1.9 \times 10^{-18}(T_g/300)0.5 \exp(-4990/T_g)$
(R10)	$O_2 + O_2^- \rightarrow e + O_2 + O_2$	$2.7 \times 10^{-16}(T_g/300)0.5 \exp(-5590/T_g)$
(R11)	$O_2 + N_2^+ \rightarrow O_2^+ + N_2$	5×10^{-17}
(R12)	$O_2^- + N_2^+ \rightarrow O_2 + N_2$	$2 \times 10^{-13}(300/T_g)0.5$
(R13)	$O_2^- + O_2^+ \rightarrow 2O_2$	$2 \times 10^{-13}(300/T_g)0.5$
(R14)	$e + O_2 \rightarrow 2O + e$	$2.03 \times 10^{-14}\ \varepsilon_{avg}-0.1 \exp(-8.47/\varepsilon_{avg})$
(R15)	$M + 2O \rightarrow M + O_2$	$3.2 \times 10^{-47} \exp(900/T_g)$
(R16)	$M + O + O_2 \rightarrow M + O_3$	$3.4 \times 10^{-46}\ (300/T_g)1.2$
(R17)	$O + O_3 \rightarrow 2O_2$	$8 \times 10^{-18} \exp(-2060/T_g)$
(R18)	$M + O_3 \rightarrow M + O + O_2$	$3.92 \times 10^{-16} \exp(-11400/T_g)$

References

[1] U. Römling and C. Balsalobre, “Biofilm infections, their resilience to therapy and innovative treatment strategies,” *J. Intern. Med.*, vol. 272, no. 6, pp. 541–561, 2012.

[2] W. Siemens, “Ueber die elektrostatische Induction und die Verzögerung des Stroms in Flaschendrähten,” *Ann. Phys.*, vol. 178, no. 9, 1857.

[3] U. Kogelschatz, “Dielectric-barrier discharges: Their History, Discharge Physics, and Industrial Applications,” *Plasma Chem. Plasma Process.*, vol. 23, no. 1, pp. 1–46, 2003.

[4] A. Fridman, *Plasma Chemistry*. 2008.

[5] F. Chen, *Introduction to Plasma Physics and Controlled Fusion*. 1984.

[6] J. Kriegseis, “Performance Characterization and Quantification of Dielectric Barrier Discharge Plasma Actuators,” Technischen Universität Darmstadt, 2011.

[7] J. R. Roth, *Industrial Plasma Engineering Volume 2*. .

[8] F. Paschen, “Ueber die zum Funkenübergang in Luft, Wasserstoff und Kohlensäure bei verschiedenen Drucken erforderliche Potentialdifferenz,” *Ann. Phys.*, vol. 273, pp. 69–96, 1889.

[9] J.-S. Yoon, “Dielectric barrier discharge plasma actuator study for low Reynolds number flow control,” 2015.

[10] T. Andrews and P. G. Tait, “On the Volumetric Relations of Ozone , and the Action of the Electrical Discharge on Oxygen and Other Gases,” *Phil. Trans. R. Soc. Lond.*, no. January, pp. 113–131, 1860.

[11] H. Becker, “Wissenschaftliche Veröffentlichungen aus dem Siemens-Konzern-Scientific publications from Siemens group,” *Springer B.*, vol. 3, no. 243, 1923.

[12] M. P. Otto, *L’ozone et ses applications*, vol. 1931. .

[13] E. Warburg, “Über spontane Desozonisierung, BerichtigungTitle,” *Ann. Phys.*, vol.

318, no. 5, 1904.

[14] E. Warburg and G. Leithäuser, "Leistungsmessungen an Ozonröhren," *Ann. Phys.*, vol. 333, no. 1, 1909.

[15] I. Langmuir, "Oscillations in Ionized Gases," *Proc Natl Acad Sci U S A.*, vol. 14, pp. 627–637, 1928.

[16] K. Buss, *Die elektrodenlose Entladung nach Messung mit dem Kathodenoszillographen*, vol. 26. 1932.

[17] A. Klemenc, H. Hinterberger, and H. Hofer, "No Title," *Z. Elektrochem*, vol. 43, 1937.

[18] K. Honda and Y. Naito, "On the Nature of Silent Electric Discharge," *J. Phys. Soc. Jpn.*, vol. 10, pp. 1007–1011, 1955.

[19] H. Gobrecht, O. Meinhardt, and F. Hein, "Uber die stille elektrische Entladung in Ozonisatoren," *Ber. Bunsenges. f. phys. Chem.*, vol. 68, 1964.

[20] T. C. Manley, "The Electric Characteristics of the Ozonator Discharge," *JES*, vol. 84, pp. 83–96, 1943.

[21] U. Kogelschatz, "Dielectric Barrier Discharge : Their History, Discharge Physic, and Industrial Applications," *Plasma Chem. Plasma Process.*, vol. 23, no. 1, p. 1, 2003.

[22] A. Fridman and L. A. Kennedy, *Plasma Physics and Engineeringe*. CRC Press, 2004.

[23] K. Becker, U. Kogelschatz, K. Schoenbach, and R. Barker, *Non-Equilibrium Air Plasmas at Atmospheric Pressure*. 2005.

[24] O. Guaitella, "Nature de la synergie plasma-photocatalyseur pour la destruction d'un composé organique volatil type : l'acétylène," Ecole Polytechnique X, 2006.

[25] "Nik Plasma Tech, Dielectric barrier." [Online]. Available: http://nikplasma.com/en/laboratory-equipment/dbd-plasma/.

[26] A. Chirokov, A. Gutsol, and A. Fridman, "Atmospheric pressure plasma of dielectric barrier discharges," *Pure Appl. Chem.*, vol. 77, no. 2, pp. 487–495, 2005.

[27] B. Eliasson, M. Hirth, and U. Kogelschatz, "Ozone synthesis from oxygen in dielectric

barrier discharges," *J. Phys. D. Appl. Phys.*, vol. 20, no. 11, p. 1421, 1987.

[28] T. von Woedtke, S. Reuter, K. Masur, and K. D. Weltmann, "Plasmas for medicine," *Phys. Rep.*, vol. 530, no. 4, pp. 291–320, 2013.

[29] D. Dobrynin, K. Arjunan, A. Fridman, G. Friedman, and A. M. Clyne, "Direct and controllable nitric oxide delivery into biological media and living cells by a pin-to-hole spark discharge (PHD) plasma," *J. Phys. D. Appl. Phys.*, vol. 44, no. 7, p. 075201, 2011.

[30] J. Balzer *et al.*, "Non-Thermal Dielectric Barrier Discharge (DBD) effects on proliferation and differentiation of human fibroblasts are primary mediated by hydrogen peroxide," *PLoS One*, vol. 10, no. 12, pp. 1–18, 2015.

[31] D. B. Graves, "The emerging role of reactive oxygen and nitrogen species in redox biology and some implications for plasma applications to medicine and biology," *J. Phys. D. Appl. Phys.*, vol. 45, no. 26, p. 263001, 2012.

[32] E. García-Alcantara *et al.*, "Accelerated mice skin acute wound healing in vivo by combined treatment of argon and helium plasma needle," *Arch. Med. Res.*, vol. 44, no. 3, pp. 169–177, 2013.

[33] Z. Chen *et al.*, "A novel micro cold atmospheric plasma device for glioblastoma both in vitro and in vivo," *Cancers (Basel).*, vol. 9, no. 6, pp. 1–16, 2017.

[34] S. Bekeschus, A. Schmidt, K. D. Weltmann, and T. von Woedtke, "The plasma jet kINPen – A powerful tool for wound healing," *Clin. Plasma Med.*, vol. 4, no. 1, pp. 19–28, 2016.

[35] A. V. Nastuta, I. Topala, C. Grigoras, V. Pohoata, and G. Popa, "Stimulation of wound healing by helium atmospheric pressure plasma treatment," *J. Phys. D. Appl. Phys.*, vol. 44, no. 10, 2011.

[36] Y. T. Chang and G. Chen, "Oral bacterial inactivation using a novel low-temperature atmospheric-pressure plasma device," *J. Dent. Sci.*, vol. 11, no. 1, pp. 65–71, 2014.

[37] L. Taghizadeh, G. Brackman, A. Y. Nikiforov, T. Coenye, and C. Leys, “Antibiofilm effect of argon plasma jet,” *Ispc_20*, pp. 1–4, 2011.

[38] G. E. Morfill, T. Shimizu, B. Steffes, and H. U. Schmidt, “Nosocomial infections - A new approach towards preventive medicine using plasmas,” *New J. Phys.*, vol. 11, p. 115019, 2009.

[39] T. Shimizu, Y. Sakiyama, D. B. Graves, J. L. Zimmermann, and G. E. Morfill, “The dynamics of ozone generation and mode transition in air surface micro-discharge plasma at atmospheric pressure,” *New J. Phys.*, vol. 14, no. 10, p. 103028, 2012.

[40] T. Shimizu, J. L. Zimmermann, and G. E. Morfill, “The bactericidal effect of surface micro-discharge plasma under different ambient conditions,” 2011.

[41] T. He *et al.*, “A ‘ tissue model ’ to study the barrier effects of living tissues on the reactive species generated by surface air discharge,” *J. Phys. D Appl. Phys*, no. 49, p. 205204, 2016.

[42] W. Liu, L. Zhu, X. Chen, L. Zhao, and S. Sun, “Study on Generation of Glow Discharge Plasma in Air and Surface Modification of Wool Fabric,” *Plasma Chem. Plasma Process.*, vol. 39, no. 2, pp. 487–501, 2019.

[43] Y. Song *et al.*, “An Atmospheric-Pressure Large-Area Diffuse Used for Disinfection Application,” *IEEE Trans. Plasma Sci.*, vol. 43, no. 3, pp. 821–827, 2015.

[44] K. Heuer *et al.*, “The topical use of non-thermal dielectric barrier discharge (DBD): Nitric oxide related effects on human skin,” *Nitric Oxide - Biol. Chem.*, vol. 44, no. 1, pp. 52–60, 2015.

[45] N. Y, M. J. Lynch, M. Modic, R. D. Whalley, and J. L. Walsh, “A solar powered handheld plasma source for microbial decontamination applications,” 2016.

[46] Y. Sakiyama, D. B. Graves, H. Chang, T. Shimizu, and G. E. Morfill, “Plasma chemistry model of surface microdischarge in humid air and dynamics of reactive neutral species,” 2012.

[47] M. J. Pavlovich, D. S. Clark, and D. B. Graves, “Quantification of air plasma chemistry for surface disinfection,” *Plasma Sources Sci. Technol.*, vol. 23, no. 6, 2014.

[48] M. I. Hasan and J. L. Walsh, “Numerical investigation of the spatiotemporal distribution of chemical species in an atmospheric surface barrier-discharge,” *J. Appl. Phys.*, vol. 119, no. 20, 2016.

[49] T. Shimizu, Y. Sakiyama, D. B. Graves, J. L. Zimmermann, and G. E. Morfill, “The dynamics of ozone generation and mode transition in air surface micro-discharge plasma at atmospheric pressure,” *New J. Phys.*, vol. 14, no. 10, p. 103028, 2012.

[50] S. Pekarek and J. Mikes, “Temperature-and airflow-related effects of ozone production by surface dielectric barrier discharge in air,” no. 2, 2014.

[51] S. Pekárek, “Non-Thermal Plasma Ozone Generation,” vol. 43, no. 6, 2003.

[52] Y. Sakiyama, D. B. Graves, H. W. Chang, T. Shimizu, and G. E. Morfill, “Plasma chemistry model of surface microdischarge in humid air and dynamics of reactive neutral species,” *J. Phys. D. Appl. Phys.*, vol. 45, no. 42, 2012.

[53] A. Al-abduly and P. Christensen, “An in situ and downstream study of non-thermal plasma chemistry in an air fed dielectric barrier discharge (DBD),” *Plasma Sources Sci. Technol*, vol. 24, 2015.

[54] S. Yonemori, Y. Nakagawa, R. Ono, and T. Oda, “Measurement of OH density and air – helium mixture ratio in an atmospheric-pressure helium plasma jet,” vol. 225202, 2012.

[55] R. Bansemer, A. Schmidt-Bleker, U. Van Rienen, and K.-D. Weltmann, “Investigation and control of the O3- to NO-transition in a novel sub-atmospheric pressure dielectric barrier discharge,” *Plasma Sources Sci. Technol.*, vol. 26, no. 6, 2017.

[56] R. E. Nightingale, A. R. Downie, D. L. Rotenberg, B. Crawford, and R. A. Ogg, “The preparation and infrared spectra of the oxides of nitrogen,” *J. Phys. Chem.*, vol. 58, no. 11, pp. 1047–1050, 1954.

[57] D. J. McCaa and J. H. Shaw, “The Infrared Spectrum of Ozone,” *J. Mol. Spectrosc.*, vol. 25, pp. 374–397, 1968.

[58] C. Haridass, A. Aw-Musse, P. Misra, and J. Jordan, “Fourier Transform infrared (FT-IR) spectroscopy of trace molecular species of importance for the elucidation of atmospheric phenomena,” *Comput. Electr. Eng.*, vol. 26, 2000.

[59] G. Herzberg, *Molecular spectra and molecular structure: Infrared and Raman spectra of polyatomic molecules*. 1945.

[60] A. F. H. Van Gessel, K. M. J. Alards, and P. J. Bruggeman, “NO production in an RF plasma jet at atmospheric pressure,” *J. Phys. D. Appl. Phys.*, vol. 46, no. 26, p. 265202, 2013.

[61] A. F. H. Van Gessel, B. Hrycak, M. Jasiński, J. Mizeraczyk, J. J. A. M. Van Der Mullen, and P. J. Bruggeman, “Temperature and NO density measurements by LIF and OES on an atmospheric pressure plasma jet,” *J. Phys. D. Appl. Phys.*, vol. 46, no. 9, p. 095201, 2013.

[62] Y. Kim, G. Kim, Y. Shin, and J. Kwak, “Experimental Investigation on the Effects of DBD Plasma on the Film Cooling Effectiveness of a 30-Degree Slot,” *Appl. Sci.*, vol. 7, no. 6, p. 633, 2017.

[63] P. Audier, M. Fénot, N. Bénard, and E. Moreau, “Film cooling effectiveness enhancement using surface dielectric barrier discharge plasma actuator,” *Int. J. Heat Fluid Flow*, vol. 62, pp. 247–257, 2016.

[64] K.-S. Choi *et al.*, “Plasma Virtual Actuators for Flow Control,” *J. Flow Control. Meas. & Vis.*, vol. 03, no. 01, pp. 22–34, 2015.

[65] Richard D. Whalley, “Turbulent boundary-layer control with DBD plasma actuators using spanwise travelling-wave technique,” 2011.

[66] M. Robinson, “A History of the Electric Wind,” *Am. J. Phys.*, vol. 10, pp. 366–372, 1962.

[67] E. Moreau *et al.*, “Surface Dielectric Barrier Discharge Plasma Actuators,” pp. 5–10.

[68] J. J. Wang, K. S. Choi, L. H. Feng, T. N. Jukes, and R. D. Whalley, “Recent developments in DBD plasma flow control,” *Prog. Aerosp. Sci.*, vol. 62, pp. 52–78, 2013.

[69] R. D. Whalley and J. L. Walsh, “Turbulent jet flow generated downstream of a low temperature dielectric barrier atmospheric pressure plasma device,” *Sci. Rep.*, vol. 6, no. July, pp. 1–7, 2016.

[70] E. Traldi *et al.*, “Schlieren imaging: a powerful tool for atmospheric plasma diagnostic,” *EPJ Tech. Instrum.*, vol. 5, no. 1, pp. 1–23, 2018.

[71] G. S. Settles and M. J. Hargather, “A review of recent developments in schlieren and shadowgraph techniques,” *Meas. Sci. Technol.*, vol. 28, no. 4, 2017.

[72] M. I. Hasan and J. L. Walsh, “Influence of gas flow velocity on the transport of chemical species in an atmospheric pressure air plasma discharge,” *Appl. Phys. Lett.*, vol. 110, no. 13, 2017.

[73] M. Taglioli *et al.*, “EHD-driven mass transport enhancement in surface dielectric barrier discharges,” *Plasma Sources Sci. Technol.*, vol. 25, no. 6, 2016.

[74] T. C. Corke, C. L. Enloe, and S. P. Wilkinson, “Dielectric Barrier Discharge Plasma Actuators for Flow Control,” *Annu. Rev. Fluid Mech.*, vol. 42, no. 1, pp. 505–529, 2009.

[75] E. Moreau, R. Sosa, and G. Artana, “Electric wind produced by surface plasma actuators: A new dielectric barrier discharge based on a three-electrode geometry,” *J. Phys. D. Appl. Phys.*, vol. 41, no. 11, 2008.

[76] H. Akbıyık, H. Yavuz, and Y. E. Akansu, “A Study on the Plasma Actuator Electrode Geometry Configurations for Improvement of the Aerodynamic Performance of an Airfoil,” *J. Mech. Eng.*, vol. 64, no. 12, pp. 1–7, 2018.

[77] H. Akbıyık, H. Yavuz, and Y. E. Akansu, “Investigation of the Electrode Geometry

Configurations of Plasma Actuators," no. June, pp. 9–16, 2017.

[78] C. L. Enloe *et al.*, "Mechanisms and Responses of a Dielectric Barrier Plasma Actuator: Geometric Effects," *AIAA J.*, vol. 42, no. 3, pp. 595–604, 2004.

[79] S. Y. Xu, J. S. Cai, Z. K. Zhang, and S. J. Tang, "Investigation of the electrode surface geometry effects driven by nanosecond-pulsed surface dielectric barrier discharge," *J. Phys. D. Appl. Phys.*, vol. 50, no. 18, 2017.

[80] N. Benard, J. P. Bonnet, G. Touchard, and E. Moreau, "Flow Control by Dielectric Barrier Discharge Actuators: Jet Mixing Enhancement," *AIAA J.*, vol. 46, no. 9, pp. 2293–2305, 2008.

[81] G. Neretti, A. Cristofolini, and C. A. Borghi, "Experimental investigation on a vectorized aerodynamic dielectric barrier discharge plasma actuator array," *J. Appl. Phys.*, vol. 115, no. 16, 2014.

[82] C. Ozturk and J. Jacob, "Aerodynamic Flow Control Using Jet Vectoring Plasma Actuators," *AIAA J.*, 2012.

[83] J. Foster, B. S. Sommers, S. N. Gucker, I. M. Blankson, and G. Adamovsky, "Perspectives on the interaction of plasmas with liquid water for water purification," *IEEE Trans. Plasma Sci.*, vol. 40, no. 5 PART 1, pp. 1311–1323, 2012.

[84] M. Sato, T. Ohgiyama, and J. S. Clements, "Formation of chemical species and their effects on microorganisms using a pulsed high-voltage discharge in water," *Ieee*, vol. 32, no. 1, pp. 106–112, 1996.

[85] M. Naítali, G. Kamgang-Youbi, J. M. Herry, M. N. Bellon-Fontaine, and J. L. Brisset, "Combined effects of long-living chemical species during microbial inactivation using atmospheric plasma-treated water," *Appl. Environ. Microbiol.*, vol. 76, no. 22, pp. 7662–7664, 2010.

[86] P. Lukes, E. Dolezalova, I. Sisrova, and M. Clupek, "Aqueous-phase chemistry and bactericidal effects from an air discharge plasma in contact with water: evidence for

the formation of peroxynitrite through a pseudo-second-order post-discharge reaction of H 2 O 2 and HNO 2," *Plasma Sources Sci. Technol.*, vol. 23, no. 1, p. 015019, 2014.

[87] J. Shen *et al.*, "Bactericidal Effects against S. aureus and Physicochemical Properties of Plasma Activated Water stored at different temperatures," *Sci. Rep.*, vol. 6, no. 1, p. 28505, 2016.

[88] P. J. Bruggeman *et al.*, "Plasma-liquid interactions: A review and roadmap," *Plasma Sources Sci. Technol.*, vol. 25, no. 5, 2016.

[89] P. Bruggeman and C. Leys, "Non-thermal plasmas in and in contact with liquids," *J. Phys. D. Appl. Phys.*, vol. 42, no. 5, 2009.

[90] W. Tian and M. J. Kushner, "Atmospheric pressure dielectric barrier discharges interacting with liquid covered tissue," *J. Phys. D. Appl. Phys.*, vol. 47, no. 16, 2014.

[91] S. Samukawa *et al.*, "The 2012 Plasma Roadmap," *J. Phys. D. Appl. Phys.*, vol. 45, no. 25, p. 253001, 2012.

[92] D. X. Liu *et al.*, "Aqueous reactive species induced by a surface air discharge: Heterogeneous mass transfer and liquid chemistry pathways," *Sci. Rep.*, vol. 6, no. April, pp. 1–11, 2016.

[93] R. Zhou *et al.*, "Cold atmospheric plasma activated water as a prospective disinfectant: The crucial role of peroxynitrite," *Green Chem.*, vol. 20, no. 23, pp. 5276–5284, 2018.

[94] J. Chauvin, F. Judée, M. Yousfi, P. Vicendo, and N. Merbahi, "Analysis of reactive oxygen and nitrogen species generated in three liquid media by low temperature helium plasma jet," *Sci. Rep.*, vol. 7, no. September 2016, pp. 1–15, 2017.

[95] F. Judée, S. Simon, and T. Dufour, "Plasma-activation of tap water using DBD for agronomy applications: Identification and quantification of long lifetime chemical species and production/consumption mechanisms," *Water Res.*, vol. 133, pp. 47–59,

2017.

[96] W. B. Kuvshinov, D., Siswanto, A., Lozano-Parada, J., Zimmerman, “Efficient Compact Micro DBD Plasma Reactor for Ozone Generation for Industrial Application in Liquid and Gas Phase Systems,” vol. 8, no. 1, pp. 8–11, 2014.

[97] C. C. Beltrá, “Fluorescent Probes for Selective Detection of Ozone in Plasma Applications.”

[98] S. I. Imai, Y. Sakaguchi, and T. Shirafuji, “Simultaneous generation of acidic and alkaline water using atmospheric air plasma formed in water,” *Jpn. J. Appl. Phys.*, vol. 57, no. 1, pp. 0–6, 2018.

[99] T. Abuzairi, S. Ramadhanty, D. F. Puspohadiningrum, A. Ratnasari, N. R. Poespawati, and R. W. Purnamaningsih, “Investigation on physicochemical properties of plasma-activated water for the application of medical device sterilization,” *AIP Conf. Proc.*, vol. 1933, no. February, pp. 1–7, 2018.

[100] G. Fridman *et al.*, “Comparison of direct and indirect effects of non-thermal atmospheric-pressure plasma on bacteria,” *Plasma Process. Polym.*, vol. 4, no. 4, pp. 370–375, 2007.

[101] D. Butscher, D. Zimmermann, M. Schuppler, and P. Rudolf von Rohr, “Plasma inactivation of bacterial endospores on wheat grains and polymeric model substrates in a dielectric barrier discharge,” *Food Control*, vol. 60, pp. 636–645, 2016.

[102] D. Z. Yang *et al.*, “Atmospheric pressure gas-liquid diffuse nanosecond pulse discharge used for sterilization in sewage,” *Plasma Process. Polym.*, vol. 11, no. 9, pp. 842–849, 2014.

[103] T. Nosenko, T. Shimizu, and G. E. Morfill, “Designing plasmas for chronic wound disinfection,” *New J. Phys.*, vol. 11, 2009.

[104] M. Modic, N. P. McLeod, J. M. Sutton, and J. L. Walsh, “Cold atmospheric pressure

plasma elimination of clinically important single- and mixed-species biofilms," *Int. J. Antimicrob. Agents*, vol. 49, no. 3, pp. 375–378, 2017.

[105] D. Ziuzina, S. Patil, P. J. Cullen, D. Boehm, and P. Bourke, "Dielectric Barrier Discharge Atmospheric Cold Plasma for Inactivation of Pseudomonas aeruginosa Biofilms," *Plasma Med.*, vol. 4, no. 1–4, pp. 137–152, 2014.

[106] E. Simoncelli *et al.*, "Preliminary investigation of the antibacterial efficacy of a handheld Plasma Gun source for endodontic procedures," *Clin. Plasma Med.*, vol. 3, no. 2, pp. 77–86, 2015.

[107] S. G. Joshi, M. Paff, G. Friedman, G. Fridman, A. Fridman, and A. D. Brooks, "Control of methicillin-resistant Staphylococcus aureus in planktonic form and biofilms: A biocidal efficacy study of nonthermal dielectric-barrier discharge plasma," *Am. J. Infect. Control*, vol. 38, no. 4, pp. 293–301, 2010.

[108] Z. Kovalova *et al.*, "Atmospheric pressure argon surface discharges propagated in long tubes: physical characterization and application to bio-decontamination," *J. Phys. D. Appl. Phys.*, vol. 48, no. 46, p. 464003, 2015.

[109] M. J. Pavlovich, D. S. Clark, and D. B. Graves, "Quantification of air plasma chemistry for surface disinfection," *Plasma Sources Sci. Technol.*, vol. 23, no. 6, p. 065036, 2014.

[110] K. Fricke *et al.*, "Atmospheric pressure plasma: A high-performance tool for the efficient removal of biofilms," *PLoS One*, vol. 7, no. 8, pp. 1–8, 2012.

[111] Y. Liang *et al.*, "Plasma Thorns: Atmospheric Pressure Non-Thermal Plasma Source for Dentistry Applications," *Plasma Process. Polym.*, p. n/a-n/a, 2015.

[112] S. A. Ermolaeva *et al.*, "Bactericidal effects of non-thermal argon plasma in vitro, in biofilms and in the animal model of infected wounds," *J. Med. Microbiol.*, vol. 60, no. 1, pp. 75–83, 2011.

[113] A. Mai-Prochnow, M. Clauson, J. Hong, and A. B. Murphy, "Gram positive and Gram

negative bacteria differ in their sensitivity to cold plasma," *Sci. Rep.*, vol. 6, no. December, 2016.

[114] L. Han, S. Patil, D. Boehm, V. Milosavljević, P. J. Cullen, and P. Bourke, "Mechanisms of Inactivation by High-Voltage Atmospheric Cold Plasma Differ for Escherichia coli and Staphylococcus aureus," *Appl. Environ. Microbiol.*, vol. 82, no. 2, pp. 450–458, 2016.

[115] A. Kilonzo-Nthenge, S. Liu, S. Yannam, and A. Patras, "Atmospheric Cold Plasma Inactivation of Salmonella and Escherichia coli on the Surface of Golden Delicious Apples," *Front. Nutr.*, vol. 5, no. December, pp. 1–9, 2018.

[116] S. G. Joshi *et al.*, " Nonthermal Dielectric-Barrier Discharge Plasma-Induced Inactivation Involves Oxidative DNA Damage and Membrane Lipid Peroxidation in Escherichia coli ," *Antimicrob. Agents Chemother.*, vol. 55, no. 3, pp. 1053–1062, 2011.

[117] X. Lei, Z. Rui, L. Peng, D. Li-Li, and Z. Ru-Juan, " Sterilization of E. coli bacterium with an atmospheric pressure surface barrier discharge ," *Chinese Phys.*, vol. 13, no. 6, pp. 913–917, 2004.

[118] R. Matthes *et al.*, "Antimicrobial Efficacy of Two Surface Barrier Discharges with Air Plasma against In Vitro Biofilms," *PLoS One*, vol. 8, no. 7, pp. 1–11, 2013.

[119] P. Lembre, C. Lorentz, and P. Di Martino, *Exopolysaccharides of the Biofilm Matrix: A Complex Biophysical World*, vol. i, no. tourism. 2012.

[120] D. Ziuzina, D. Boehm, S. Patil, P. J. Cullen, and P. Bourke, "Cold plasma inactivation of bacterial biofilms and reduction of quorum sensing regulated virulence factors," *PLoS One*, vol. 10, no. 9, pp. 1–21, 2015.

[121] Q. Hong *et al.*, "Disinfection of *Streptococcus mutans* biofilm by a non-thermal atmospheric plasma brush," *Jpn. J. Appl. Phys.*, vol. 55, no. 7S2, p. 07LG02, 2016.

[122] J. Aparecida Delben, C. Evelin Zago, N. Tyhovych, S. Duarte, and C. Eduardo Vergani,

"Effect of atmospheric-pressure cold plasma on pathogenic oral biofilms and in vitro reconstituted oral epithelium," *PLoS One*, vol. 11, no. 5, pp. 1–18, 2016.

[123] D. P. Arora, S. Hossain, Y. Xu, and E. M. Boon, "Nitric Oxide Regulation of Bacterial Biofilms," *Biochemistry*, vol. 54, no. 24, pp. 3717–3728, 2015.

[124] G. Brelles-mariño, "Challenges in Biofilm Inactivation : The Use of Cold Plasma as a New Approach," *J. Bioprocess. Biotech.*, vol. 2, no. 4, pp. 2–5, 2012.

[125] N. Education, "A biofilm is composed of attached microbial cells encased." [Online]. Available: https://www.nature.com/scitable/content/a-biofilm-is-composed-of-attached-microbial-100450918.

[126] S. Kalghatgi *et al.*, "Effects of non-thermal plasma on mammalian cells," *PLoS One*, vol. 6, no. 1, pp. 1–11, 2011.

[127] S. Kalghatgi *et al.*, "Toxicity analysis of direct nonthermal plasma treatment of living tissue," *2008 IEEE 35th Int. Conf. Plasma Sci.*, vol. 2008, p. 2008, 2008.

[128] S. W. Sharpe, R. L. Sams, and T. J. Johnson, "The PNNL quantitative IR database for infrared remote sensing and hyperspectral imaging," *Proc. - Appl. Imag. Pattern Recognit. Work.*, vol. 2002-Janua, pp. 45–48, 2002.

[129] P. A. Christensen, A. H. B. M. Ali, Z. T. A. W. Mashhadani, and P. A. Martin, "A Direct Fourier Transform Infrared Spectroscopic Comparison of the Plasma- and Thermally-Driven Reaction of CO2 at Macor," *Plasma Chem. Plasma Process.*, vol. 38, no. 2, pp. 293–310, 2018.

[130] V. Procházka *et al.*, "Coplanar surface barrier discharge ignited in water vapor - A selective source of OH radicals proved by (TA)LIF measurement," *Plasma Sources Sci. Technol.*, vol. 27, no. 1, p. 015001, 2018.

[131] J. B. Nee, C. Y. Juan, J. Y. Hsu, J. C. Yang, and W. J. Chen, "The electronic quenching rates of NO(A2Σ+, v′=0-2)," *Chem. Phys.*, vol. 300, no. 1–3, pp. 85–92, 2004.

[132] I. J. Wysong, "Vibrational energy transfer of NO (NO (X2Π, v=2 and 1)," *J. Chem.*

Phys., vol. 101, no. 4, p. 2800, 1994.

[133] T. B. Settersten, B. D. Patterson, and J. A. Gray, "Temperature- and species-dependent quenching of NO A 2Sigma+(v'=0) probed by two-photon laser-induced fluorescence using a picosecond laser.," *J. Chem. Phys.*, vol. 124, no. 23, p. 234308, 2006.

[134] J. Malicet, D. Daumont, J. Charbonnier, C. Parisse, A. Chakir, and J. Brion, "Ozone UV spectroscopy. II. Absorption cross-sections and temperature dependence," *J. Atmos. Chem.*, vol. 21, no. 3, pp. 263–273, 1995.

[135] M. C. Drake and J. W. Ratcliffe, "High temperature quenching cross sections for nitric oxide laser-induced fluorescence measurements," *J. Chem. Phys.*, vol. 98, no. 5, p. 3850, 1993.

[136] R. S. Yates and M. K. Stenstrom, "Gravimetric sampling procedure for aqueous ozone concentrations," *Water Res.*, vol. 34, no. 4, pp. 1413–1416, 2000.

[137] R. Chand, D. H. Bremner, K. C. Namkung, P. J. Collier, and P. R. Gogate, "Water disinfection using the novel approach of ozone and a liquid whistle reactor," *Biochem. Eng. J.*, vol. 35, no. 3, pp. 357–364, 2007.

[138] H. Bader and J. Hoigné, "Determination of ozone in water by the indigo method," *Water Res.*, vol. 15, no. 4, pp. 449–456, 1981.

[139] M. E. Williams and J. L. Darby, "Measuring ozone by indigo method: interference of suspended material," vol. 118, no. 6, pp. 988–993, 1992.

[140] M. I. Hasan, Y. Morabit, A. Dickenson, and J. L. Walsh, "Impact of electrode geometry on an atmospheric pressure surface barrier discharge," vol. 264101, no. June, pp. 1–5, 2017.

[141] A. Dickenson, N. Britun, A. Nikiforov, C. Leys, M. I. Hasana, and J. L. Walsh, "The generation and transport of reactive nitrogen species from a low temperature atmospheric pressure air plasma source," *PCCP*, pp. 28499–28510, 2018.

[142] A. Dickenson, Y. Morabit, M. I. Hasan, and J. L. Walsh, “Directional mass transport in an atmospheric pressure surface barrier discharge,” *Sci. Rep.*, vol. 7, no. 1, pp. 1–9, 2017.

[143] W. H. Tay, S. S. Kausik, C. S. Wong, S. L. Yap, and S. V. Muniandy, “Statistical modelling of discharge behavior of atmospheric pressure dielectric barrier discharge,” *Phys. Plasmas*, vol. 21, no. 11, 2014.

[144] M. G. Kong *et al.*, “Plasma medicine: An introductory review,” *New J. Phys.*, vol. 11, 2009.

[145] T. Shimizu, Y. Sakiyama, D. B. Graves, J. L. Zimmermann, and G. E. Morfill, “The dynamics of ozone generation and mode transition in air surface micro-discharge plasma at atmospheric pressure,” *New J. Phys.*, vol. 14, no. 10, p. 103028, 2012.

[146] J. H. Park *et al.*, “Effect of cleaning and sterilization on titanium implant surface properties and cellular response,” *Acta Biomater.*, vol. 8, no. 5, pp. 1966–1975, 2012.

[147] S. Cha and Y. S. Park, “Plasma in dentistry,” *Clin. Plasma Med.*, vol. 2, no. 1, pp. 4–10, 2014.

[148] F. Vatansever *et al.*, “Antimicrobial strategies centered around reactive oxygen species - bactericidal antibiotics, photodynamic therapy, and beyond,” *FEMS Microbiol. Rev.*, vol. 37, no. 6, pp. 955–989, 2013.

[149] J. D. Luo and A. F. Chen, “Nitric oxide: A newly discovered function on wound healing,” *Acta Pharmacol. Sin.*, vol. 26, no. 3, pp. 259–264, 2005.

[150] M. Sher, A, M. Braude, B, E. Cleaton-Jones, P, G. Moyes, D, and J. Mallett, “Nitrous oxide sedation in dentistry,” *Anaesthesia*, vol. 39, no. 8, pp. 837–838, 1984.

[151] P. Leelataweewud, W. F. Vann, D. C. Dilley, and W. J. Lucas, “The physiological effects of supplemental oxygen versus nitrous oxide/oxygen during conscious sedation of pediatric dental patients.,” *Pediatr. Dent.*, vol. 22, no. 2, pp. 125–33,

2000.

[152] J. V. Michael, “Thermal decomposition of ozone,” *J. Chem. Phys.*, vol. 54, no. 10, pp. 4455–4459, 1971.

[153] M. B. McElroy, S. C. Wofsy, and Y. L. Yung, “The nitrogen cycle: perturbations due to man and their impact on atmospheric N2O and O3,” *Philos. Trans. R. Soc. London*, 1977.

[154] W. C. Wang and N. D. Sze, “Coupled effects of atmospheric N2O and O3 on the earth’s climate,” *Nature*, vol. 286, no. 5773, pp. 589–590, 1980.

[155] U. Kogelschatz and P. Baessler, “Determination Of Nitrous Oxide And Dinitrogen Pentoxide Concentrations In The Output Of Air-Fed Ozone Generators Of High Power Density,” *Ozone Sci. Eng.*, vol. 9, no. 3, pp. 195–206, 1987.

[156] M. . Nicolet and E. . Vergison, “L ’ oxyde azoteux dans la stratosphère,” *Aeron. A ACT A*, 1971.

[157] P. J. Crutzen, “Ozone production rates in an oxygen-hydrogen-nitrogen oxide atmosphere,” *J. Geophys. Res.*, vol. 76, no. 30, pp. 7311–7327, 1971.

[158] J. Liebmann *et al.*, “Biological effects of nitric oxide generated by an atmospheric pressure gas-plasma on human skin cells,” *Nitric Oxide - Biol. Chem.*, vol. 24, no. 1, pp. 8–16, 2011.

[159] B. Haertel, T. von Woedtke, K. D. Weltmann, and U. Lindequist, “Non-thermal atmospheric-pressure plasma possible application in wound healing,” *Biomol. Ther.*, vol. 22, no. 6, pp. 477–490, 2014.

[160] R. Bansemer, A. Schmidt-Bleker, U. Van Rienen, and K.-D. Weltmann, “Investigation and control of the O3- to NO- transition in a novel sub-atmospheric pressure dielectric barrier discharge,” *Plasma Sources Sci. Technol.*, vol. 26, no. 6, 2017.

[161] K. Takeda, K. Ishikawa, H. Tanaka, M. Sekine, and M. Hori, “Spatial distributions of O , N , NO , OH and vacuum ultraviolet light along gas flow direction in an AC-excited

atmospheric pressure Ar plasma jet generated in open air," *J. Phys. D Appl. Phys*, vol. 50, no. 19, p. 195202, 2017.

[162] A. F. H. Van Gessel, B. Hrycak, M. Jasiński, J. Mizeraczyk, J. J. A. M. Van Der Mullen, and P. J. Bruggeman, "Temperature fitting of partially resolved rotational spectra," *J. Instrum.*, vol. 7, no. 2, p. C02054, 2012.

[163] S. Yonemori and R. Ono, "Effect of discharge polarity on the propagation of atmospheric-pressure helium plasma jets and the densities of OH, NO, and O radicals," *Biointerphases*, vol. 10, no. 2, p. 029514, 2015.

[164] M. I. Hasan, Y. Morabit, A. Dickenson, and J. L. Walsh, "Impact of electrode geometry on an atmospheric pressure surface barrier discharge," *Appl. Phys. Lett.*, vol. 110, no. 26, pp. 1–5, 2017.

[165] N. Mastanaiah, P. Banerjee, J. A. Johnson, and S. Roy, "Examining the role of ozone in surface plasma sterilization using dielectric barrier discharge (DBD) plasma," *Plasma Process. Polym.*, vol. 10, no. 12, pp. 1120–1133, 2013.

[166] C. L. Enloe, G. I. Font, T. E. McLaughlin, and D. M. Orlov, "Surface Potential and Longitudinal Electric Field Measurements in the Aerodynamic Plasma Actuator," *AIAA J.*, vol. 46, no. 11, pp. 2730–2740, 2008.

[167] M. A. De Moraes, R. F. Weska, and M. M. Beppu, "Effects of sterilization methods on the physical, chemical, and biological properties of silk fibroin membranes," *J. Biomed. Mater. Res. - Part B Appl. Biomater.*, vol. 102, no. 4, pp. 869–876, 2014.

[168] Y. Tian, R. Ma, Q. Zhang, H. Feng, and Y. Liang, "Assessment of the Physicochemical Properties and Biological Effects of Water Activated by Non-Thermal Plasma Above and Beneath the Water Surface," pp. 16–17, 2015.

[169] G. Kamgang-youbi, J. Herry, and J. Brisset, "Impact on disinfection efficiency of cell load and of planktonic / adherent / detached state : case of Hafnia alvei inactivation by Plasma Activated Water," pp. 449–457, 2008.

[170] J. L. Brisset and E. Hnatiuc, “Peroxynitrite: A re-examination of the chemical properties of non-thermal discharges burning in air over aqueous solutions,” *Plasma Chem. Plasma Process.*, vol. 32, no. 4, pp. 655–674, 2012.

[171] C. Ducrocq, B. Blanchard, B. Pignatelli, and H. Ohshima, “Peroxynitrite: an endogenous oxidizing and nitrating agent.,” *Cell. Mol. Life Sci.*, vol. 55, no. 8–9, pp. 1068–1077, 1999.

[172] W. Heaselgrave, P. W. Andrew, and S. Kilvington, “Acidified nitrite enhances hydrogen peroxide disinfection of Acanthamoeba, bacteria and fungi,” *J. Antimicrob. Chemother.*, vol. 65, no. 6, pp. 1207–1214, 2010.

[173] G. A. O’May, N. Reynolds, and G. T. Macfarlane, “Effect of pH on an in vitro model of gastric microbiota in enteral nutrition patients,” *Appl. Environ. Microbiol.*, vol. 71, no. 8, pp. 4777–4783, 2005.

[174] M. J. Lee, J. S. Kwon, H. B. Jiang, E. H. Choi, G. Park, and K. M. Kim, “The antibacterial effect of non-thermal atmospheric pressure plasma treatment of titanium surfaces according to the bacterial wall structure,” *Sci. Rep.*, vol. 9, no. 1, pp. 1–13, 2019.

[175] O. Lunov *et al.*, “Towards the understanding of non-thermal air plasma action: Effects on bacteria and fibroblasts,” *RSC Adv.*, vol. 6, no. 30, pp. 25286–25292, 2016.